Winter 2010

Numerical simulations of combined wave-current bottom boundary layers

Gary R. Margelowsky
University of New Hampshire, Durham

NUMERICAL SIMULATIONS OF COMBINED WAVE-CURRENT BOTTOM BOUNDARY LAYERS

BY

GARY R. MARGELOWSKY

Bachelor of Science, The Ohio State University, 2008

THESIS

Submitted to the University of New Hampshire
in Partial Fulfillment of
the Requirements for the degree of

Master of Science

in

Ocean Engineering

December 2010

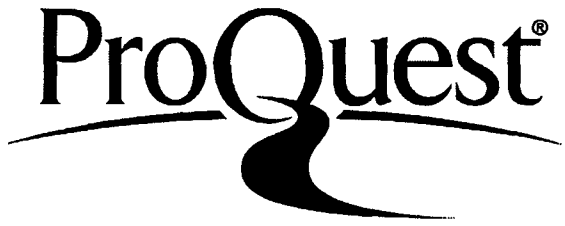

ProQuest LLC
789 East Eisenhower Parkway
P.O. Box 1346
Ann Arbor, MI 48106-1346

This thesis has been examined and approved.

Thesis Director, Diane L. Foster
Associate Professor of Mechanical Engineering and Ocean Engineering

James D. Irish
Research Professor of Ocean Engineering

Thomas C. Lippmann
Research Associate Professor of Earth Sciences and Ocean Engineering

Kenneth C. Baldwin
Professor of Mechanical Engineering and Ocean Engineering and Marine Sciences

11 December 2010
Date

ACKNOWLEDGMENTS

This work would not have been possible without the love and support of my family. Although this chapter of my life involved a geographic separation, you remained as close as ever, helping me along I am sure more than you know.

I would like to thank Dr. Diane Foster for her advice, guidance, and occasional home cooked meals. Without her persistence during my undergraduate years, I would undoubtedly not be where I am today. I am grateful for the many opportunities you have presented me.

Thank you to Dr. Peter Traykovski of Woods Hole Oceanographic Institute for sharing, and assistance in interpreting, the field observations you collected. Your timely responses to my never ending questions were always appreciated.

I thank the SMART Fellowship program, for selecting and supporting me during my two years at UNH.

Finally, I thank all of the close friends I have accumulated up to this point in life's journey. There is far too much to say to mention you all individually. I would like to acknowledge fellow students of the OE grad student area - including, but not limited to: James Wright, Ryan Despins, Tim Picket, Jud Decew, Alex Johnston, Meagan Wengrove, Donya Frank, and Sylvia Rodriguez Abudo - for your help, support, and comic relief. I especially thank my Puerto Rican sister for her advice, inside jokes, countless laughs, and brutal honesty. Without the many facets of your assistance, I could not have made it through this endeavor.

TABLE OF CONTENTS

List of Tables

List of Figures

ABSTRACT

NUMERICAL SIMULATIONS OF COMBINED WAVE-CURRENT BOTTOM BOUNDARY LAYERS

by

Gary R. Margelowsky
University of New Hampshire, December, 2010

The hydrodynamics of wave-current bottom boundary layers are examined with a quasi-three-dimensional non-hydrostatic bottom boundary layer model, **Dune**. Flow is simulated by resolving the Reynolds-Averaged Navier-Stokes equations with a k-ω 2^{nd} order turbulence closure. The model simulations are performed for a range of theoretical and observed hydrodynamic forcing conditions to examine the boundary layer sensitivity to the wave and current forcing and bedform resolution.The model is evaluated with field observations of velocity profiles and seabed geometry collected at the Martha's Vineyard Coastal Observatory (MVCO, Edgartown, MA) in 2005 in 13 m water depth.

Model simulations forced by observed velocity time series best predicted field observations. Bichromatic wave groups simulations showed favorable results with observations, suggesting the importance of modulating velocity magnitudes. The flow field was found to be highly spatially variable in the vicinity of the bedform, emphasizing the importance of instrument location relative to bedform geometry.

CHAPTER 1

INTRODUCTION

1.1 Background

According to the National Oceanic and Atmospheric Administration (NOAA), approximately half of the United States population lives within 50 miles of a coastline (*Dalrymple*, 2001). Coastal regions are often of high economic importance due to their large population concentration, tourism, and coastal infrastructure supporting the transport of goods and services. A comprehensive understanding of circulation and sediment transport on the inner continental shelf will lead to improved management of coastal communities. Furthermore, improved knowledge of these processes will lead to more informative decisions regarding beach nourishment and waterway navigation.

Viscous flow over a boundary results in a region of deformation in the velocity field known as the boundary layer. The bottom boundary layer is a dynamic region of fluid flow near the seabed characterized by high shear stresses, and significant energy dissipation. This region was first characterized by Prandtl in the early twentieth century, and remains a topic of scientific interest today (*Kundu and Cohen*, 2008). The shape of the bottom boundary layer is a function of the free stream flow characteristics, as well as the bottom boundary characteristics (e.g. sediment

grain size and bedform geometry). Bottom boundary layer dynamics have a significant impact on sediment transport, wave height attenuation, pollution dispersal, biologic tracking, and coastal circulation patterns (*Sleath*, 1991).

Steady flows, such as currents over fixed flat beds, have been studied extensively, and are relatively well understood (*Kundu and Cohen*, 2008). However, natural flow environments are often complicated by beds of sediment arranged in a variety of geometries. The small scale morphology at the bed, known as bedforms, complicate the characteristics of the flow field by enhancing turbulence, and introducing vortex formation and ejection near the bottom boundary. Numerous studies of steady flow over bedforms have expanded the knowledge of flow characteristics in this environment (*Arya*, 1975; *Chriss and Caldwell*, 1982; *Ranasoma and Sleath*, 1994; *Kundu and Cohen*, 2008). In steady current regimes, the bottom boundary layer is often able to fully develop into a state of equilibrium, reaching the free surface and thus decreasing the flow complexity.

Coastal flows are further complicated by an unsteady component - waves. Due to the relatively short periods associated with the oscillatory forcing of free surface gravity waves, the time-dependent near-bed boundary layer is never able to fully develop, remaining in a state of transition throughout all phases of the wave period. The short temporal scale of waves results in much larger shear stresses at the bottom boundary than for currents of the same magnitude (*Grant and Madsen*, 1979). Moreover, non-linear wave-current interactions introduce greater complexity to the combined wave-current flow field (*Grant and Madsen*, 1979; *Nielsen*, 1992; *Fredsøe et al.*, 1999). Possible effects of wave-current interactions include enhanced shear

and turbulence above the bottom boundary, as well as increased transport due to wave stresses that mobilize the bed, and longer period currents that displace the entrained sediment.

One way to better understand and predict coastal flow and transport dynamics in the nearshore and on the inner shelf is through the development of accurate numerical models to simulate flow. Computational Fluid Dynamics (CFD) uses fine-scale numerical approximations of the relevant conservation laws (conservation of mass, momentum, and energy) to produce quantitative predictions of various fluid-flow phenomena (*Kundu and Cohen*, 2008). As large scale coastal circulation models generally rely on sub-grid parameterization very small scale processes, embedded models with finer resolution are often employed to predict the flow structure and quantify the boundary induced roughness. The ability to accurately model the bottom boundary layer, including velocity distribution and bottom shear stress under combined waves and currents, is essential to the study of sediment transport, as well as fluid dynamics and circulation on the inner continental shelf (*Grant and Madsen*, 1979).

1.2 Motivation

Of particular interest is the underlying question of the hydrodynamic forcing resolution necessary to accurately simulate bottom boundary layer flow. Given the scale of coastal bottom boundary layers, existing numerical models require simplifications and approximations to account for boundary roughness, forcing parameters, and turbulence. These simplifications lead to a significant decrease in computa-

tional expense, but can significantly impact the dynamics of interest. Nearshore flow fields are often comprised of combined currents and random waves that interact with a bed of unconsolidated sediment arranged in a range of geometries. The significant spatial and temporal hydrodynamic variability of these individual contributions creates an impressively high number of possible outcomes across the inner continental shelf. Thus, to avoid the large numerical demands required to simulate exact field conditions, hydrodynamic forcing is often simulated using a characteristic bottom roughness (e.g. *Grant and Madsen* (1979)). The goal of this investigation is to determine the sensitivity of bottom boundary layer dynamics to forcing and boundary conditions

This effort was motivated by bathymetric observations in Portsmouth Harbor, Portsmouth, NH obtained by *Felzenberg* (2009), using multi-beam echosounders from June 2007 to July 2008. Surveys were conducted during slack water following subsequent flood and ebb tidal phases during a neap tide on 8 June 2007, as well as during the following spring tide on 14 June 2007. Similar multi-beam surveys were completed over neap and spring tides in 3 July 2008 and 9 July 2008, respectively. An example of one *Felzenberg* (2009) survey is shown in Figure 1-1. An Acoustic Doppler Current Profiler (ADCP) was deployed on the eastern margin of the bedform field during the 2008 surveys. The ADCP measured three components of velocity from 1.03 to 8.83 meters above bottom in 0.20 m vertical bins with six minute averages of velocity measurements. Multiple scales of bedforms existed in this area, ranging from dunes with heights O(1 m) and wavelengths O(10 m) to small scale ripples with heights of centimeters and wavelengths of 10's of centime-

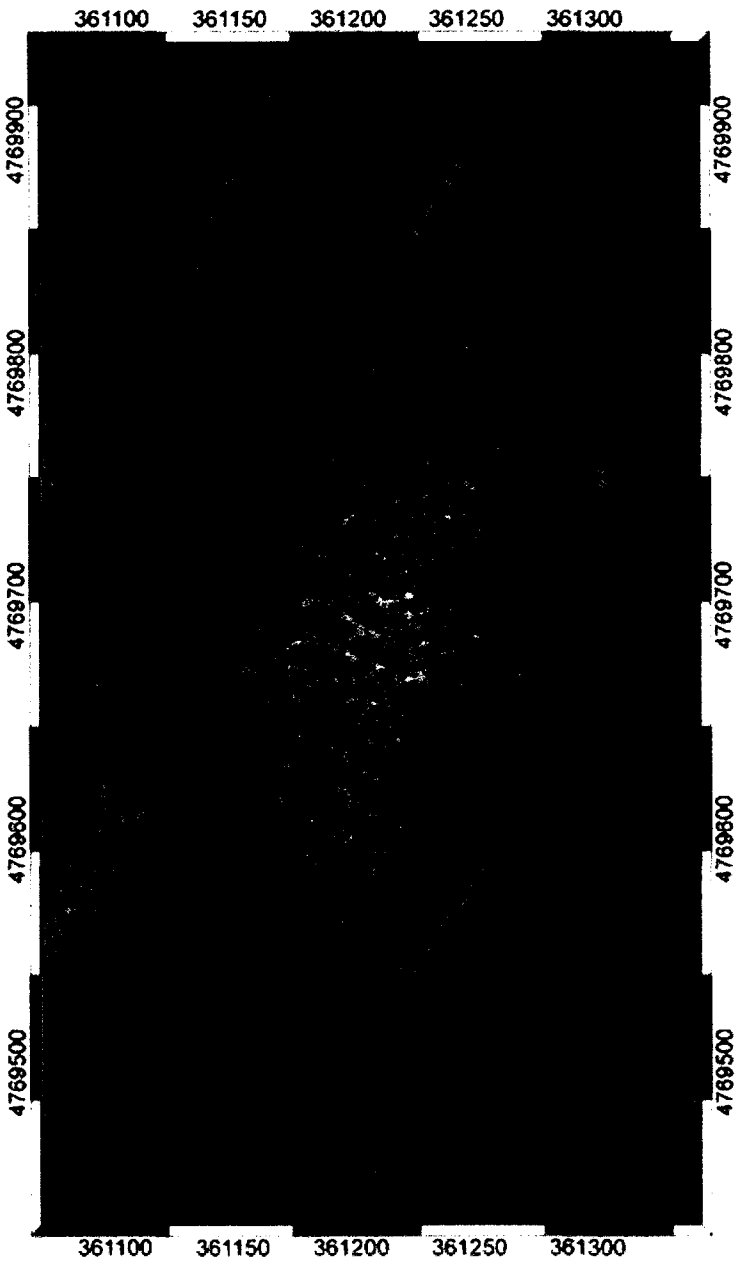

Figure 1-1: High-resolution multibeam echosounder bathymetry data obtained in Portsmouth Harbor, Portsmouth, NH as published by *Felzenberg* (2009). Length scales are in meters. Lettered lines show locations of profiles used in the study.

ters, which were often found superimposed on the larger dunes. Felzenberg used an innovative BISHNU fingerprint algorithm to track bedform field migrations. Bedform migrations were compared to the hydrodynamic forcing conditions obtained

by the ADCP.

Vertical profiles of flow velocity over bedforms is dependent on horizontal position along the bedform, as shown in Figure 1-2 (*Fredsøe et al.*, 1999). High resolution images of larger dune profiles were obtained by multibeam echosounders (see Figure 1-1). Temporal variation in dune morphology was observed by overlaying bathymetric profiles at a single location over over numerous surveys. Diver photographs of a grid of known dimensions on the sea floor provided quantitative information on smaller-scale ripple geometry characteristics. Thus, detailed quantification of bedforms were obtained in the *Felzenberg* (2009) investigation. High resolution observations of the flow field were not obtained, as the location of velocity profile along the bedform was not recorded, and sampling interval for velocity measurements was too slow to accurately resolve the wave field. Although these data do not have the resolution to address the questions of interest, they motivate interest in data resolution required to numerically resolve the flow field using CFD modeling.

Traykovski (2007) obtained fine-scale bathymetry and velocity measurements off the coast of Martha's Vineyard Coastal Observatory (MVCO, Edgartown MA) in September 2005 – April 2006. Hourly high-resolution bathymetric maps, near bed velocity profiles, and velocity point measurements were acquired. The *Traykovski* (2007) data set provides adequate resolution of seabed characteristics and hydrodynamic conditions to evaluate the numerical bottom boundary layer model chosen for the present effort. This investigation will explore the impact of a variety of forcing conditions including currents-only, waves-only, and combined wave-currents

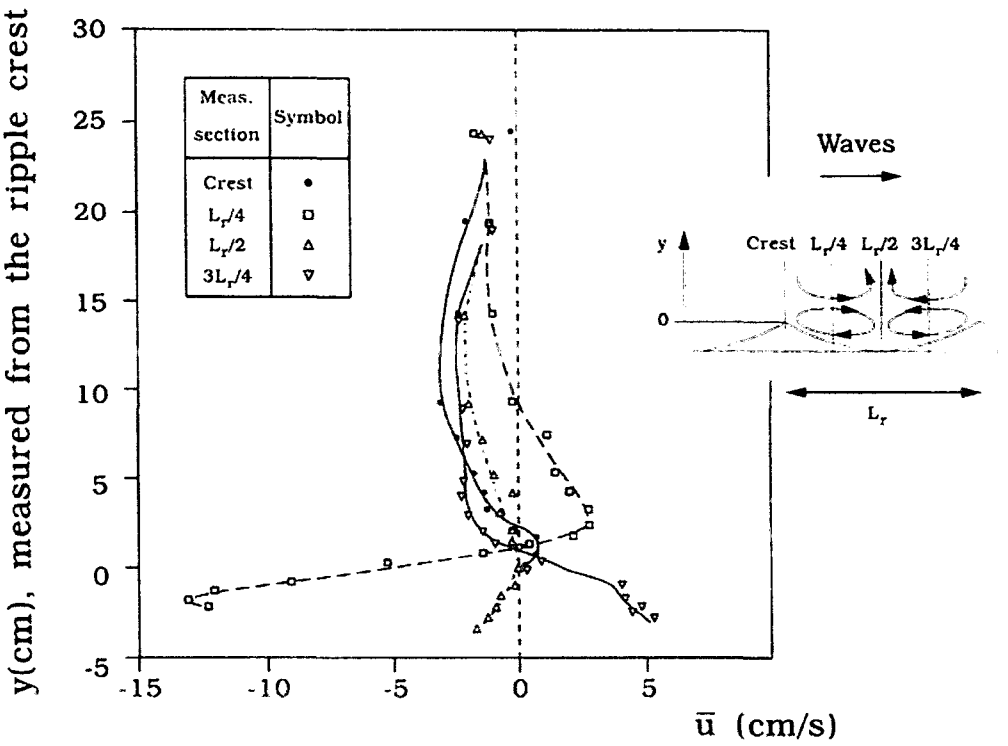

Figure 1-2: Close-up picture of the period-averaged velocity profiles at four measurement sections, as published by *Fredsøe et al.* (1999)

at varying angles, over a rough rippled bed to examine the sensitivity of near-bed flow field dynamics to various resolutions of hydrodynamic forcing.

1.3 Model Background

The CFD model chosen for this investigation, **Dune**, was originally created at the Technical University of Denmark in the early 1990s by Ph.D. student, Søren Tjerry, and his advisor, Prof. Jørgen Fredsøe (*Tjerry*, 1995). The objective of the model effort was to simulate the interaction of flow and sediment structures in riverine environments to resolve sediment transport, bed stress, pressure, and velocity

characteristics throughout the water column (*Tjerry*, 1995; *Tjerry and Fredsøe*, 2005). This outcome was achieved by forcing constant pressure gradient flow over a prescribed bedform. Tjerry's model showed good agreement with laboratory collected data.

Turbulence modeling is used to approximate Reynolds stresses with known variables such that the governing Reynolds Averaged Navier-Stokes (herein, RANS) equations can be solved (see Appendix A for review of RANS equations). Although numerous turbulence models to quantify these stresses exist, this initial effort relied on a k-ϵ two-equation turbulence closure model (*Wilcox*, 1988), where k is turbulent kinetic energy, and ϵ is turbulent dissipation. This particular model is well tested, widely used, and commonly accepted among the turbulence modeling community (*Tjerry*, 1995). However, the k-ϵ model has been known to poorly estimate the dissipation equation and has been described as numerically stiff (*Tjerry and Fredsøe*, 2005).

The k-ϵ model characterizes the eddy viscosity with an additional equation for turbulent kinetic energy and viscous dissipation. Reynolds stresses are determined in a manner analogous to the molecular stresses, and defined by:

$$-\overline{u_i u_j} = \nu_t \left(\frac{\partial u_i}{\partial x_j} + \frac{\partial u_j}{\partial x_i} \right) - \frac{2}{3} k \tag{1.1}$$

where ν_t is the eddy viscosity, and the over-bar indicates averaging over a wave period. One short-coming of the eddy viscosity concept is that the equation is isotropic, whereas turbulence is anisotropic. Using the eddy viscosity concept, dimensional analysis, and time averaging (*Wilcox*, 1988; *Tjerry*, 1995), the turbulent

kinetic energy is specified by:

$$\frac{\partial k}{\partial t} + \frac{\partial u_j \epsilon}{\partial x_j} = \frac{\partial}{\partial x_j}\left(\frac{\nu_t}{\sigma_k}\frac{\partial k}{\partial x_j}\right) + \nu_t\left(\frac{\partial u_i}{\partial x_j} + \frac{\partial u_j}{\partial x_i}\right)\frac{\partial u_i}{\partial x_j} - \epsilon \tag{1.2}$$

Dissipation is found from:

$$\frac{\partial \epsilon}{\partial t} + \frac{\partial u_j \epsilon}{\partial x_j} = \frac{\partial}{\partial x_j}\left(\frac{\nu_t}{\sigma_\epsilon}\frac{\partial \epsilon}{\partial x_j}\right) + C_{\epsilon 1} c_\mu k\left(\frac{\partial u_i}{\partial x_j} + \frac{\partial u_j}{\partial x_i}\right)\frac{\partial u_i}{\partial x_j} - C_{\epsilon 2}\frac{\epsilon^2}{k} \tag{1.3}$$

where c_μ is the return to isotropy constant, σ_ϵ is dissipation transfer, σ_k is the Schmidt number, and $C_{\epsilon 1}$ and $C_{\epsilon 2}$ are dissipation equation constants 1 and 2, respectively. The coefficients utilized in the k-ϵ dissipation equation (1.3) are presented in Table 1.3. These constants are consistent with typical values given in *Wilcox* (1998). The equations were solved using boundary conditions that applied given the geometries present, including logarithmic velocity profile at wall boundaries, as well as typical inlet and outlet boundary conditions.

c_μ	σ_ϵ	σ_k	$C_{\epsilon 1}$	$C_{\epsilon 2}$
0.09	1.3	1.0	1.44	1.92

Table 1.1: k-ϵ closure coefficients

Dune resolves the mean and wave components of the fully turbulent flow field. In the case of flow over bedforms, the non-hydrostatic simulations are capable of reproducing flow separation in the vicinity of the ripple crest. The model resolves hydraulically rough flow over both flat and rippled beds. The periodic boundary conditions at the sidewalls assumes a repeated geometry. The model approximates

the velocity and pressure profiles through the water column, as well as bed shear stresses and the resulting sediment transport.

The model was evaluated with measured flow over dunes obtained experimentally by *Nelson et al.* (1993). The flow was measured over a 4 cm high, 80 cm long sinusoidal concrete dune in a water depth of 21.5 cm with a free stream velocity of 36 cm/s and roughness of 0.43 mm. In the experiment, seven profiles over the dune were measured. These measurements were compared to the outcome of the model. Flow velocity was predicted well, with an error of 10%, often due to low estimates of velocity near the bed (*Tjerry*, 1995).

Model estimates of sediment transport were also evaluated with the observations. Sediment motion is typically evaluated with estimates of the Shields parameter, though with significant uncertainty of around 50% existing in the prediction of dune geometries when Shields parameters are large. However, for relatively small Shields parameters, bedform geometry (height and wavelength) predictions agree quite well with experimental data (*Tjerry and Fredsøe*, 2005).

Following *Tjerry* (1995), *Andersen* (1999) modified the model to resolve an oscillatory component, representative of waves, to approximate boundary layer hydrodynamics within coastal environments. Perhaps the most significant of *Andersen* (1999)'s modifications was the use of a k-ω 2^{nd} order turbulence closure scheme, rather than the k-ϵ model originally chosen. Originally developed by *Kolmogorov* (1942), the k-ω model utilized in this effort is the modified version of *Wilcox* (1988), where ω is specific dissipation. The transport equations for k and ω are as follows:

$$\frac{\partial k}{\partial t} + U_j \frac{\partial k}{\partial x_j} = \frac{\partial}{\partial x_j}\left[(\nu + \sigma^* \nu_t)\frac{\partial k}{\partial x_j}\right] - \overline{u_i u_j}\frac{\partial U_i}{\partial x_j} - \beta^* k\omega \tag{1.4}$$

$$\frac{\partial \omega}{\partial t} + U_j \frac{\partial \omega}{\partial x_j} = \frac{\partial}{\partial x_j}\left[(\nu + \sigma \nu_t)\frac{\partial \omega}{\partial x_j}\right] - \nu\frac{\omega}{k}\overline{u_i u_j}\frac{\partial U_i}{\partial x_j} - \beta\omega^2 \tag{1.5}$$

where, k is turbulent kinetic energy, U_j is the mean and wave velocity components, u_i' is the fluctuating turbulent velocity, ν is kinematic viscosity, ω is specific dissipation rate, and ν_t is the eddy viscosity. Closure coefficients, in accordance with *Wilcox* (1998), are given in Table 1.2. The k-ω model was chosen because it yields better estimates in flows with strong adverse pressure gradients (*Fredsøe et al.*, 1999; *Wilcox*, 1988), resulting in more accurate results for oscillatory flows. The vertical grid cell thickness closest to the bed is set to ensure that at least two grid cells are located within the viscous sublayer, so that viscous stresses can be resolved at the bed (*Andersen*, 1999).

γ^*	γ	β^*	β	σ^*	σ
1	5/9	9/100	3/40	1/2	1/2

Table 1.2: k-ω closure coefficients.

Both *Natoo* (2003) and *Marieu et al.* (2008) have used Dune to determine hydrodynamics and morphodynamics within wave-current bottom boundary layers over flat and rippled sand beds (*Frank*, 2008). *Natoo* (Accepted) provided the first direct pairing of a 2-D numerical model with field observations of velocity and suspended sediment within the nearshore environment. Suspended sediment over flat and rippled beds was consistent with bistatic Coherent Velocity and Sediment Pro-

filer (BCDVSP) data collected during the 1997 SANDYDUCK experiment at the Army Corps of Engineer's Field Research Facility (FRF), in Duck, N.C. (*Natoo*, Accepted).

Most recently, *Frank* (2008) used **Dune** to compare hydrodynamic estimates predicted by various other analytical and empirical models. This included comparisons of velocity profiles and bed stresses over flat and rippled beds. Significant improvements to the model by *Frank* (2008) include enhancements for more robust numerical stability, as well as the ability for the model to simulate wave and current flow approaching from different incident angles. This quasi-three-dimensional (quasi-3D) version of **Dune** is used for the present investigation. The model can resolve a wide range of current angles (from 0 to 360 degrees), wave periods, free-stream currents and wave orbital velocities over both flat and rippled erodible, non-sloping sediment beds.

The present quasi-3D version of **Dune** assumes the bedform morphology and velocity field is uniform in the alongshore (y) direction. **Dune** resolves the incompressible RANS and continuity equations in Cartesian coordinates, given in indicial notation by:

$$\frac{\partial \overline{u_i}}{\partial t} + \frac{\partial \overline{u_i u_j}}{\partial x_j} = -\frac{1}{\rho}\frac{\partial \overline{p}}{\partial x_j} + \nu \frac{\partial^2 u_i}{\partial x_j^2} - \frac{\partial \overline{u_i' u_j'}}{\partial x_j^2} \tag{1.6}$$

$$\frac{\partial \overline{u_i}}{\partial x_i} = 0 \tag{1.7}$$

To solve the model's governing equations, a finite volume approach was implemented. A boundary-fitted hyperbolic grid is used as it improves estimates of

the stress in the near bed region and conforms to the bedform geometry (*Tjerry*, 1995). Using a finite volume iterative solution technique, velocity and pressure are resolved in each grid cell.

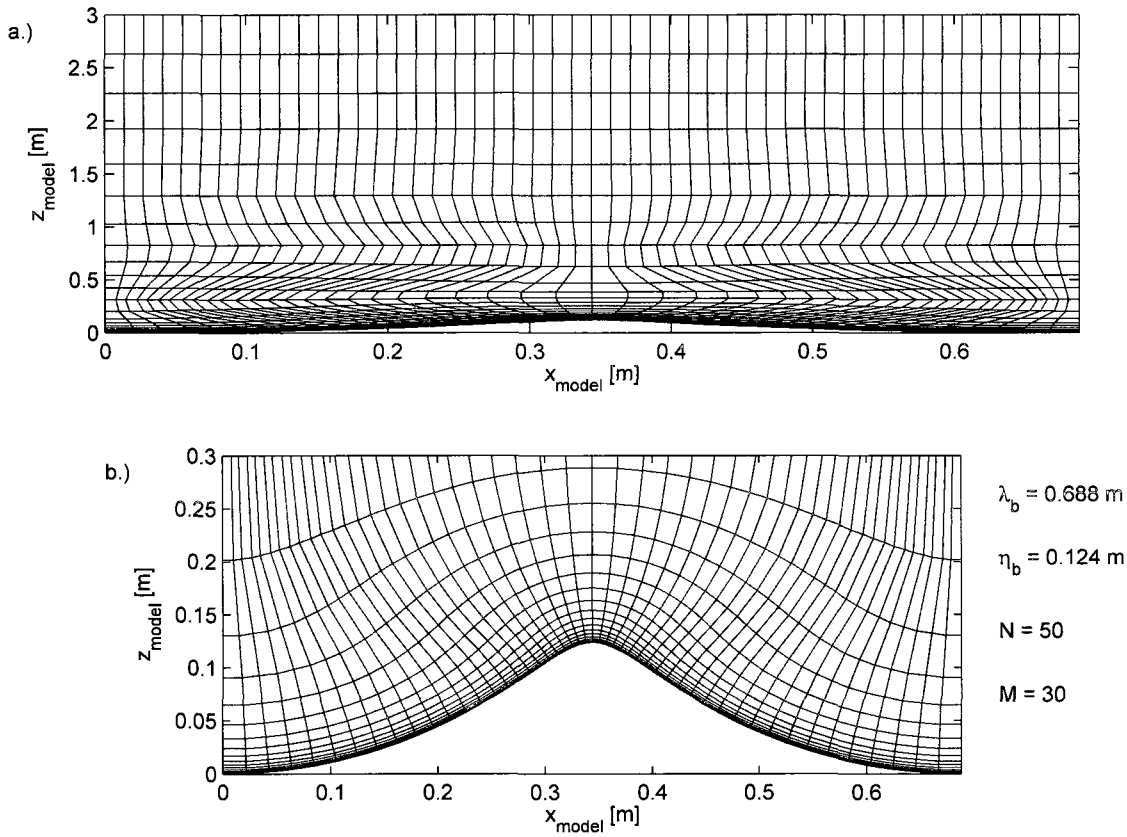

Figure 1-3: **Dune** Grid Example with a 3 m domain height, 50 horizontal (N) and 30 vertical (M) grid cells. a.) reveals the grid structure over the entire domain of the simulation, b.) shows an expanded view of the same grid with horizontal and vertical axis length scales of equal scaling. The bedform has wavelength (λ_b) and height (η_b) of 0.688 m and 0.124 m, respectively.

Vertical grid spacing is increased as distance from the bed increases. Higher resolution of vertical grid cells near the bed are necessary to resolve the hydrodynamics within the wave bottom boundary layer. A sample grid from simulations in the present investigation is shown in Figure 1-3. For this particular simulation, there were 50 grid cells in the horizontal (N), and 30 grid cells in the vertical (M).

For this example simulation, bedform wavelength (λ_b) is 0.688 m, with a bedform height (η_b) of 0.124 m.

This investigation considers combined wave and current flows over rough bedforms. Inter-model comparisons between various simulations with different forcing parameters as well as between field data and model simulations are presented.

CHAPTER 2

OBSERVATIONS

Field observations were obtained as part of the Mine Burial Experiments at Martha's Vineyard Coastal Observatory (MVCO, Edgartown, MA) in September 2005 - April 2006 (*Traykovski*, 2007). A quad-pod instrument frame straddled the area of observation in a water depth of 12.7 m. Two grab samples obtained within 10 m of the instrument frame revealed a median grain diameter (d_{50}) of 750 μm. Instrumentation was fixed to the frame via horizontal crossbars (Figure 2-1). Single point velocity measurements were obtained with a Nortek Acoustic Doppler Velocimeter (ADV) located 50 cm above the footpads of the instrument frame. Velocity profiles were obtained via a Sontek Dopbeam components assembled into a Bistatic Coherent Pulse Doppler Profiler by Woods Hole Oceanographic Institution (WHOI), with the head of the instrument located 75 cm above the bottom of the frame's footpads. This instrument measures three components of velocity with a vertical bin size of 0.8 cm bins for vertical velocities, and horizontal velocity bins ranging between 0.8 and 2 cm in height. Although the bed elevation was temporally and spatially variable, the sampling volume range of the instrument always penetrated the sediment bed. Mean current velocity and wave direction obtained by an RD Instruments Acoustic Doppler Current Profiler (ADCP) located 120 m East of the instrument frame (on the MVCO main underwater node) was

positioned 2.4 meters above the bed and showed reasonable comparison with values obtained by the ADV at the instrument frame.

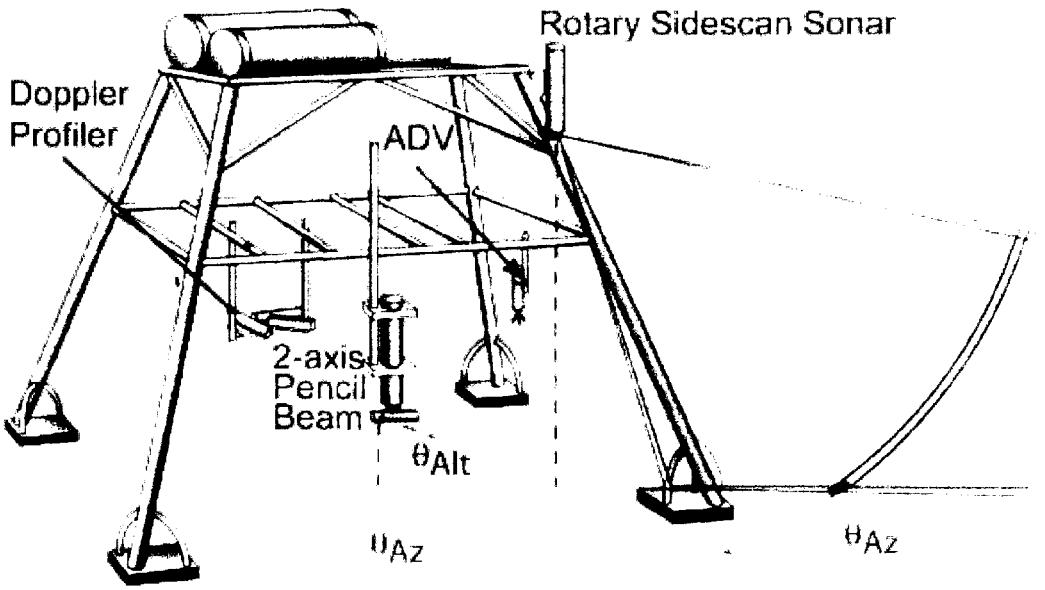

Figure 2-1: Instrumentation setup at MVCO site, 2005. As published by *Traykovski* (2007)

An Imagenex 881a two-axis rotary pencil-beam sonar provided hourly high resolution bathymetric surveys of the local area below the profiler and ADV instruments. The vertical position of the transducer and the rotary resolution of the stepper allowed for a resolution of the seabed geometry to 2 cm-horizontal by 1 cm-vertical in the vicinity of the instruments. The resolution decreased monotonically to 10 cm-horizontal and 5-cm vertical near the extent of the 3 meter radius from the instrument. In addition, an Imagenex 881 rotary side scan fan beam sonar located at the corner of the frame at 2.2 meters above the bottom provided characteristic ripple shape imagery within a 10 m radius of the transducer.

This investigation focuses on a subset of data collected from 14–15 September

2005. This subset was chosen for its relatively calm, consistent flow conditions with low variability in wave and current magnitudes. Furthermore, during this observational window, bedform geometry and ripple orientation remained relatively stationary with waves nearly perpendicular to ripple crests over the entire record. Twenty-six hourly bathymetric maps coupled with 10 minute records of ADV and Doppler profiler velocity measurements are examined. Each data set (one bathymetric survey coupled with 10 minute ADV and Doppler profiler velocity measurements) is referred to as a single burst. The present study focuses on bursts 280–305. Mean current velocities ranged from 0 to 15 cm/s and were predominantly tidal. Wave direction is calculated as the direction of maximum variance in the horizontal ADV velocity data time series for each 10 minute record. Standard deviation of wave velocity ranges from 13 to 17 cm/s over the 26 data sets analyzed. Peak wave period is determined by the peak in wave velocity spectra as measured by the ADV and varied from 9 to 12 s, with a predominant period of 10 s. Due to the spatial separation between ADV and the Doppler profiler instrument, the ADV time series is temporally shifted to be consistent with Doppler velocities by calculating the maximum correlation between the two instruments in the wave direction and shifting the ADV record by the resulting time step. The ADV data was sampled at 8 Hz. Doppler profiler data was processed at 4 Hz, and was subsequently interpolated to 8 Hz to match the sampling rate of the ADV (*Traykovski*, 2007).

As is common with acoustic profilers, vertical velocities are able to be measured with considerably greater accuracy than horizontal velocities due to the geometry of the transducer arrangement. This is partly due to the fact that vertical velocity

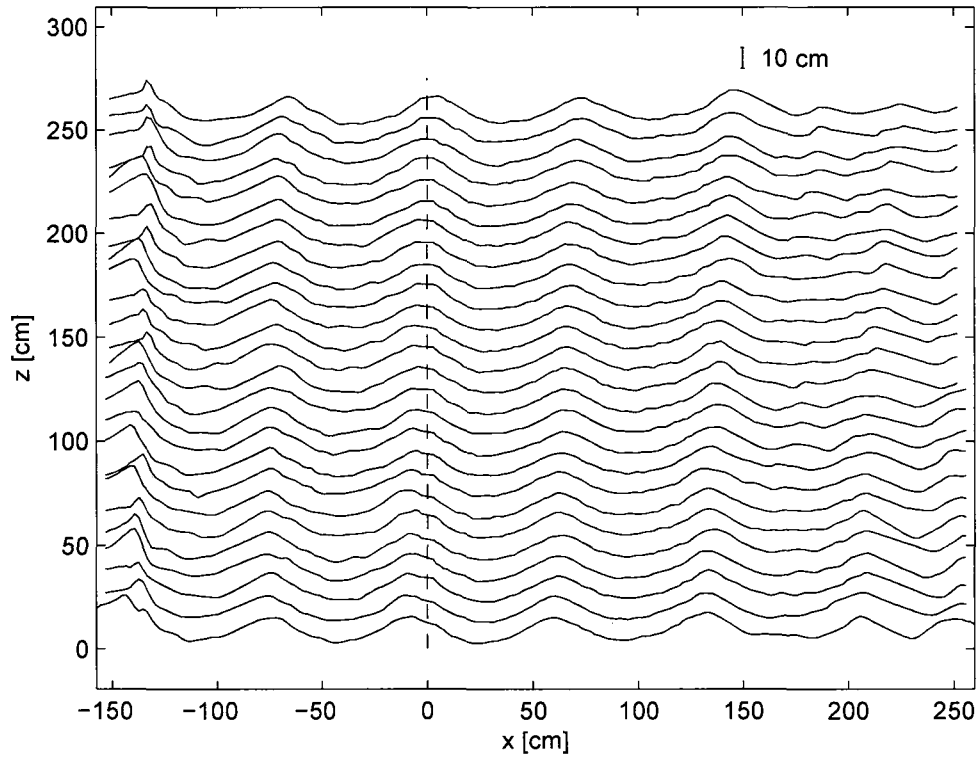

Figure 2-2: Bedform stack from profiles obtained by Imagenex 881a pencil beam sonar. Dashed line represents horizontal position of Doppler profiler instrument above seabed. Bedform for burst 280 depicted nearest zero in the vertical. Each subsequent hourly profile (bursts 281–305 are displaced by 10 centimeters in the positive vertical direction from the previous. A scale of 10 cm is provided in the upper right for convenience.

measurements require only one transducer, while horizontal velocity measurements require two to three transducers. Only vertical profile data is used for the ensuing analysis, as the instrument elevation with respect to the seabed did not provide adequate resolution to analyze horizontal components of velocity. Specifically, the overlap region of acoustic returns necessary to resolve horizontal components of velocity accurately was located predominantly below the surface of the sediment, yielding few reliable measurements of the horizontal flow field above the bottom boundary.

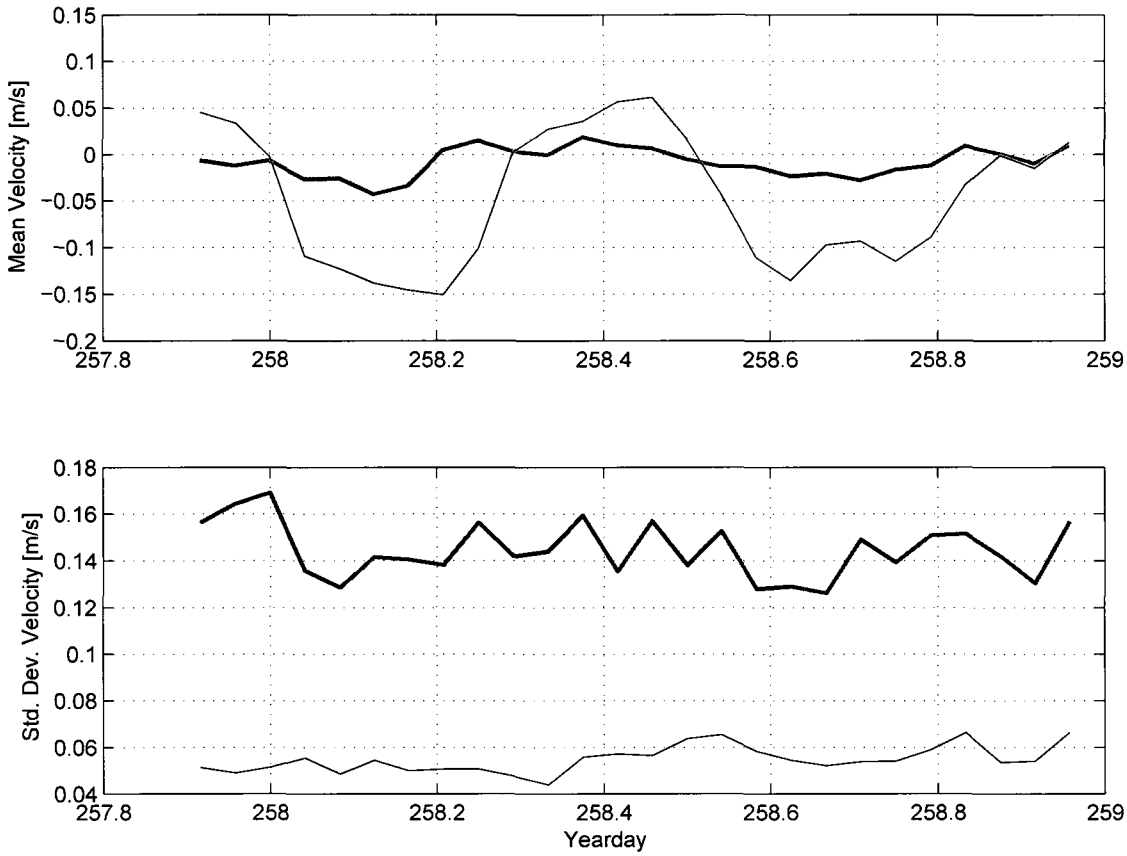

Figure 2-3: ADV record mean and standard deviation time series over the data subset of interest. Thick gray lines represent wave direction (Umax) velocity statistics. Thin black lines show statistics for horizontal velocities perpendicular to the wave direction (Umin).

One entire bathymetric survey, as measured by the two-axis rotating pencil beam sonar, required twenty-two minutes to cycle completely. As hourly data was desired, this duration was not conducive to recording multiple surveys and averaging for higher resolution. Ripple direction was determined by calculating the peak in the 2-dimensional Fourier Transform of the bathymetry. Consequently, ripple profiles for each data set were determined by taking a single slice of the bathymetry data from the pencil beam sonar in the ripple direction (perpendicular to the predominant ripple crest orientation) that passed through the point at which

the Doppler profiler sampling bins reached the bed.

More information regarding the deployment and observations for this Office of Naval Research (ONR) sponsored investigation can be found in *Traykovski* (2007).

CHAPTER 3

RESULTS

3.1 Model Setup

Simulations were performed for a range of bedforms, as well as wave and current conditions. The field observations showed that the bedform geometry remained relatively uniform with a slight migration (0.5 cm/hr in the +x direction) over the twenty-six hour record of interest as is shown in Figure 2-2. Simulations were performed over both the observed bedform and over a characteristic bedform. In each case, the model performance is evaluated at the horizontal position of the profiler in each of the 26 runs. Simulations performed with the observed bedform were determined by selecting the profile that was inline with the Doppler profiler. The profile was resampled to consist of a constant horizontal distance between points, such that the total number of points in the profile was 51, yielding approximately 1.5 cm resolution in the horizontal. Model spin up time was reduced by keeping the number of grid cells constant for all the runs. Resampled bed profiles were smoothed using a Gaussian window of three points. The object of the smoothing was to remove small perturbations likely associated with observational noise and spurious points resulting from the resampling algorithm, while leaving the main characteristics of the observed bedform intact. An example of a profile determined

bedform with the resulting grid is shown in Figure 3-1.

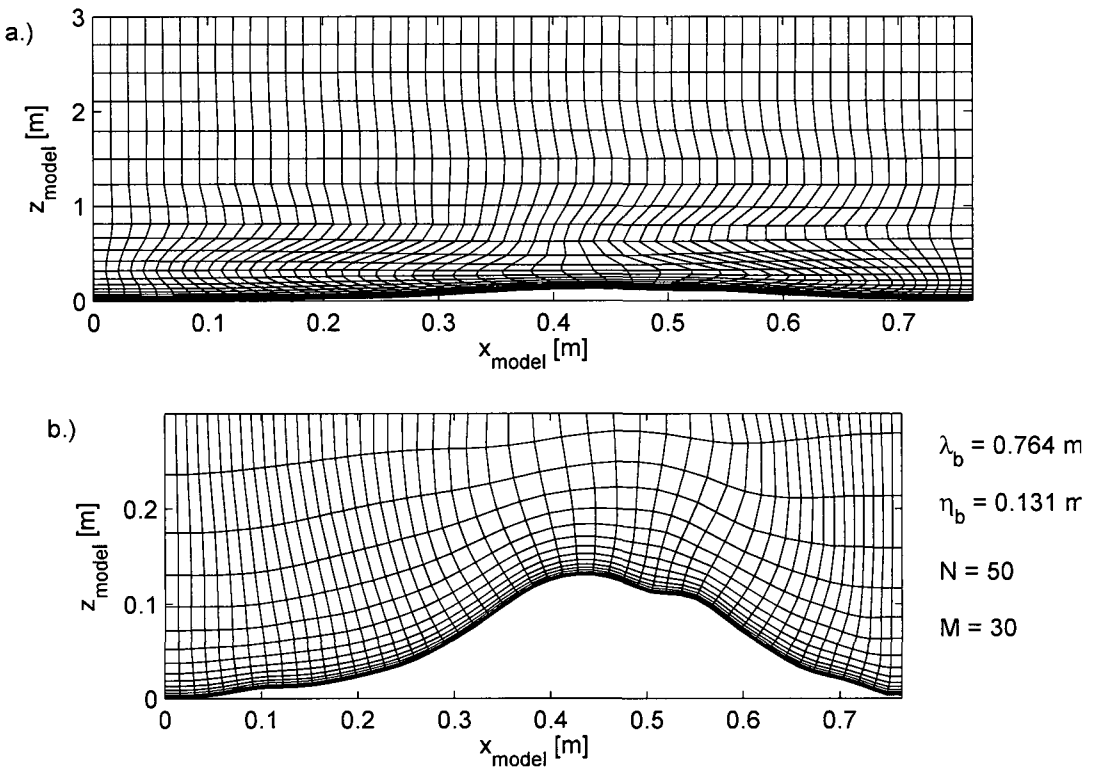

Figure 3-1: **Dune** grid example for burst 286. Three meter domain height with 50 horizontal (N) and 30 vertical (M) grid cells. The bedform has a wavelength (λ_b) and height (η_b) of 0.764 m and 0.131 m, respectively.

As there is low variability over the data set, one characteristic Sleath ripple (*Andersen*, 1999) was chosen to simulate flow over the bottom boundary for the range of bursts analyzed. Matlab^{TM} code used to generate this bedform can be found in Appendix B. This particular ripple is symmetric about its centerline, the ripple crest, and has an increased resolution near the crest. This produces a bedform which allows for improved model performance and stability in the highly dynamic region where the flow separation, high accelerations, and large stresses are expected. The characteristic bedform wavelength (λ_b) and height (η_b) were specified with the

mean profile computed over the entire sampling period (See Figure 3-2).

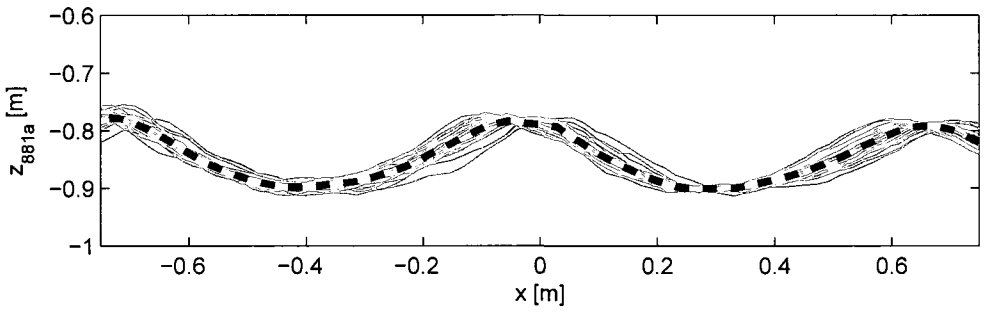

Figure 3-2: Hourly bedform profiles are shown in gray. Mean bedform profile represented by dashed black line. Horizontal position of profiler along profiles is at x = 0. Characteristic bedform size taken from mean bedform profile.

A hyperbolic grid generator was used to create a grid for these simulations with 50 cells in the horizontal (N) and 30 in the vertical (M). Grid cells are concentrated near the bed, and set to always contain two grid cells within the viscous sublayer. This allows the model to resolve the high shear in flows near the bottom boundary while satisfying the no slip condition. Thirty vertical grid cells and a domain height of three meters was chosen for this simulation, yielding a maximum vertical grid spacing of 0.4 meters at the top of the domain. Fifty horizontal grid cells were chosen to capture flow dynamics along the bedforms, which were all less than 1 meter in wavelength. The representative Sleath ripple with resulting grid is shown in Figure 1-3.

Model sensitivity to hydrodynamic forcing resolution was performed for a range of wave and current forcing conditions over the dataset. These representative datasets included the following burst numbers: 286, 289, 292, and 294. They represent profiles of maximum current magnitude in the flooding and ebbing tide,

as well as data sampled during slack tide conditions.

The spin-up of the flow field is performed in a series of steps to ensure numerical stability. First, a small time step (50,000 iterations per wave period) simulation is performed for a single sinusoidal wave. Second, a simulation is performed for 10 wave periods using the same time step. Third, a simulation with a coarser time step (1,000 iterations per wave period) is performed with the desired sinusoidal wave magnitude and direction, as well as mean current magnitude and direction. The simulation is run until the mean flow field has converged to its specified value. As the mean pressure gradient necessary for producing the desired current is unknown, the current is nudged into convergence through the use of a PID-control algorithm. This algorithm iteratively adjusts the pressure gradient based on the trends of the simulated current, until the desired current magnitude is attained (see *Frank* (2008) for details).

3.2 Coordinate Systems

Given the quasi-3D nature of the model, a coordinate transformation of the observations is required to align the along crest ripple direction with the along shore direction of the model. The hydrodynamic field observations were reported in terms of u_{max}, u_{min}, and w. The velocity in the direction of maximum variance in the horizontal velocity field is defined as u_{max}. Consequently, u_{min} is the velocity in the direction perpendicular to the wave direction. Finally, w represents vertical velocity. The ADV instrument records geographic heading in reference to magnetic North, as well as velocity magnitudes. This geographic heading represents the ori-

entation of the instrument frame itself (see Figure 2-1). To relate velocity direction (incident angles of u_{max} and u_{min}) to ripple orientation, geographic ADV heading is added to all angles. Ripple direction is determined by the peak in the spatial Fast Fourier Transform (FFT) of the bathymetry map as recorded by the Imagenex 881a pencil beam sonar. Thus, when rotated by ADV heading, hydrodynamic forcing orientations can be related directly to the direction of ripple profiles.

Figure 3-3: Field data directions in geographic coordinates. Thick gray line is ripple direction. Thin black line is wave direction.

Model direction is determined by the bedform, as bedforms are considered to be uniform in the along shore direction. Model directions are as follows: x is the horizontal dimension perpendicular to the ripple crest with positive onshore, y is the along-crest horizontal position, and z is the vertical direction with positive

upwards from the bedform profile minima. Figure 3-3 shows that wave direction is relatively consistent with ripple direction, and that ripple direction varies by only seven degrees over the record length. The ripple direction is taken to be zero in the model simulations, and subsequently wave and current angles (α_w and α_c, respectively) are rotated to the model's ripple oriented coordinate system. The u_{max} direction is calculated by adding the direction of horizontal velocity maximum variance to the orientation of the tripod to rotate horizontal velocity direction angles into geographic coordinates. The current angle is calculated by adding the resultant current direction in geographic coordinates to the u_{max} direction. Negative wave and current angles were increased by 360 degrees in order to avoid negative angles for model simulation and naming convention purposes (note: this has no impact on physics of the flow field).

3.3 Model Forcing Parameters

Simulations are performed for 3 cases of varying complexity. Case 1 features the simplest flow field with waves perpendicular to ripple crests in the absence of mean currents. Case 2 simulations are characterized by waves at angles of approach equivalent to those recorded in the observations. Sinusoidal waves, bichromatic wave field, and actual velocity time series are simulated for the Case 1 and Case 2 parameters. Finally, Case 3 simulates combined wave and mean current flow approaching the bedform at the angles measured in the observations. Case 3 simulations will include sinusoidal and bichromatic wave group forcing. For each case, bursts 286, 289, 292, and 294 are analyzed over the same representative Sleath

ripple. These bursts of interest are distinguished by the bold faced rows in Tables 3.1, 3.2, and 3.3.

Model forcing parameters were obtained from velocity measured by the ADV instrument, located roughly 40 cm above the bed. Sinusoidal waves simulations were specified to have a maximum velocity (u_w) of $\sqrt{2}\sigma_{u_{max}}$, where σ is standard deviation of velocity, and u_{max} is the ADV measured horizontal velocity in the direction of maximum variance in horizontal flow observations. This ensures that the standard deviation of the velocity field is equal to the standard deviation of the sinusoidal wave field simulated by the model. Current magnitude (u_c) is determined as the magnitude of the 10-minute time averaged horizontal components of velocity as measured by the ADV for each burst. The wave period, T, was calculated from the frequency of the spectral peak in the u_{max} velocity data time series for each burst.

Table 3.1 shows the sinusoidal wave forcing parameters for the purely two-dimensional waves-only simulations, defined as Case 1 simulations. Waves for this case were assumed to be perpendicular to the ripple crests, thus for model simulations, $\alpha_w = 0$. Table 3.2 shows the simulation forcing parameters for the quasi-3D waves-only at observed angles (no mean currents), defined as Case 2 simulations for sinusoidal waves. Table 3.3 shows the forcing parameters for the combined wave and current simulations, defined as Case 3 simulations, for sinusoidal waves. The forcing for the simulations match the observed magnitudes and directions for both the waves and mean currents.

In addition to combinations of sinusoidal waves and mean currents, real wave

Table 3.1: Case 1 simulations for sinusoidal waves at $\alpha_w = 0$ [deg]. The bold-faced values represent specific bursts analyzed in this investigation.

burst #	T **[cm/s]**	u_w **[cm/s]**
280	12	22
281	10	23
282	10	24
283	12	19
284	9	18
285	10	20
286	**10**	**20**
287	10	20
288	10	22
289	**10**	**20**
290	10	20
291	10	23
292	**10**	**19**
293	10	22
294	**9**	**20**
295	10	22
296	10	18
297	10	18
298	10	18
299	10	21
300	10	20
301	10	21
302	10	21
303	10	20
304	10	18
305	9	22

data as obtained by the ADV was also simulated. The ADV velocities were first filtered with a 3 standard deviation filter to remove any outlier data points. Then, ADV observations were filtered in the frequency domain, using a low pass filter with a cutoff of 0.5 Hz, to isolate the wave signal from higher frequency perturbations (signals with periods less than 2 seconds) in the velocity measurements. Figure 3-4 shows an example of ADV recorded velocities as well as the filtered time series used as the model input. It is important to note that 0.5 Hz cutoff filter reduces

Table 3.2: Case 2 simulations for sinusoidal waves at observed direction. The bold-faced values represent specific bursts analyzed in this investigation.

Burst #	**T [s]**	u_w **[cm/s]**	α_w **[deg]**
280	12	22	5
281	10	23	8
282	10	24	10
283	12	19	11
284	9	18	10
285	10	20	15
286	**10**	**20**	**11**
287	10	20	11
288	10	22	7
289	**10**	**20**	**7**
290	10	20	3
291	10	23	359
292	**10**	**19**	**6**
293	10	22	359
294	**9**	**20**	**5**
295	10	22	357
296	10	18	11
297	10	18	7
298	10	18	7
299	10	21	11
300	10	20	11
301	10	21	10
302	10	21	5
303	10	20	13
304	10	18	9
305	9	22	8

the magnitude of the extreme local maxima and minima in the velocity time series. Simulating these local extremities is hydrodynamically pertinent to accurately resolve the flow field characteristics. However, the chosen cutoff was necessary to remove higher frequency fluctuations not characterized by the wave signal. The local acceleration of the filtered velocity time series was used to approximate the horizontal pressure gradient by assuming linear wave theory. Herein, model simulations forced with the filtered ADV time seres will be referred to as "real" wave

Table 3.3: Case 3 simulations for sinusoidal waves and currents at observed magnitude and direction. The bold-faced values represent specific bursts analyzed in this investigation.

Burst #	**T [s]**	u_w **[cm/s]**	α_w **[deg]**	u_c **[cm/s]**	α_c **[deg]**
280	12	22	5	5	102
281	10	23	8	4	117
282	10	24	10	1	211
283	12	19	11	11	267
284	9	18	10	13	268
285	10	20	15	14	268
286	**10**	**20**	**11**	**15**	**268**
287	10	20	11	15	283
288	10	22	7	10	285
289	**10**	**20**	**7**	**0**	**39**
290	10	20	3	3	95
291	10	23	359	4	62
292	**10**	**19**	**6**	**6**	**86**
293	10	22	359	6	83
294	**9**	**20**	**5**	**2**	**113**
295	10	22	357	4	249
296	10	18	11	11	274
297	10	18	7	14	267
298	10	18	7	10	265
299	10	21	11	10	264
300	10	20	11	12	273
301	10	21	10	9	273
302	10	21	5	3	291
303	10	20	13	0	318
304	10	18	9	2	246
305	9	22	8	2	63

simulations.

Figure 3-5 shows ADV measured wave time series (top panel) and resulting spectrum (bottom panel) for burst 286. The filtered wave spectrum (Figure 3-5 bottom panel) shows a broad banded spectral peak for frequencies of 0.7 to 0.11 Hz for horizontal velocities in the wave direction. The addition of the spectrum for these frequencies causes the appearance of wave groups in the wave time series,

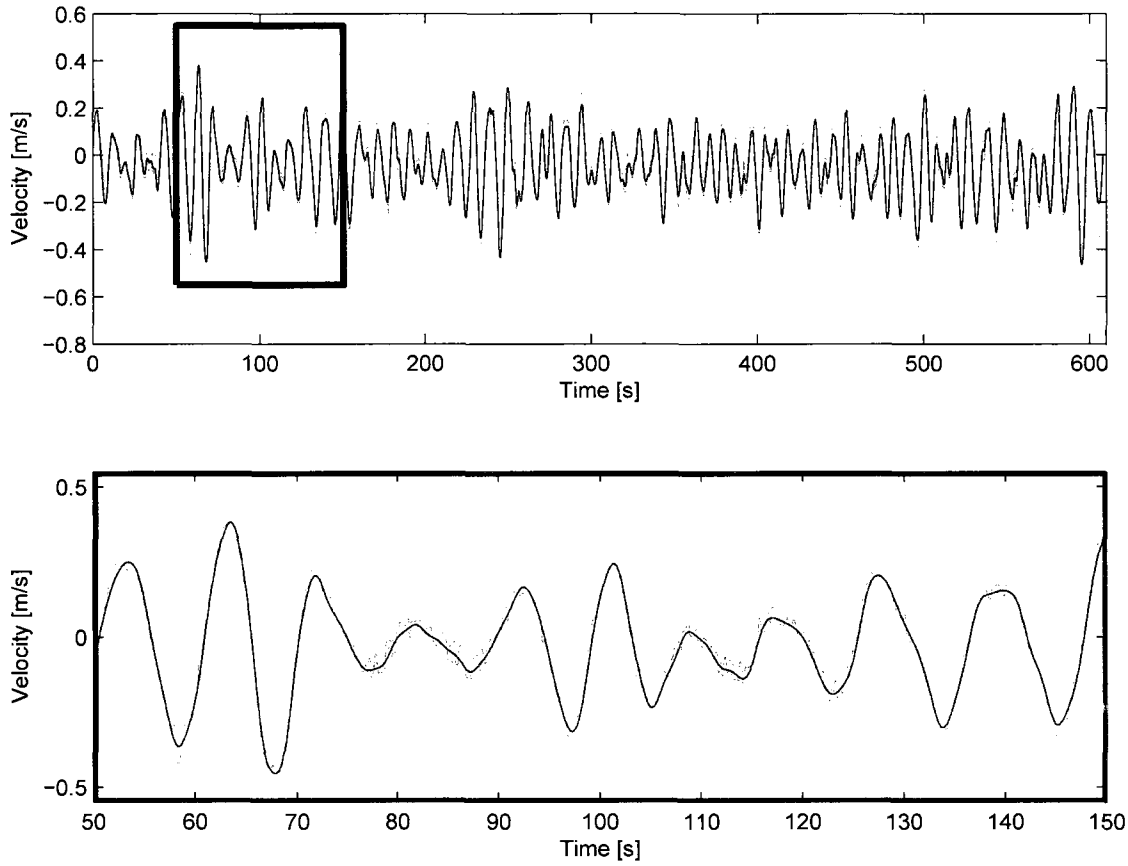

Figure 3-4: Real velocity time series model input example for burst 286. Gray line shows raw u_{max} velocity as calculated by the ADV. Black line shows integrated model input filtered acceleration time series. Top panel shows time series for full record. Bottom panel shows expanded view of full time series marked by gray box in top panel.

as shown in Figure 3-5 (top panel) for times of 30–90 s and 200–260 s. The wave group appearance in the wave direction velocity time series is similar for all cases investigated. Although the filtered spectrum does not show two significant peaks in this region (indicative of a truely bichromatic wave time series), a bichromatic time series is generated to simulate this wave group structure, as shown in Figure 3-6. Simulated bichromatic wave group time series are created by the vector addition of two sine waves of equal amplitude and differing frequency. The radian frequency of the incident sinusoid is set to $2\pi/T_{peak}$. The frequency of the second sinusoid is

calculated by the radian frequency of the desired group period (in this case, $2\pi/60$) less the radian frequency of the incident wave. Magnitudes of each sinusoid are set to the standard deviation of the ADV velocity in the wave direction, yielding a bichromatic velocity time series of equivalent standard deviation.

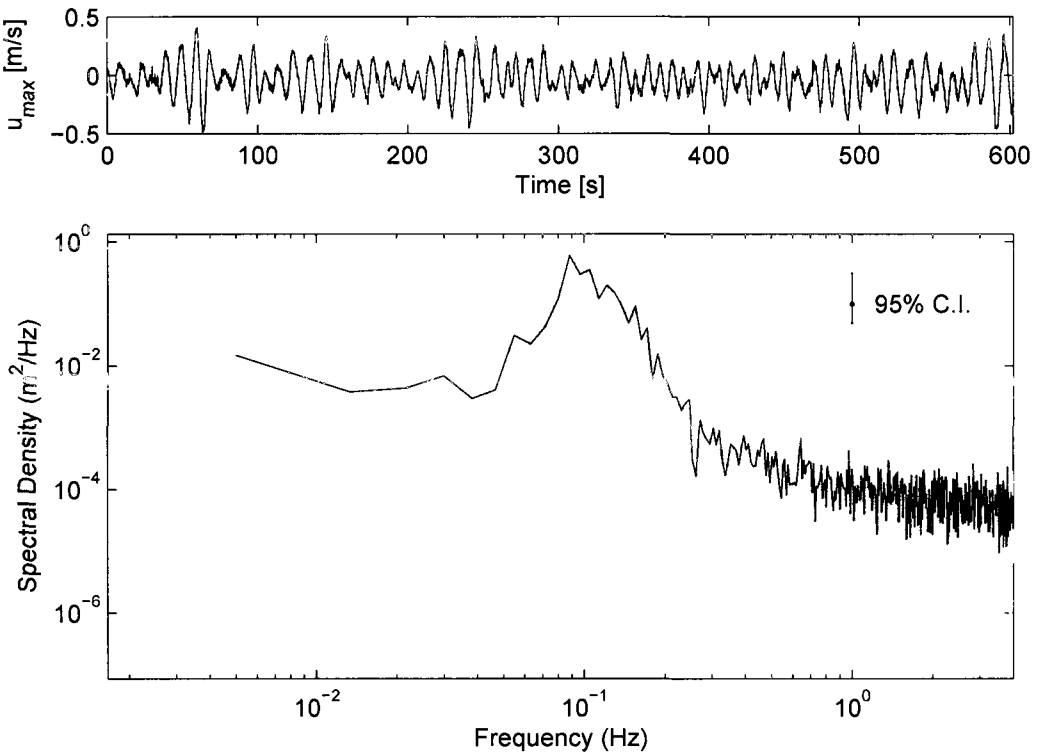

Figure 3-5: ADV measured wave time series (top) and resulting spectrum (bottom) for burst 286. The gray and black lines in the bottom panel show raw and band averaged spectrum with 10 degrees of freedom.

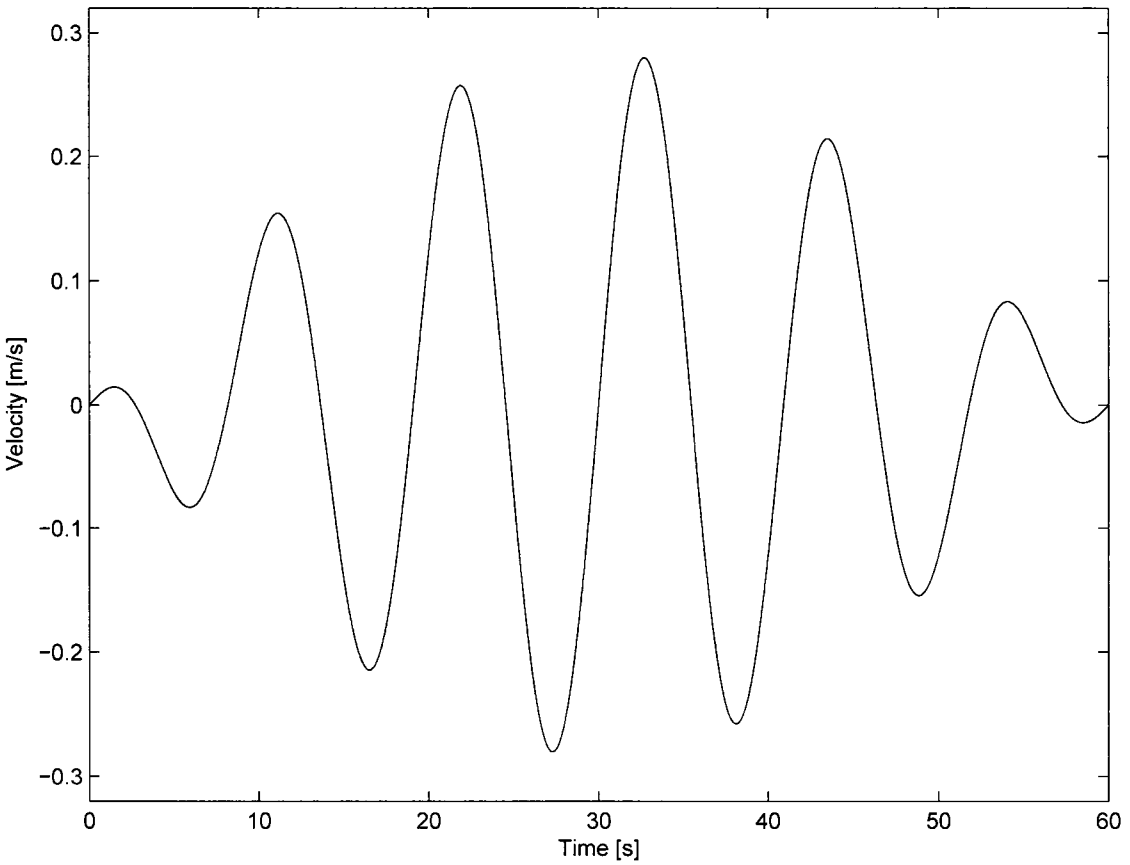

Figure 3-6: Bichromatic wave group time series example for burst 286. Waves have incident period of 10 seconds and group period of 60 seconds with a standard deviation equal to that of ADV observations in the u_{max} direction over the record length.

3.4 Determination of Bed Position

The Doppler profiler and ADV instrument vertical positions are known in reference to the footpads of the instrument frame. However, as the frame was positioned on a movable bed of coarse grained sediment, the bedform was migrating past the instrument array. Thus, it was necessary to determine local bed elevation under the Doppler profiler for each dataset. The Doppler profiler is an acoustic instrument that returns acoustic backscatter amplitude as a function of depth. As the wave climate was relatively calm and the sediment in the vicinity of the frame

was coarse grained, significant amounts of suspended sediment was not expected, as was confirmed by the amplitude of acoustic backscatter. Furthermore, ripples over the 10 minute record length were assumed stationary, and evolved little over the twenty-six hour record length (Figure 2-2). Consequently, the vertical profile of backscatter amplitude was temporally averaged to achieve a single mean profile over each record (see Figure 3-7).

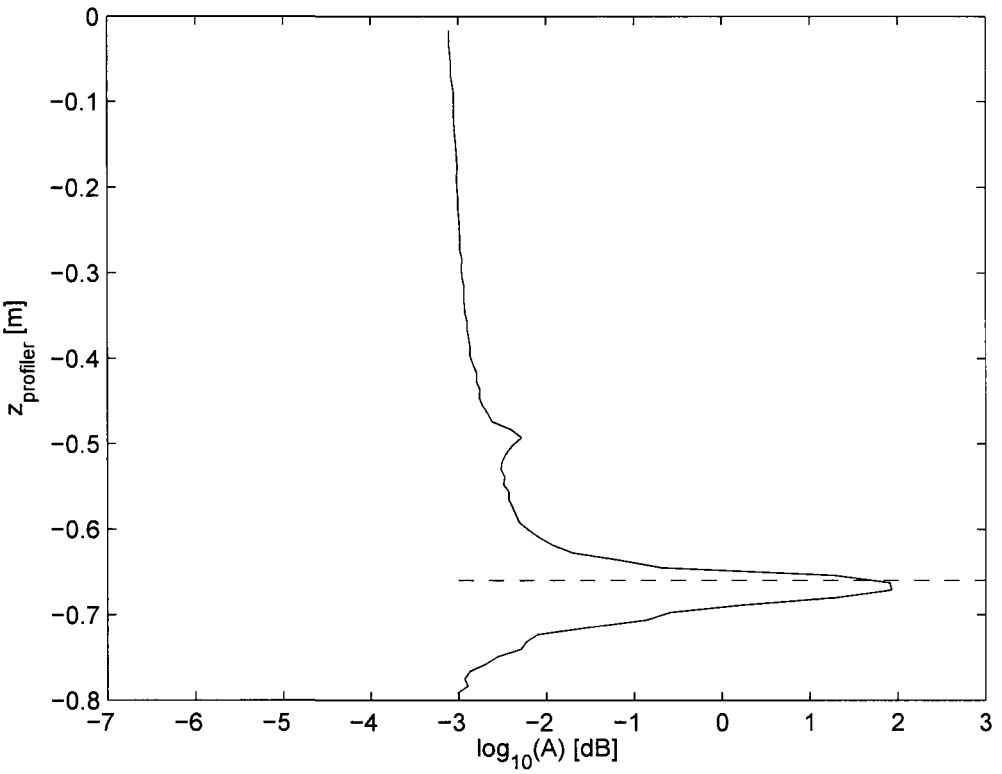

Figure 3-7: Temporal mean of vertical backscatter amplitude over a single 10 minute record as measured by the Doppler profiler for burst 286 in the vertical direction. The dashed line represents the location of maximum gradient in mean backscatter amplitude profile. Vertical axes is distance from the vertical Doppler profiler transducer, positive upwards

The maximum gradient of mean backscatter amplitude was assumed to be the local bed elevation. Figure 3-8 shows the gradient of mean backscatter profile.

Figure 3-9 shows the acoustic backscatter amplitude time series and approximated bed location for burst 286. Figure 3-7 shows the profile of time average of acoustic backscatter amplitude, with the black dashed line showing the position of the bed. After estimating the position of the bed, the vertical distance from the local bed to the ADV instrument was determined by the relation to the instrument frame and the distance from the profiler instrument to the bed.

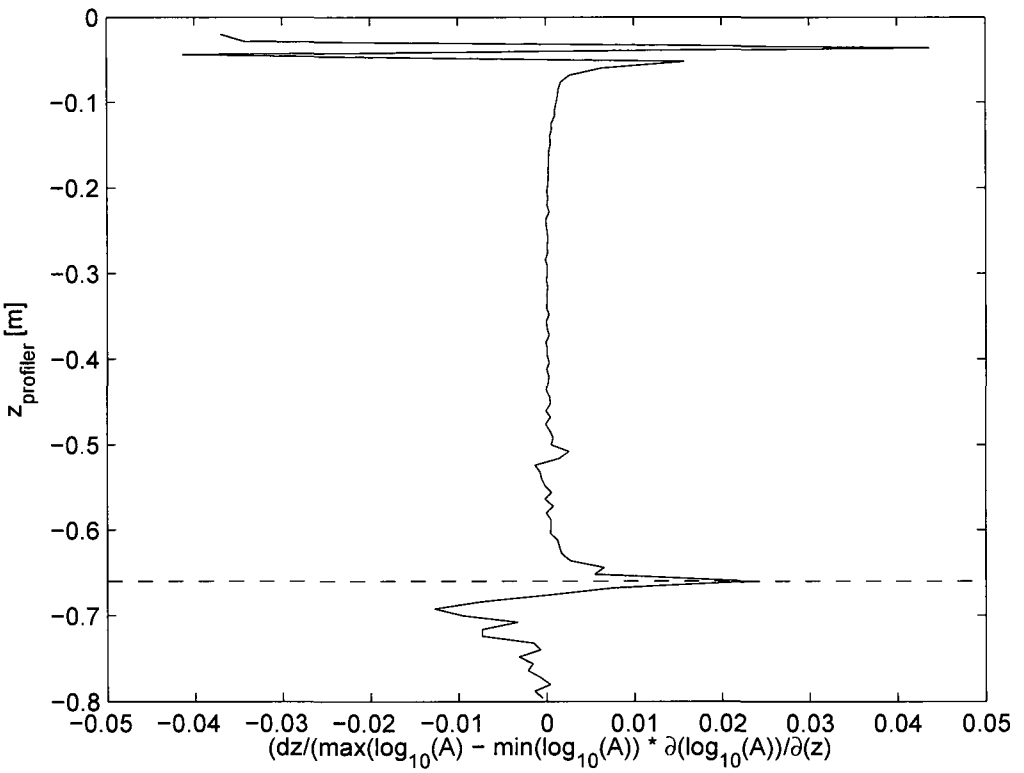

Figure 3-8: Normalized gradient of time-averaged vertical backscatter amplitude as measured by the Doppler profiler instrument for burst 286. The bed is assumed to be the vertical position of maximum gradient, represented by the dashed line. Large gradients near instrument head ($z_{profiler} = 0$) are due to near field instrument performance and flow interaction with instrument frame, and are therefore not included in the bed finding routine.

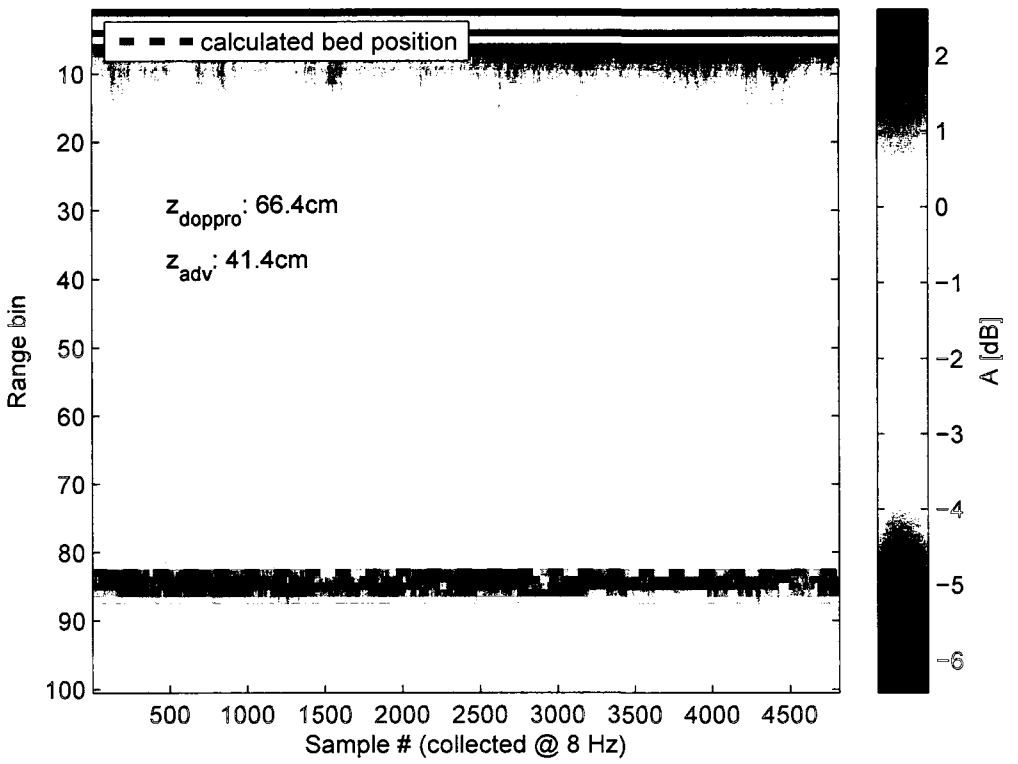

Figure 3-9: Vertical acoustic backscatter amplitude measured by the Doppler profiler for burst 286. Black dashed line represents vertical position of the bed as estimated by the maximum gradient in the mean backscatter amplitude profile (Figure 3-8).

3.5 Limitations of Doppler Profiler Observations

The measurements recorded by the Doppler profiler used in this investigation have limitations that must be explained prior to the ensuing analysis. At a distance above the crest, ranging from 10-17 cm ($z_{model} = 0.23 - 0.30$ m), there is a distinct change in the vertical shear of the vertical velocity (as observed by a local minima in the w_{std} profile). Above this local minima, w_{std} profiles increase significantly with distance from the bed. The elevation of the local minima is consistent with the elevation of a band of increased backscatter amplitude in the profiler data, as

can be seen in Figure 3-9. This increase in backscatter amplitude is most likely a contribution from side lobe returns from the transducer of the Doppler profiler (personal communication with P. Traykovski). At high elevations above the bed, measurements reveals flow interference with the instrument frame. For analysis purposes, only profiler data between the bedform crest and local minima due to side lobe returns were considered.

3.6 Model-Data Comparisons

In the following section, field observations are compared to model simulations for the three separate cases detailed in Section 3.3. Oscillatory flow over a bedform is temporally, as well as spatially variable. As such, to compare field observations with model simulations it is necessary to identify the equivalent position of the instrumentation on the simulated bedform. The algorithm used to determine the horizontal position of the Doppler profiler in respect to the representative ripple is as follows. First, the observed ripple height is determined by subtracting the height of the crest nearest the profiler from the minimum in the adjacent trough. The position of the Doppler profiler is known along the bedform. The non-dimensional vertical position of the profiler is calculated by the difference in the profiler elevation from the local minima in the adjacent ripple trough, divided by the height of the ripple. This non-dimensional height is then multiplied by the characteristic ripple height, resulting in the equivalent elevation of the instrument on the representative bedform. The horizontal position along the simulated ripple is then assumed to be the position with the estimated elevation on the appropriate side of the ripple

crest. Figure 3-10 shows an example of the profiler location at $x_{observations} = 0$ on the observed bedform (top panel), and the estimated equivalent position on the simulated Sleath ripple (bottom panel).

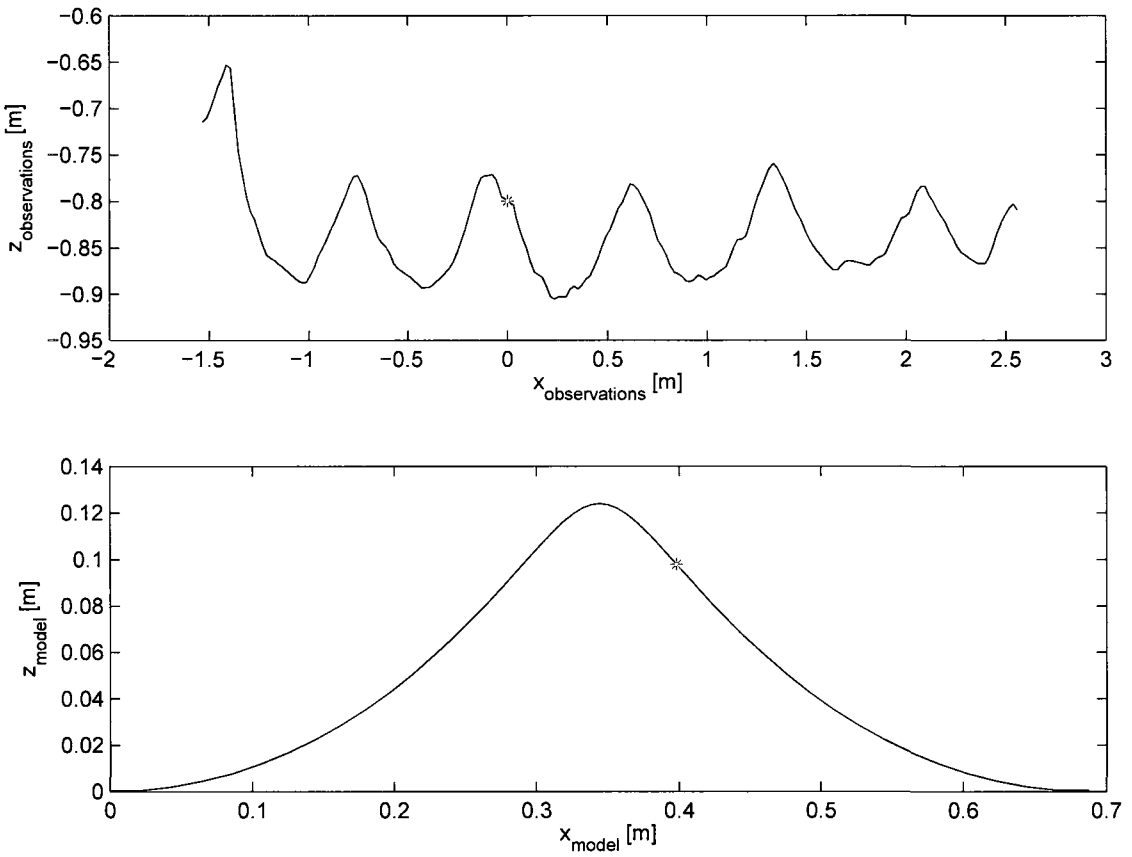

Figure 3-10: Equivalent horizontal position of Doppler profiler instrument on characteristic bedform for burst 286. The top panel shows the data bedform profile in black with the horizontal position of the profiler identified by the gray star. The bottom panel shows the simulated bedform profile with equivalent profiler location identified by the gray star.

Figure 3-11 shows bedform profiles and the Doppler profiler instrument location for each of the bursts analyzed in this investigation. The horizontal position of the black dashed line shows that the location of the Doppler profiler approaches the crest with increasing burst number. This is due to the steady ripple migration observed over the record. It is important to keep this variation in profiler position

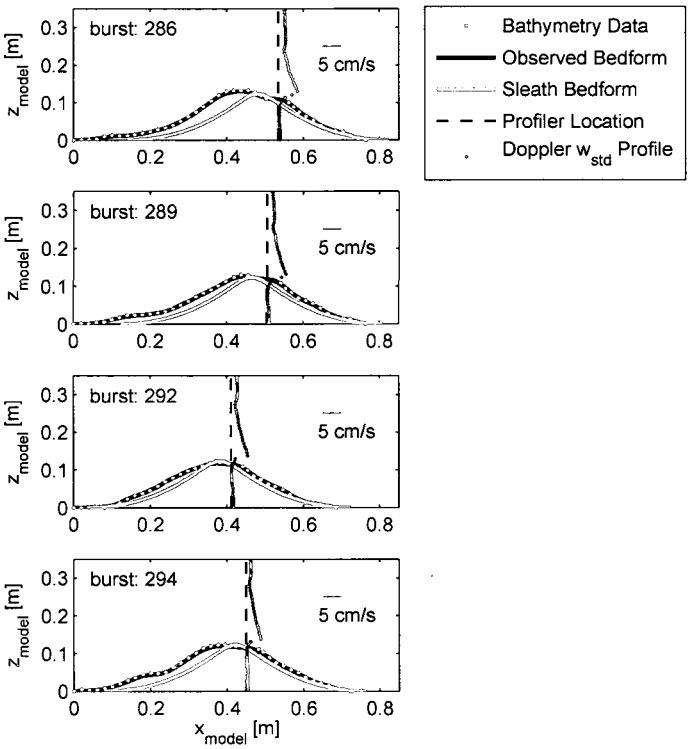

Figure 3-11: Observed and simulated bedforms and Doppler profiler locations for bursts analyzed. The green dots show pencil-beam sonar measured bathymetry profiles for the ripple at the Doppler profiler position. The black solid line shows the resampled and filtered bedform profile used for observed bedform model simulations. The brown line shows the characteristic Sleath bedform profile. The vertical black dashed line shows the lateral position of the Doppler profiler instrument. Each of the bedforms is aligned by the estimated Doppler profiler position. The red dots show the w_{std} profile as measured by the Doppler profiler. The scale in the upper left of each panel shows the scale of the profiler measurements with the black dashed line representing the position of zero velocity. The burst number for each of the panels is identified in the upper left corner.

in mind in the ensuing analysis, as it suggests that one must be careful when making direct comparisons between the data sets for the bursts analyzed. The filtered and resampled observed bedforms (black line) show favorable agreement with bedform profile as measured by the pencil-beam sonar (green dots). The characteristic Sleath ripple, shown as the brown line, shows reasonable agreement with observed bedform

profiles, however, often under-predicts the bedform wavelength, and over-predicts the steepness of the bedform at the profiler location. The standard deviation of vertical velocity profile for each of the bursts is shown by the red dots, with a scale in the upper right corner of each panel.

3.6.1 Case 1: Crest Normal Waves Over a Representative Bedform

In this section, waves are simulated over the characteristic Sleath bedform shown in Figure 1-3. The field observations are compared with model simulations with sinusoidal waves, a bichromatic wave group, and the real waves, all in the absence of steady currents. Each of the simulated profiles present in this section are characterized by incident waves approaching perpendicular to the bedform crest ($\alpha_w = 0$ [deg]).

Figure 3-12 shows standard deviation of vertical velocity (w_{std}) profiles for bursts 286 and 289, and Figure 3-13 shows w_{std} profiles for bursts 292 and 294. The field observations for the data sets show increasing vertical velocity with proximity to the bed with peak values of 4-5 cm/s. The local minima for each of the data sets ranges from 1 to 1.5 cm/s at an elevation of 10-16 cm from the ripple crest. The simulations show similar trends with vertical velocities increasing with proximity to the bed. The region between where the profiler bins reach the bed (bed intersect) and the bedform crest (area between red and lack dashed lines) contains the highest w_{std} magnitudes for each of the simulations, with the sinusoidal waves simulation being the greatest. In this region, flow is accelerating up the relatively steep face of the

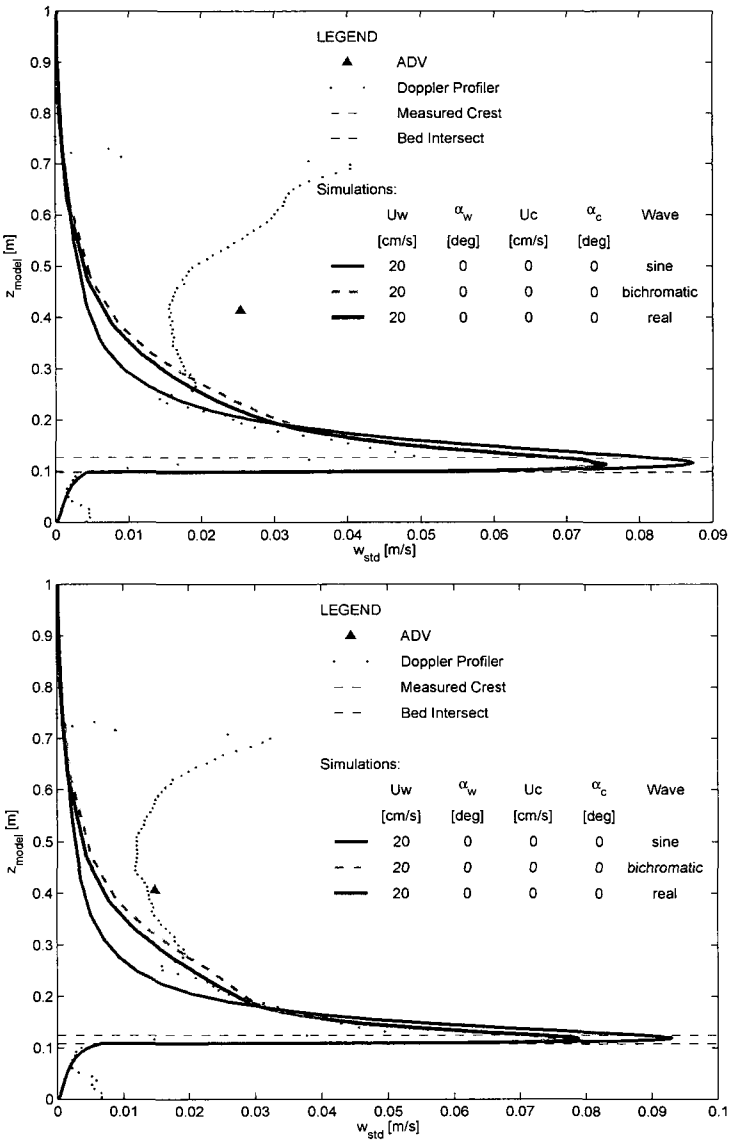

Figure 3-12: Case 1: w_{std} profiles for bursts 286 (top) and 289 (bottom). The triangle represents single point velocity measurements recorded by the ADV. The red dotted profile shows Doppler profiler observations. The black dashed line reveals the height above the vertical model datum at which the profiler sampling volume reaches the bed. The red dashed line shows the vertical position of the crest of the actual bedform recorded by the pencil beam sonar. The blue, green-dashed, and gray lines represent model simulations with sinusoidal waves, bichromatic wave groups, and real wave data, respectively.

bedform, thus yielding significant contributions to vertical velocities. Maximum w_{std} velocities of bichromatic wave groups and simulated wave time series data

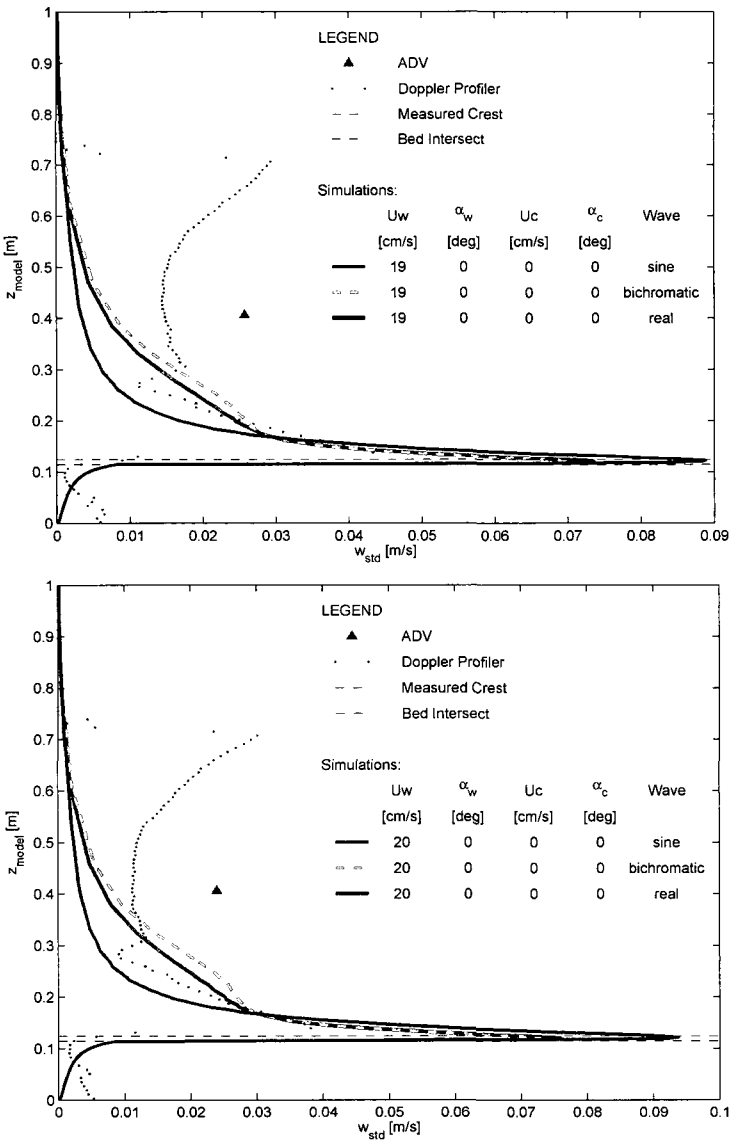

Figure 3-13: Case 1: w_{std} profiles for bursts 292 (top) and 294 (bottom). The triangle represents single point velocity measurements recorded by the ADV. The red dotted profile shows Doppler profiler observations. The black dashed line reveals the height above the vertical model datum at which the profiler sampling volume reaches the bed. The red dashed line shows the vertical position of the crest of the actual bedform recorded by the pencil beam sonar. The blue, green-dashed, and gray lines represent model simulations with sinusoidal waves, bichromatic wave groups, and real wave data, respectively.

have similar profiles in this region, with real wave time series yielding slightly larger maximum values, both typically around 15% less than maximum standard

deviation velocities simulated by sinusoidal waves only. Maximum w_{std} velocities measured by the Doppler profiler in this very near-bed region are significantly lower than those predicted by model simulations. While the observations may show lower amplitudes due to bottom reflections or profile bin locations, the model likely over estimates the velocity near the bed due to the large shear and high accelerations required to satisfy the no slip condition.

As distance from the bed increases, above the bedform crest, w_{std} decreases significantly. The most dramatic decrease occurs with the sinusoidal wave simulations with high shear within the first 10 cm above the ripple crest. w_{std} profiles for bichromatic and real wave simulations are nearly identical in the first 6 cm above the bedform crest before bichromatic simulated profiles diverge with slightly higher w_{std} values higher in the water column. Unlike the observations, simulations of w_{std} approach zero, satisfying the rigid lid assumption for the shallow water waves. The higher w_{std} values from 0.2 to 0.5 m from the bed result from a thicker boundary layer likely induced by the modulating wave amplitude signal in the bichromatic and real wave forcing. Measured w_{std} profiles most closely follow the measured wave time series simulations in both profile shape and magnitude in the first 15 cm above the bedform crest.

Vertical standard deviation velocities measured by the ADV are significantly greater than any of the profiles, simulated or measured. Although the ADV record was temporally shifted to match the Doppler profiler time series, the location of the instrument with respect to the bedform profile remains unknown. This unknown relative position of the instrument may be the cause for the discrepancy in w_{std}

values. Furthermore, the inability of the model to simulate wave orbital motion in the vertical direction may also result in discrepancies between model simulations and the ADV point measurement.

Standard deviation velocity profiles for horizontal velocity perpendicular to ripple crests (u_{std}) are shown in Figures 3-14 and 3-15. Similar to w_{std} profiles, u_{std} are all relatively consistent for each record analyzed. For each of the Case 1 simulations, u_{std} profiles increase from zero at the bed to a maximum value just above the ripple crest. This is to be expected, as flow accelerates over the bedform at the ripple crest, with most of the contributions to velocity in the u direction. The largest maximum u_{std} values are consistently from wave group simulations, with the second largest being real wave simulations, and finally sinusoidal wave simulations.

As distance from the bed increases, simulated profiles decrease monotonically, approaching their free stream u_{std} value. Free stream u_{std} values of model simulations are generally achieved within 0.4 m of the ripple crest. Profiles show that bichromatic waves introduce the greatest amount of shear higher into the water column, with pure sinusoidal wave forcing introducing the least shear at increased distance from the bed, with results least like the real wave simulations.

ADV velocities for u_{std} are much more consistent with simulation profiles, as compared to the w_{std} study. This is to be expected, as the simulations for this investigation were based on the values recorded by the ADV. Doppler profiler u_{std} values reveal a similar shape to simulation profiles near the bed with magnitudes significantly smaller. However, no quantitative analysis can be performed on horizontal Doppler profiler data for the reasons described in the observations section.

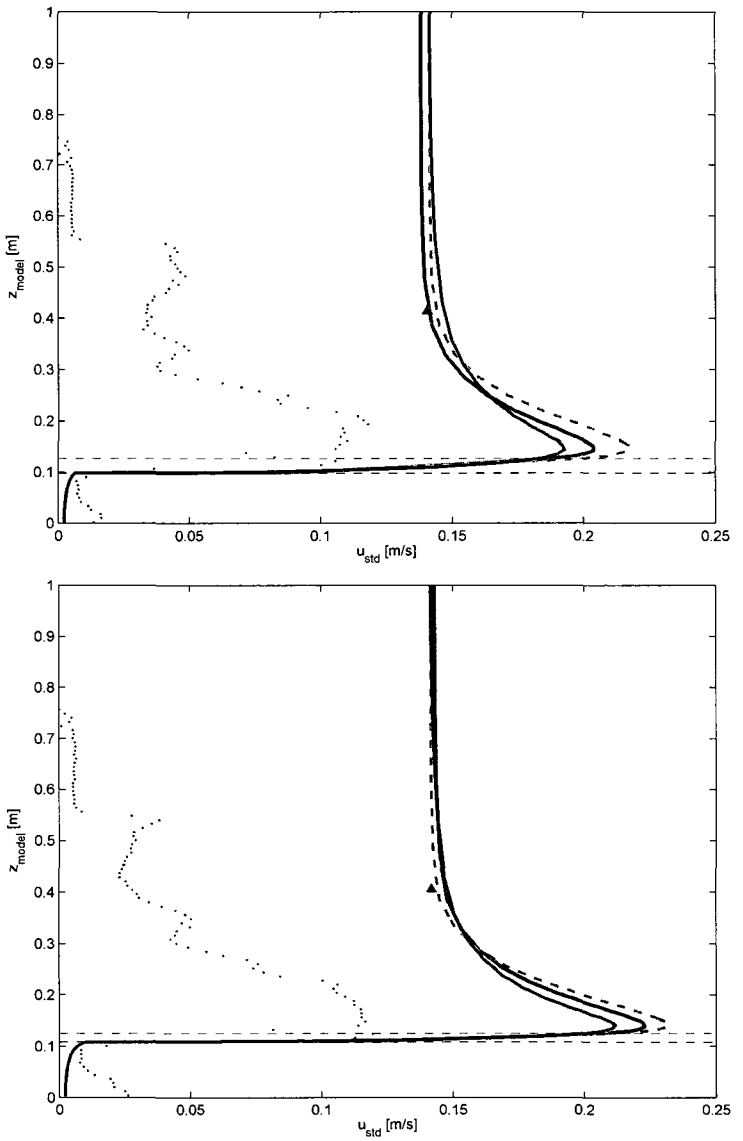

Figure 3-14: Case 1: u_{std} profiles for bursts 286 (top) and 289 (bottom). The triangle represents single point velocity measurements recorded by the ADV. The red dotted profile shows Doppler profiler observations. The black dashed line reveals the height above the vertical model datum at which the profiler sampling volume reaches the bed. The red dashed line shows the vertical position of the crest of the actual bedform recorded by the pencil beam sonar. The blue, green-dashed, and gray lines represent model simulations with sinusoidal waves, bichromatic wave groups, and real wave data, respectively.

3.6.2 Case 2: Waves at Angles Over a Representative Bedform

Case 2 presents model predictions of wave flows at an angle over fixed Sleath

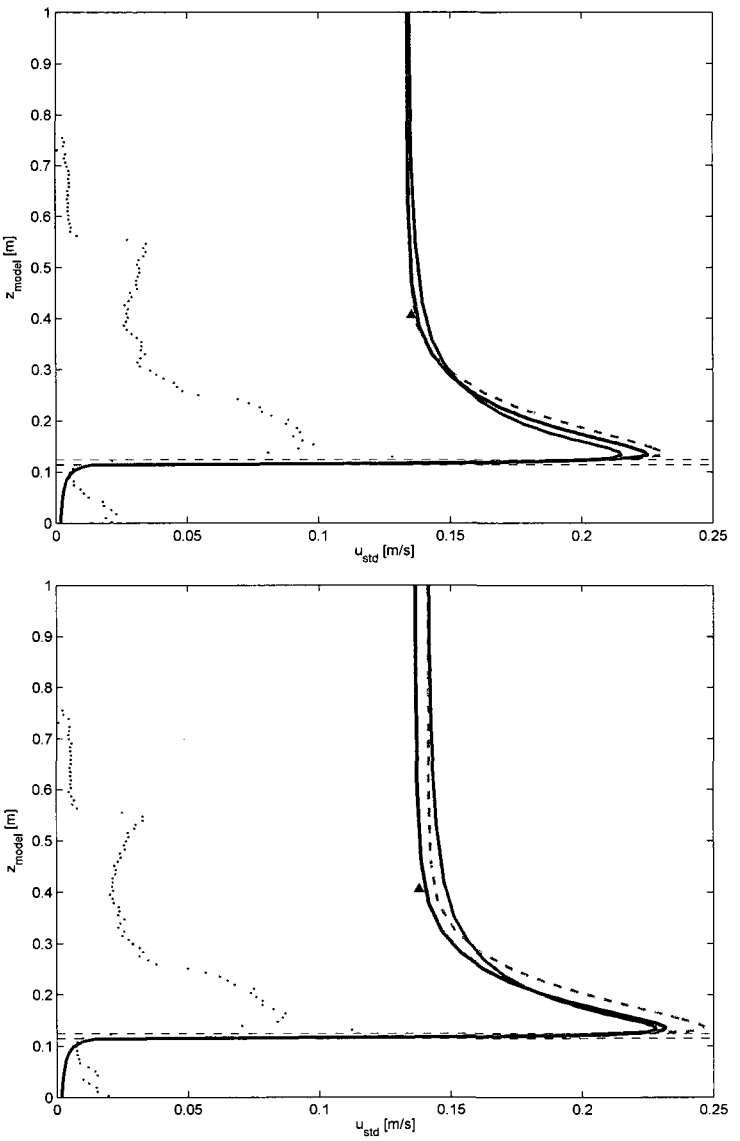

Figure 3-15: Case 1: u_{std} profiles for bursts 292 (top) and 294 (bottom). The triangle represents single point velocity measurements recorded by the ADV. The red dotted profile shows Doppler profiler observations. The black dashed line reveals the height above the vertical model datum at which the profiler sampling volume reaches the bed. The red dashed line shows the vertical position of the crest of the actual bedform recorded by the pencil beam sonar. The blue, green-dashed, and gray lines represent model simulations with sinusoidal waves, bichromatic wave groups, and real wave data, respectively.

bedforms. Similar to Case 1, no mean currents were present in these simulations.

Wave magnitudes and angles of approach for the simulations of this section are

presented in Table 3.2. Throughout the data set, waves approached at acute angles, never larger than 15 degrees from the crest perpendicular direction.

Figure 3-16 shows model-data comparisons for Case 2 w_{std} simulation profiles for bursts 286 and 289, and Figure 3-17 shows Case 2 w_{std} profiles for bursts 292 and 294. Wave angles (α_w) for these particular data sets vary between 5 and 11 degrees. Similar to Case 1, Case 2 maximum simulation values for w_{std} profiles are located below the ripple crest elevation. Sinusoidal waves have largest maximum magnitudes ranging between 8.7 and 9.5 cm/s. Real waves and bichromatic wave group simulations have maximum magnitudes within 20% of the sinusoidal wave simulations. Doppler w_{std} profiles have maximum values of approximately half that of the sinusoid simulation profiles.

As distance from the bed is increased, Case 2 profiles show similar trends to the Case 1 investigation. Lower frequency signals in the real wave and bichromatic wave group simulations result in a thicker boundary layer than the sinusoidal simulations when 0.2 m $< z_{model} <$ 0.6 m. In this elevation range, bichromatic wave groups show the thickest boundary layer of all the simulations investigated. At elevations above $z_{model} = 0.6$ m, simulations converge and tend to 0 satisfying the model's rigid lid assumption at the top of the domain ($z_{model} = 3$ m).

It is important to note that sinusoidal wave simulations produce nearly identical w_{std} profiles for Case 1 and Case 2 parameters. Only burst 286 (where $\alpha_w = 11$ degrees) in Figure 3-16 (top) reveals slight deviations in maximum w_{std} magnitude just below the ripple crest between Case 1 and Case 2, with the remainder of the profile for these two cases remaining identical. This suggests that the model is

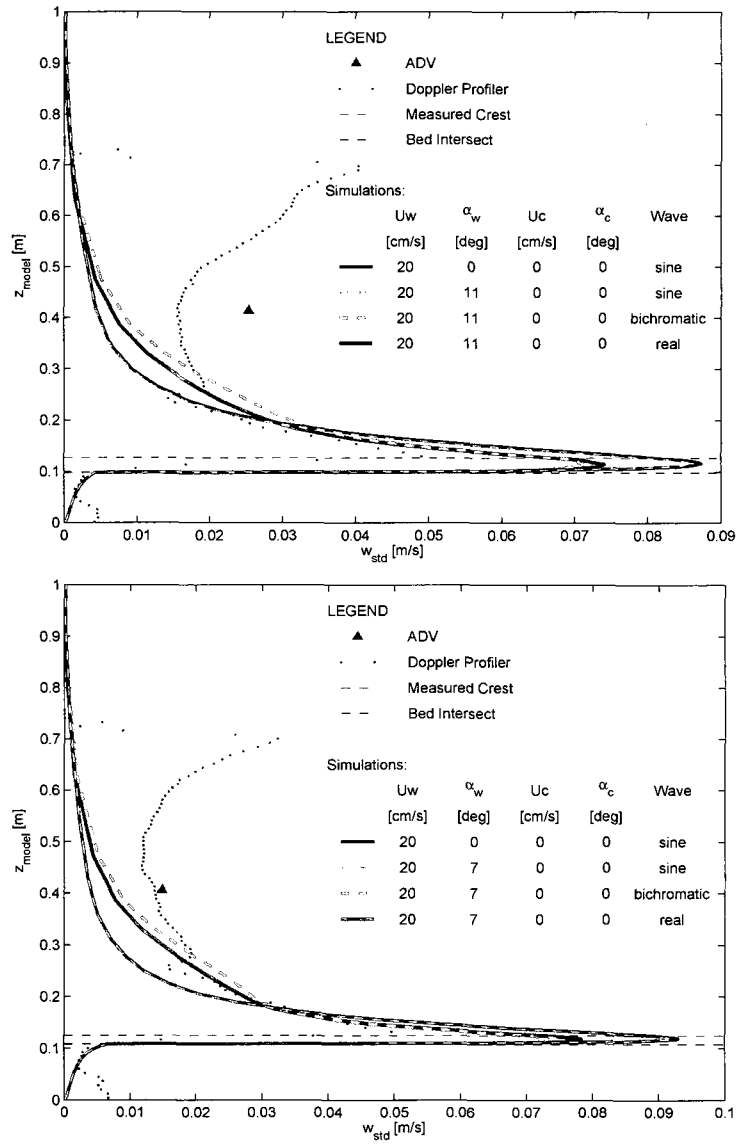

Figure 3-16: Case 2: w_{std} model-data comparison profiles for bursts 292 (top) and 294 (bottom). The triangle represents single point velocity measurements recorded by the ADV. The red dotted profile shows Doppler profiler observations. The black dashed line reveals the height above the vertical model datum at which the profiler sampling volume reaches the bed. The red dashed line shows the vertical position of the crest of the actual bedform recorded by the pencil beam sonar. The light blue dashed, green dashed, and gray lines represent Case 2 model simulations with sinusoidal waves, bichromatic wave groups, and real wave data, respectively. The solid blue line shows a sinusoidal wave simulation profile at $\alpha_w = 0$ (Case 1) for comparison.

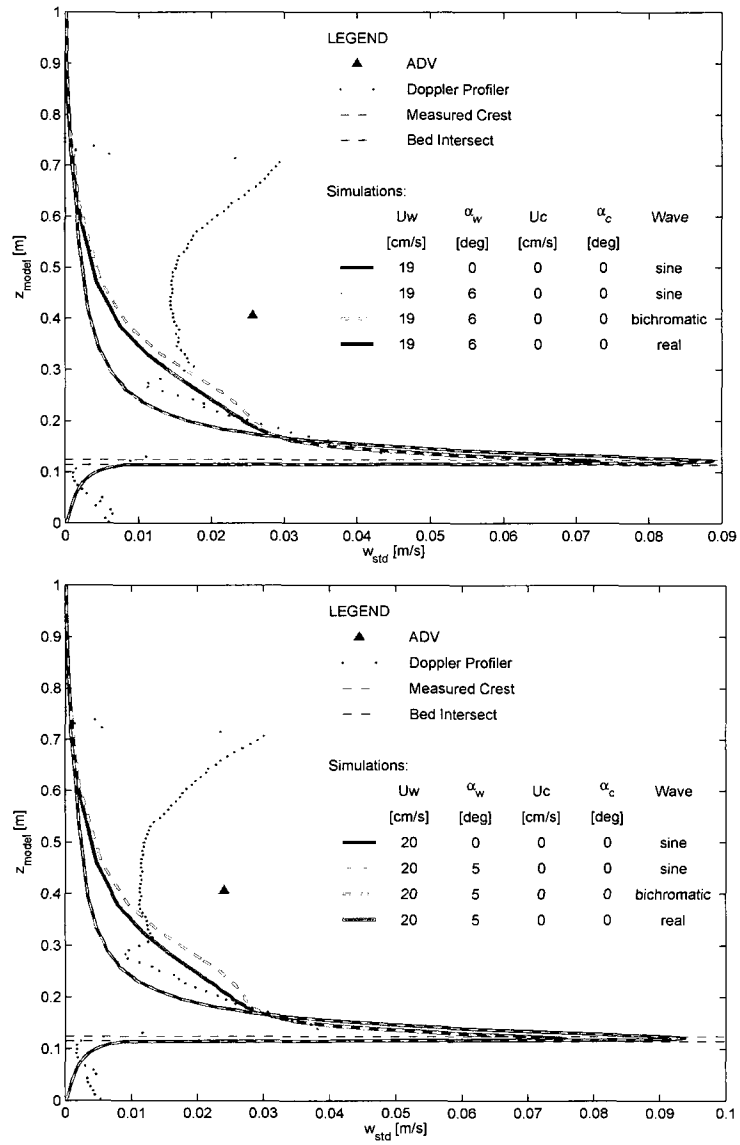

Figure 3-17: Case 2: w_{std} model-data comparison profiles for bursts 292 (top) and 294 (bottom). The triangle represents single point velocity measurements recorded by the ADV. The red dotted profile shows Doppler profiler observations. The black dashed line reveals the height above the vertical model datum at which the profiler sampling volume reaches the bed. The red dashed line shows the vertical position of the crest of the actual bedform recorded by the pencil beam sonar. The light blue dashed, green dashed, and gray lines represent Case 2 model simulations with sinusoidal waves, bichromatic wave groups, and real wave data, respectively. The solid blue line shows a sinusoidal wave simulation profile at $\alpha_w = 0$ (Case 1) for comparison.

insensitive to the slight angles investigated in Case 2 for w_{std} profiles. Case 2 real wave velocity simulations in the near bed region most closely follow the Doppler profiler measurements in the near bed region, as is consistent with the Case 1 analysis.

Figure 3-18 shows Case 2 u_{std} profiles for bursts 286 and 289, and Figure 3-19 shows u_{std} profiles for bursts 292 and 294. Bichromatic wave group simulations are responsible for the largest magnitudes of u_{std}, followed by real waves, then finally sinusoidal waves. Bichromatic wave group simulations have the thickest boundary layer up to an elevation of $z_{model} = 0.25$ m. Above this point, sinusoidal wave simulations maintain a thicker boundary layer. Profiles of u_{std} tend to converge at $z_{model} = 0.6$ m, and extend vertically to the free stream value. Case 2 simulations for burst 286 (see Figure 3-18 top) shows that u_{std} profiles are more sensitive to wave angle than w_{std} profiles, as the pure sinusoid wave simulation for $\alpha_w = 11$ degrees is noticeably different from the sinusoidal simulation when $\alpha_w = 0$ degrees. For the smaller wave angle cases investigated ($\alpha_w < 8$ degrees), there is no difference in u_{std} profile from the Case 1 simulations. This suggests that at the crest, simulated wave angles are relatively insignificant in u_{std} profiles until wave angle increases above 10 degrees.

The wave bottom boundary layer dynamics are sensitive to the horizontal position along the ripple. The distance between the bed intersect and the bedform crest decreases as burst number increases, as is made evident by the decrease in the spacing between black and red dashed horizontal lines. This is due to a steady ripple migration of approximately 0.5 cm/hour across the instrument array. This

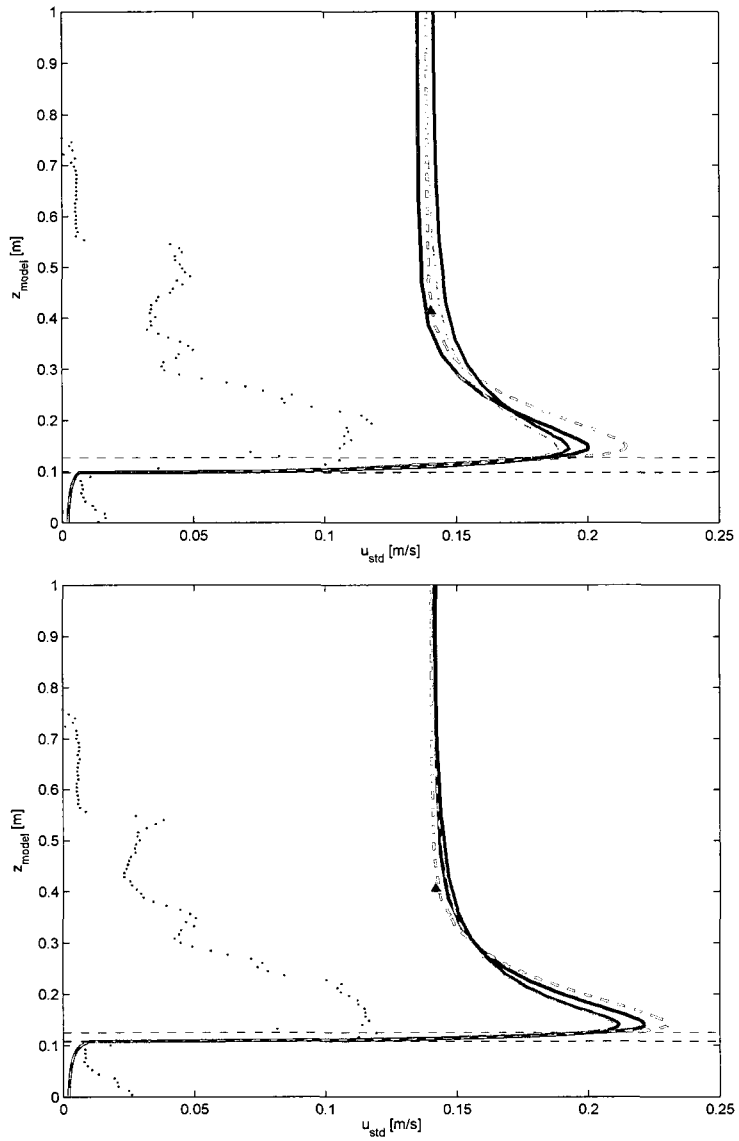

Figure 3-18: Case 2: u_{std} model-data comparison profiles for bursts 292 (top) and 294 (bottom). The triangle represents single point velocity measurements recorded by the ADV. The red dotted profile shows Doppler profiler observations. The black dashed line reveals the height above the vertical model datum at which the profiler sampling volume reaches the bed. The red dashed line shows the vertical position of the crest of the actual bedform recorded by the pencil beam sonar. The light blue dashed, green dashed, and gray lines represent Case 2 model simulations with sinusoidal waves, bichromatic wave groups, and real wave data, respectively. The solid blue line shows a sinusoidal wave simulation profile at $\alpha_w = 0$ (Case 1) for comparison.

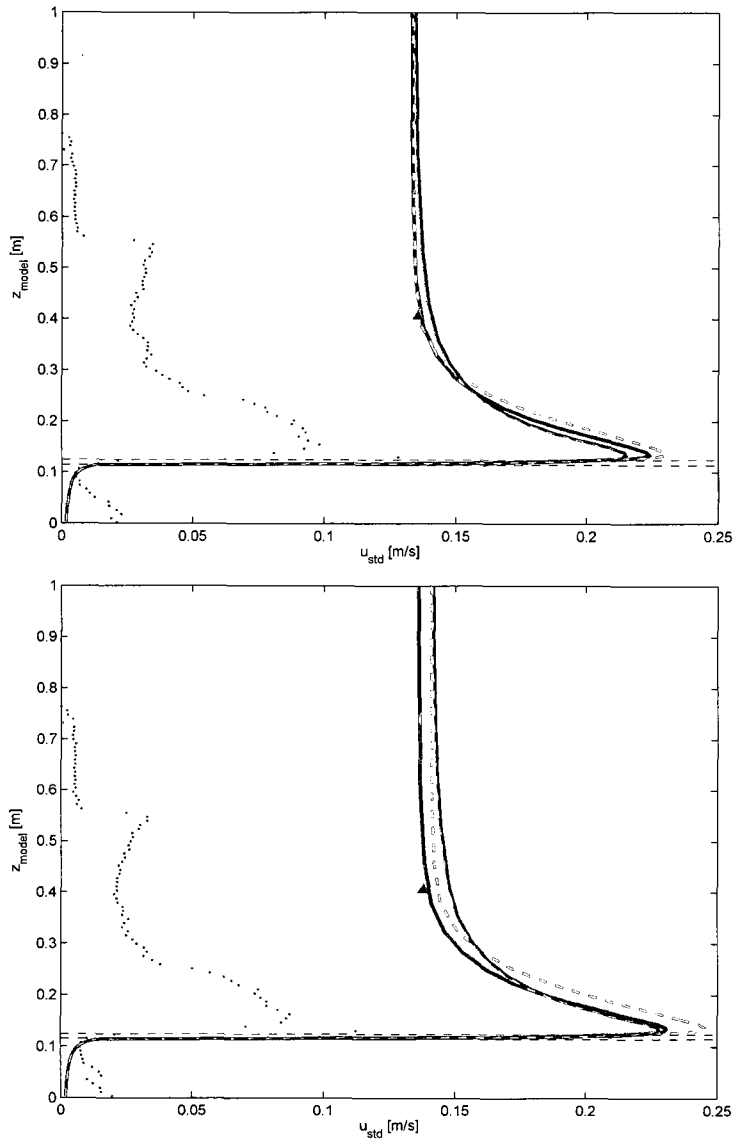

Figure 3-19: Case 2: u_{std} model-data comparison profiles for bursts 292 (top) and 294 (bottom). The triangle represents single point velocity measurements recorded by the ADV. The red dotted profile shows Doppler profiler observations. The black dashed line reveals the height above the vertical model datum at which the profiler sampling volume reaches the bed. The red dashed line shows the vertical position of the crest of the actual bedform recorded by the pencil beam sonar. The light blue dashed, green dashed, and gray lines represent Case 2 model simulations with sinusoidal waves, bichromatic wave groups, and real wave data, respectively. The solid blue line shows a sinusoidal wave simulation profile at $\alpha_w = 0$ (Case 1) for comparison.

results in an increase in the overshoot region above the ripple crest in the u_{std} profile. The large jet in u_{std} profile is likely due to the position of the profile along the ripple. This shows that there is greater variability in crest-normal velocity in the near bed region as the profile approaches the ripple crest position. This is investigated further in section 3.7.

In the near crest position, lower frequency signals have less of an impact on the shear above the ripple crest than was observed in vertical velocity profiles in the locations analyzed. This is shown by the smaller variability in u_{std} profiles between the various simulations as distance from the bed is increased.

Figure 3-20 shows model-data comparisons for Case 2 v_{std} simulation profiles for bursts 286 and 289, and Figure 3-21 shows Case 2 v_{std} simulation profiles for bursts 292 and 294. Observed velocities are significantly greater than the simulated velocities for any of the simulated profiles at the profiler location, and is suggestive of an error in the model forcing. Contrary to u_{std} profiles, v_{std} profiles show no overshoot region of large standard deviation velocities in the near-bed region. Rather, v_{std} profiles for Case 2 model simulations increase slightly from their value at the bed intersect, and achieve free stream values just above the ripple crest elevation. v_{std} are most sensitive to wave angles of approach. Figures 3-20 and 3-21show that α_w is directly proportional to v_{std} profile values for the acute angles investigated in this study. Each of the bursts investigated show that v_{std} is insensitive to wave climates simulated. Profiles for sinusoids, bichromatic wave groups, and real wave data lie directly on top of one another for similar wave angles of approach.

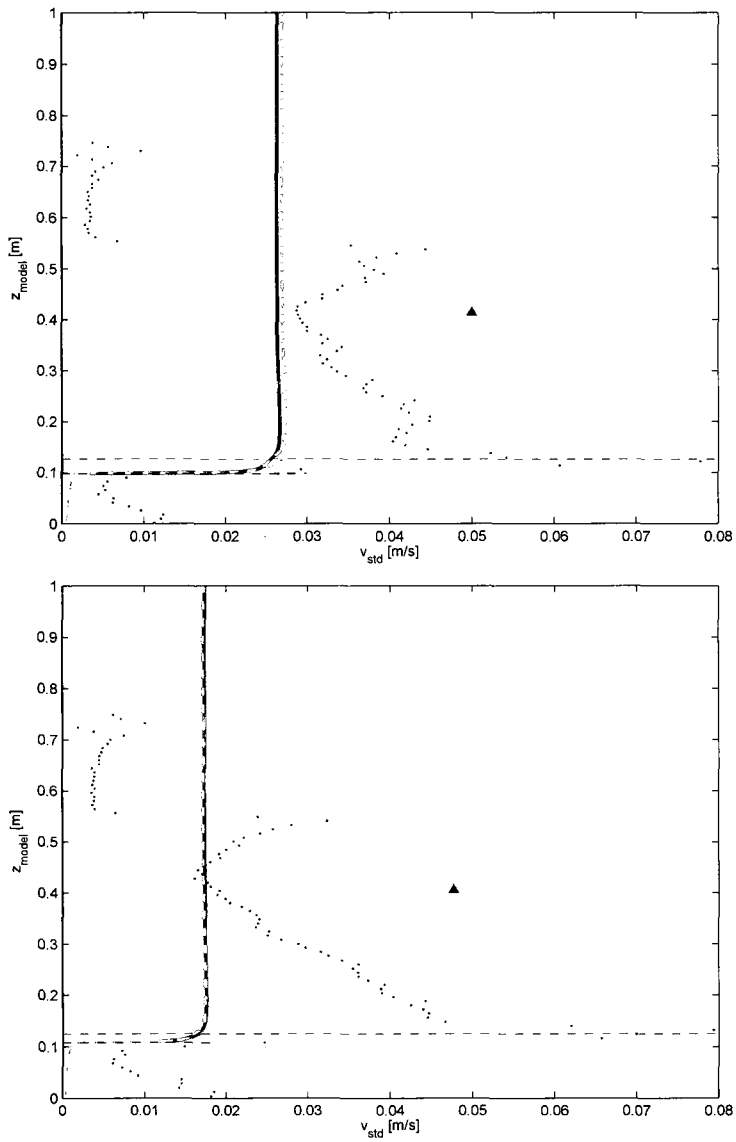

Figure 3-20: Case 2: v_{std} model-data comparison profiles for bursts 292 (top) and 294 (bottom). The triangle represents single point velocity measurements recorded by the ADV. The red dotted profile shows Doppler profiler observations. The black dashed line reveals the height above the vertical model datum at which the profiler sampling volume reaches the bed. The red dashed line shows the vertical position of the crest of the actual bedform recorded by the pencil beam sonar. The light blue dashed, green dashed, and gray lines represent Case 2 model simulations with sinusoidal waves, bichromatic wave groups, and real wave data, respectively. The solid blue line shows a sinusoidal wave simulation profile at $\alpha_w = 0$ (Case 1) for comparison.

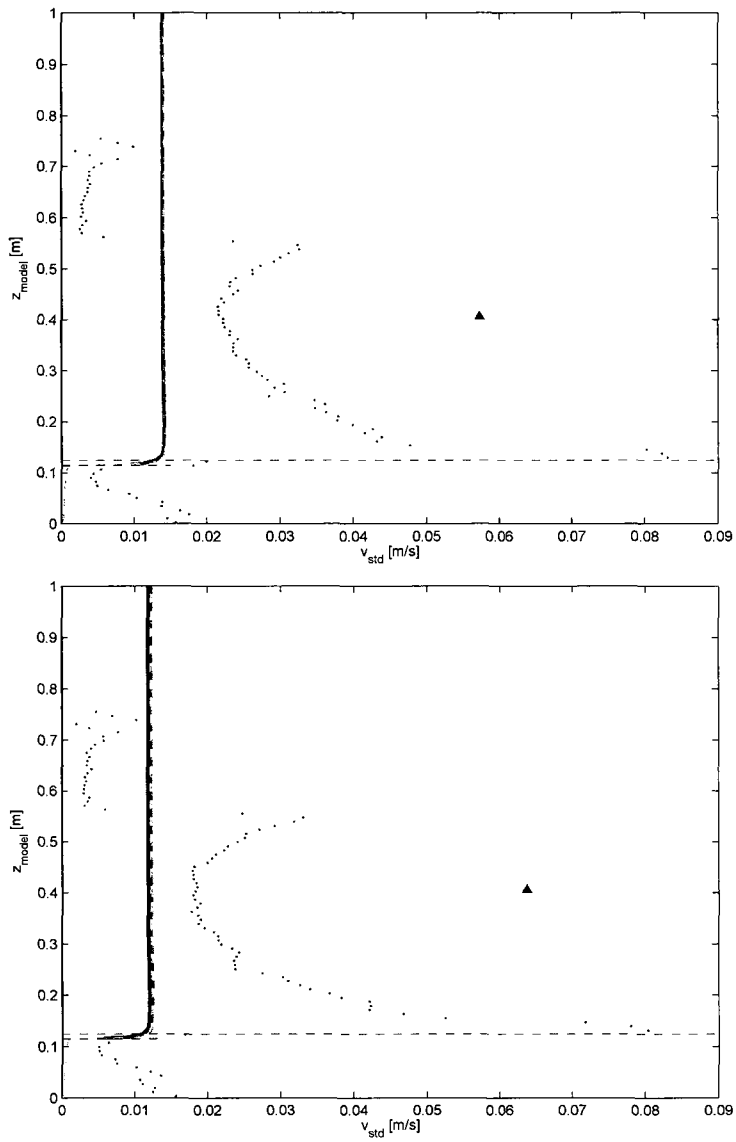

Figure 3-21: Case 2: v_{std} model-data comparison profiles for bursts 292 (top) and 294 (bottom). The triangle represents single point velocity measurements recorded by the ADV. The red dotted profile shows Doppler profiler observations. The black dashed line reveals the height above the vertical model datum at which the profiler sampling volume reaches the bed. The red dashed line shows the vertical position of the crest of the actual bedform recorded by the pencil beam sonar. The light blue dashed, green dashed, and gray lines represent Case 2 model simulations with sinusoidal waves, bichromatic wave groups, and real wave data, respectively. The solid blue line shows a sinusoidal wave simulation profile at $\alpha_w = 0$ (Case 1) for comparison.

3.6.3 Case 3: Combined Waves and Currents Over a Representative Bedform

In this section, simulations of combined wave and current flow over a fixed Sleath bedform are presented and compared to field observations. Current velocities are calculated as the magnitude of the mean components of the u_{min} and u_{max} velocity signal as measured by the ADV. The angle at which the currents approach the bed is calculated by the tangent of its mean u_{min} and u_{max} components, rotated to the ripple oriented coordinate system. Sinusoidal waves and bichromatic wave group simulations were performed for this combined flow case. Currents range from 0 to 15 cm/s for the cases investigated.

Figure 3-22 shows Case 3 w_{std} model-data comparisons for bursts 286 and 289, and Figure 3-23 shows Case 3 w_{std} model-data comparisons for bursts 292 and 294. Similar to Cases 1 and 2, maximum w_{std} magnitudes of 8.5 to 9.5 cm/s result from sinusoidal wave simulations and are located just below the crest elevation for each of the bursts investigated. Case 3 bichromatic wave simulations show slightly lower maximum w_{std} velocities, ranging from 7 to 7.5 cm/s at the profiler location. Sinusoidal waves for Case 1 and Case 3, shown by the blue and orange lines, are nearly identical throughout the entire profile. This suggests that the wave bottom boundary layer is insensitive to combined waves and currents at angles for sinusoidal waves for w_{std} profiles. This result is consistent with previous efforts, also with sinusoidal waves and mean currents, that have shown that currents have minimal impact on the wave bottom boundary layer (*Grant and Madsen*, 1979; *Frank*, 2008).

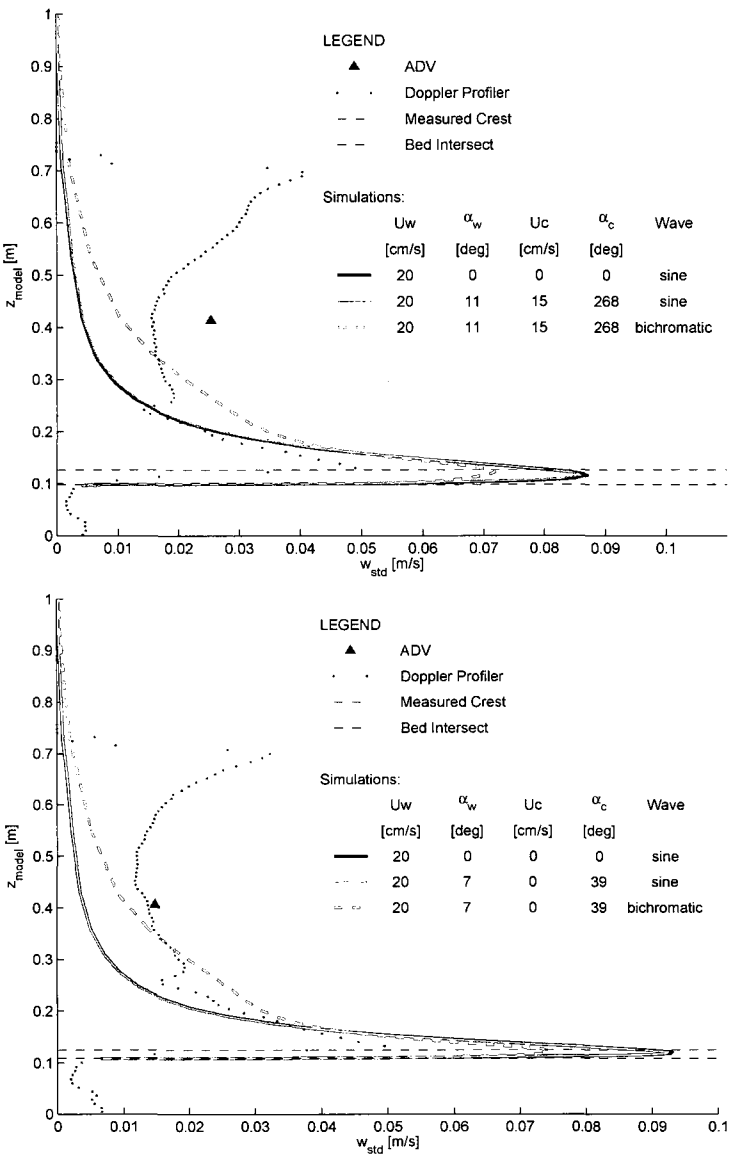

Figure 3-22: Case 3: w_{std} model-data comparison profiles for bursts 286 (top) and 289 (bottom). The triangle represents single point velocity measurements recorded by the ADV. The red dotted profile shows Doppler profiler observations. The black dashed line reveals the height above the vertical model datum at which the profiler sampling volume reaches the bed. The red dashed line shows the vertical position of the crest of the actual bedform recorded by the pencil beam sonar. The orange and green dashed lines represent Case 3 model simulations with sinusoidal waves, bichromatic wave groups, respectively. The solid blue line shows a sinusoidal wave simulation profile at $\alpha_w = 0$ (Case 1) for comparison.

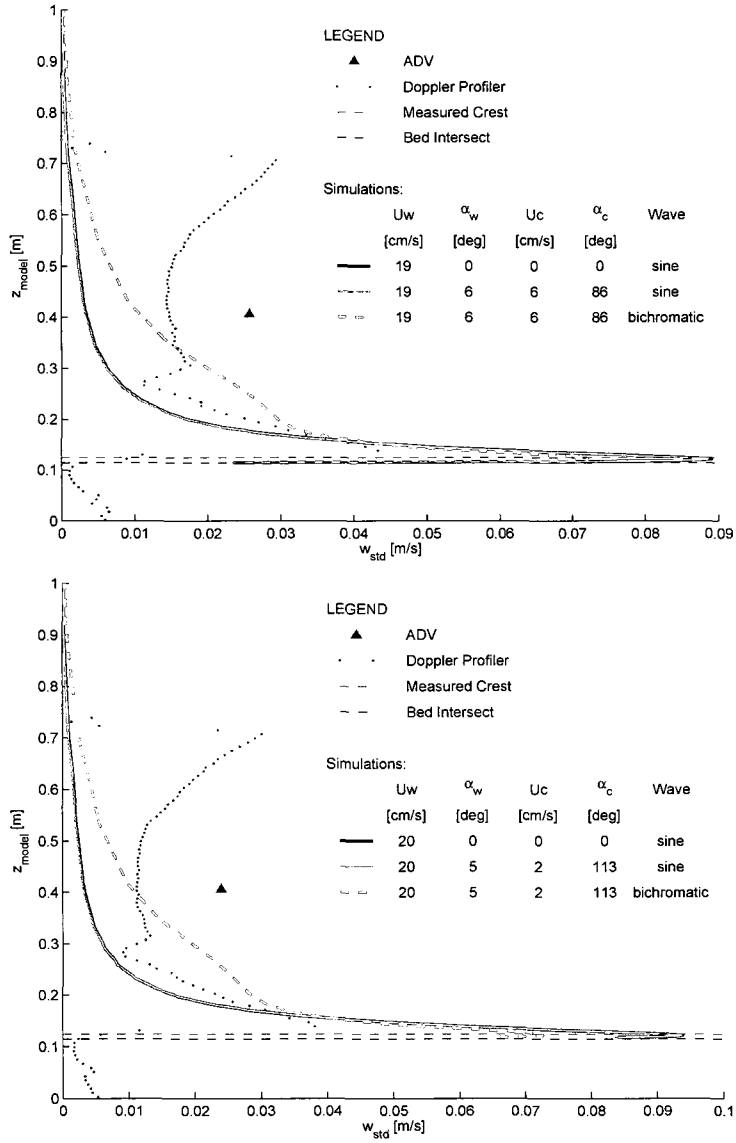

Figure 3-23: Case 3: w_{std} model-data comparison profiles for bursts 292 (top) and 294 (bottom). The triangle represents single point velocity measurements recorded by the ADV. The red dotted profile shows Doppler profiler observations. The black dashed line reveals the height above the vertical model datum at which the profiler sampling volume reaches the bed. The red dashed line shows the vertical position of the crest of the actual bedform recorded by the pencil beam sonar. The orange and green dashed lines represent Case 3 model simulations with sinusoidal waves, bichromatic wave groups, respectively. The solid blue line shows a sinusoidal wave simulation profile at $\alpha_w = 0$ (Case 1) for comparison.

Bichromatic wave groups, however, differ significantly from the sinusoidal wave simulations at distances greater than 8 cm above the ripple crest. Velocity mag-

nitude modulations in the bichromatic wave group simulations results in a significantly thicker boundary layer for z_{model} elevations of 0.20 to 0.90 m and allow for more interactions with the current boundary layer. The decrease in the w_{std} profiles is nearly linear for 0.2 m $< z_{model} <$ 0.4 m, with a significantly gentler slope than observed for sinusoidal wave simulations. Above $z_{model} = 0.9$ m, bichromatic and sinusoidal simulations converge to zero, satisfying the rigid lid assumption for shallow water waves. The sinusoidal wave and bichromatic wave group simulations both over estimate the standard deviation profile measured by the Doppler profiler at the estimated horizontal profiler location. For the cases analyzed, sinusoidal wave simulations better predict the Doppler profiler data. However, the lack of data at $z_{model} > 0.25$ m precludes a complete evaluation of the vertical velocity dynamics at greater distances from the bed.

The mean current has a negligible effect on sinusoidal wave forcing, however, it results in a significant expansion of the boundary layer when combined with the bichromatic wave forcing. It is assumed, but not proven here, that combined wave and current simulations using measured wave velocities would also result in an expanded boundary layer and increased dynamics above the bed, due to the similarities in the bichromatic and real wave simulations for Cases 1 and 2. In the present effort, it was not possible to simulate combined wave and current flow at observed angles using real wave forcing due to numerical instability issues with the model. As with Cases 1 and 2 at the profiler location, standard deviation of vertical ADV velocity time series is significantly larger than those predicted for bichromatic and sinusoidal wave simulations.

Figure 3-24 shows Case 3 u_{std} model-data comparisons for bursts 286 and 289, and Figure 3-25 shows Case 3 u_{std} model-data comparisons for bursts 292 and 294. Simulations reveal that superimposing waves on currents for model simulations has a negligible effect on u_{std} profiles. Resulting profiles for sinusoidal wave simulations are consistent with those simulations of Case 2. Superimposing waves onto currents for bichromatic wave groups, however, does result in a slight vertical displacement of the u_{std} profile. This is consistent with the findings of *Fredsøe et al.* (1999) who found that to superimpose wave and current forcing resulted in a vertical displacement of the boundary layer profile. Simulation profiles are consistent with ADV velocity measurements, which is expected, as ADV horizontal velocity statistics were used to force the model.

Figure 3-26 shows Case 3 v_{std} model-data comparisons for bursts 286 and 289, and Figure 3-27 shows Case 3 v_{std} model-data comparisons for bursts 292 and 294. Similar to Cases 1 and 2, ADV observations are significantly larger than any of the simulations predict for the elevation and position along on the bedform. It is likely that the model was under-forced in this direction and therefore ADV velocities are expected to be greater. For the largest current and wave angle case of this investigation presented in burst 286 (see Figure 3-26 top panel), the combination of waves and currents has significant effects on the v_{std} profile in the very near-bed region. Free stream v_{std} velocities range from 1 to 3 cm/s for the bursts investigated with larger values for larger current angles. Rather than increasing sharply to their free stream value, v_{std} profiles show significantly more variability near the bedform, below the data crest, than did the simulations in the absence of currents. This

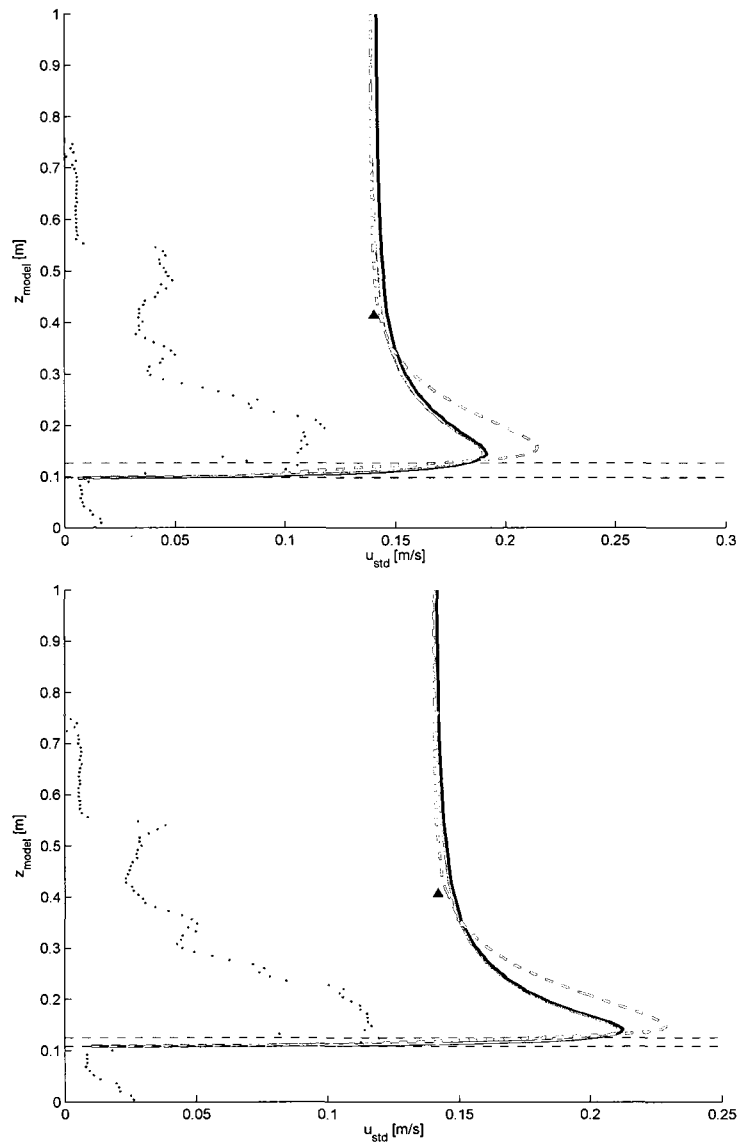

Figure 3-24: Case 3: u_{std} model-data comparison profiles for bursts 286 (top) and 289 (bottom). The triangle represents single point velocity measurements recorded by the ADV. The red dotted profile shows Doppler profiler observations. The black dashed line reveals the height above the vertical model datum at which the profiler sampling volume reaches the bed. The red dashed line shows the vertical position of the crest of the actual bedform recorded by the pencil beam sonar. The orange and green dashed lines represent Case 3 model simulations with sinusoidal waves, bichromatic wave groups, respectively. The solid blue line shows a sinusoidal wave simulation profile at $\alpha_w = 0$ (Case 1) for comparison.

is shown by the local maxima in the v_{std} profile just below the ripple crest. This results in a deformation of the profile that has effects up to 0.5 m above the ripple

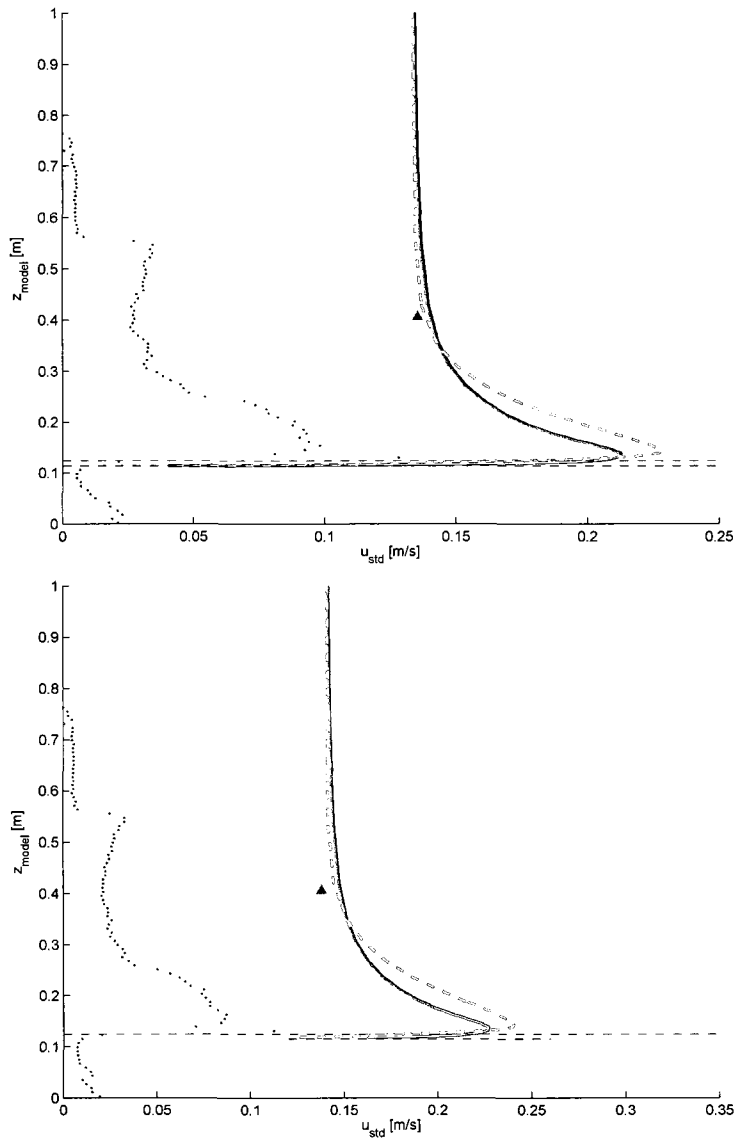

Figure 3-25: Case 3: u_{std} model-data comparison profiles for bursts 292 (top) and 294 (bottom). The triangle represents single point velocity measurements recorded by the ADV. The red dotted profile shows Doppler profiler observations. The black dashed line reveals the height above the vertical model datum at which the profiler sampling volume reaches the bed. The red dashed line shows the vertical position of the crest of the actual bedform recorded by the pencil beam sonar. The orange and green dashed lines represent Case 3 model simulations with sinusoidal waves, bichromatic wave groups, respectively. The solid blue line shows a sinusoidal wave simulation profile at $\alpha_w = 0$ (Case 1) for comparison.

trough. Above the ripple crest, v_{std} decreases slowly to its free stream value. Burst 292 reveals a slight vertical displacement in the bichromatic wave group simulation

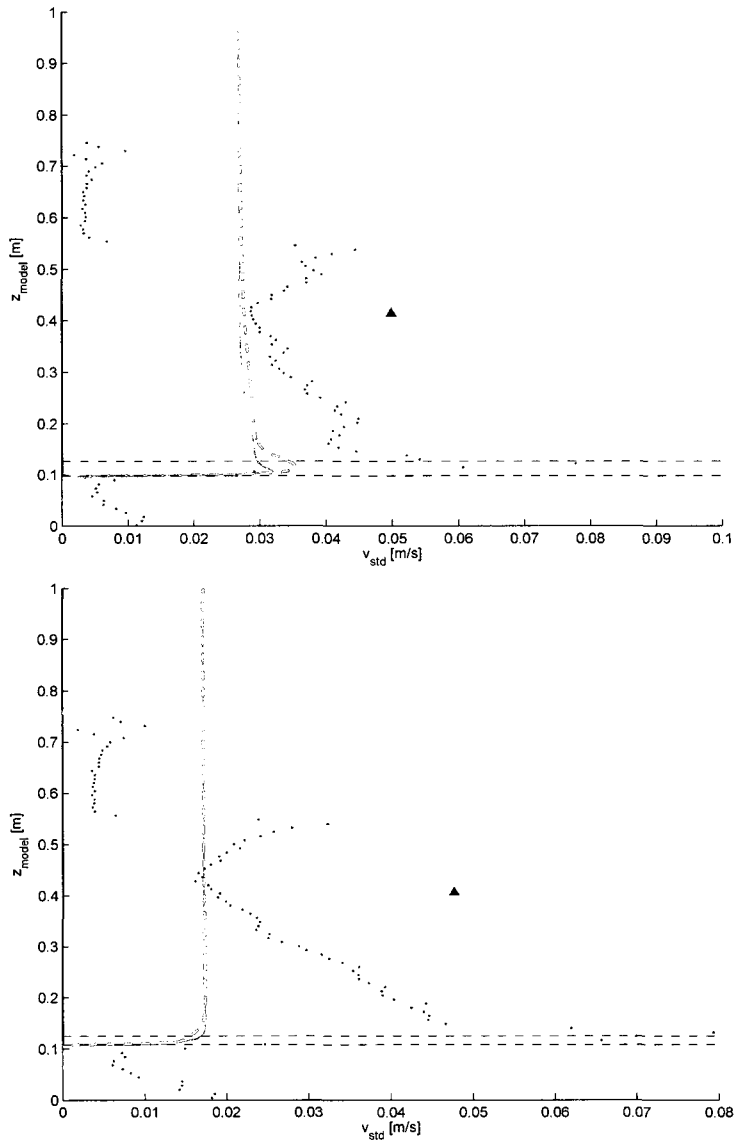

Figure 3-26: Case 3: v_{std} model-data comparison profiles for bursts 286 (top) and 289 (bottom). The triangle represents single point velocity measurements recorded by the ADV. The red dotted profile shows Doppler profiler observations. The black dashed line reveals the height above the vertical model datum at which the profiler sampling volume reaches the bed. The red dashed line shows the vertical position of the crest of the actual bedform recorded by the pencil beam sonar. The orange and green dashed lines represent Case 3 model simulations with sinusoidal waves, bichromatic wave groups, respectively. The solid blue line shows a sinusoidal wave simulation profile at $\alpha_w = 0$ (Case 1) for comparison.

profiles in the presence of currents. On the contrary, in instances of lesser current magnitudes and wave angles, negligible effects are evident. This suggests that

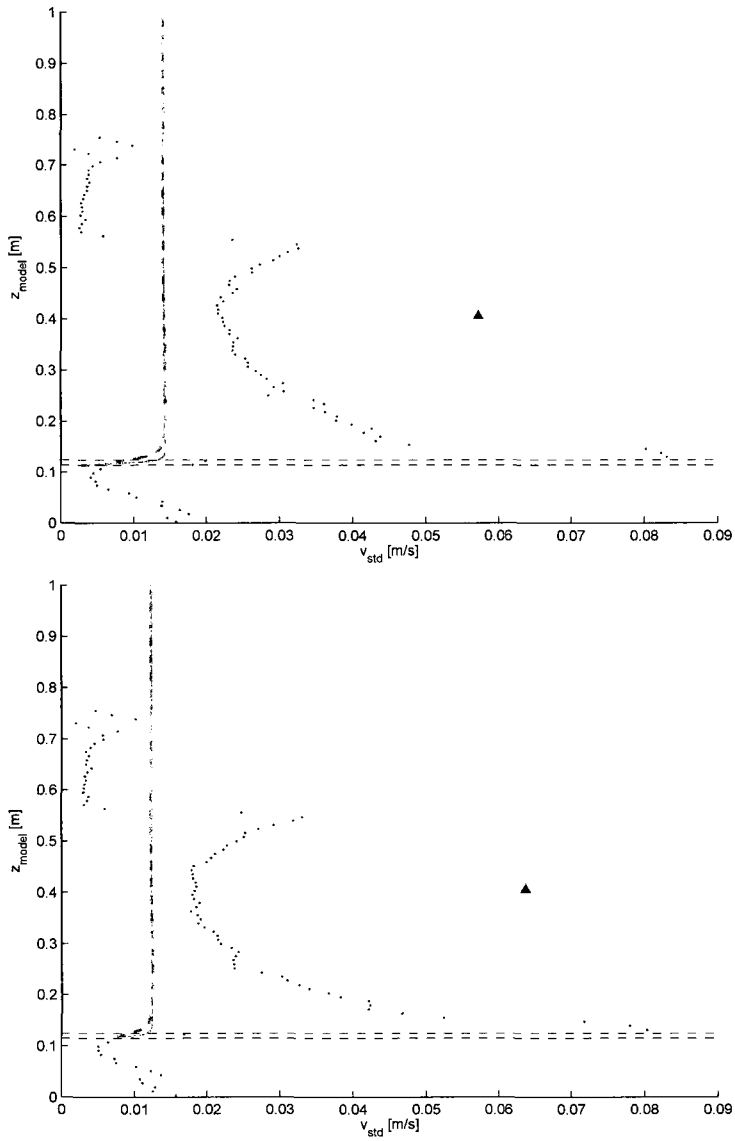

Figure 3-27: Case 3: v_{std} model-data comparison profiles for bursts 292 (top) and 294 (bottom). The triangle represents single point velocity measurements recorded by the ADV. The red dotted profile shows Doppler profiler observations. The black dashed line reveals the height above the vertical model datum at which the profiler sampling volume reaches the bed. The red dashed line shows the vertical position of the crest of the actual bedform recorded by the pencil beam sonar. The orange and green dashed lines represent Case 3 model simulations with sinusoidal waves, bichromatic wave groups, respectively. The solid blue line shows a sinusoidal wave simulation profile at $\alpha_w = 0$ (Case 1) for comparison.

the model is sensitive to combinations of wave and current forcing, however, the majority of the cases investigated here may have wave and current velocities that

are too small to notice much of an impact on the resulting v_{std} profiles.

3.7 Spatial Variability of Simulations Over a Characteristic Bedform

This section addresses the spatial variability of simulated velocity profiles. Figures 3-28 and 3-29 show cross shore and vertical velocity standard deviation vector fields at 15 equally spaced positions along the bedform for Case 1 real wave simulations. Vector directions show the relative contribution of horizontal and vertical velocities. Figures 3-28 and 3-29 show that standard deviation velocity vector profiles have low shear with elevation in the ripple trough, and not surprisingly, have considerably more shear near the ripple crest. Within one ripple height above the bedform crest, vectors remain nearly parallel to the local bedform slope. Note that on the right side of the ripple crest, this argument still holds true, however the sign of the magnitude changes as the local bedform slope is negative and standard deviation velocity, by definition, is always positive. Above one ripple height above the bedform crest, velocity profile vectors show decreasing bedform influence to the flow field with increasing distance from the bed. This is shown by the velocity vectors above $z_{model} = 0.25$ m having less of a vertical velocity component, with vectors approaching horizontal orientation. The five profiles nearest the crest show the most dramatic bedform influence on profiles. Rather than increasing monotonically to their free stream value, the profiles nearest the crest show a velocity overshoot nearest the bed, then decrease to their free stream value. This results

from flow acceleration over the ripple crest.

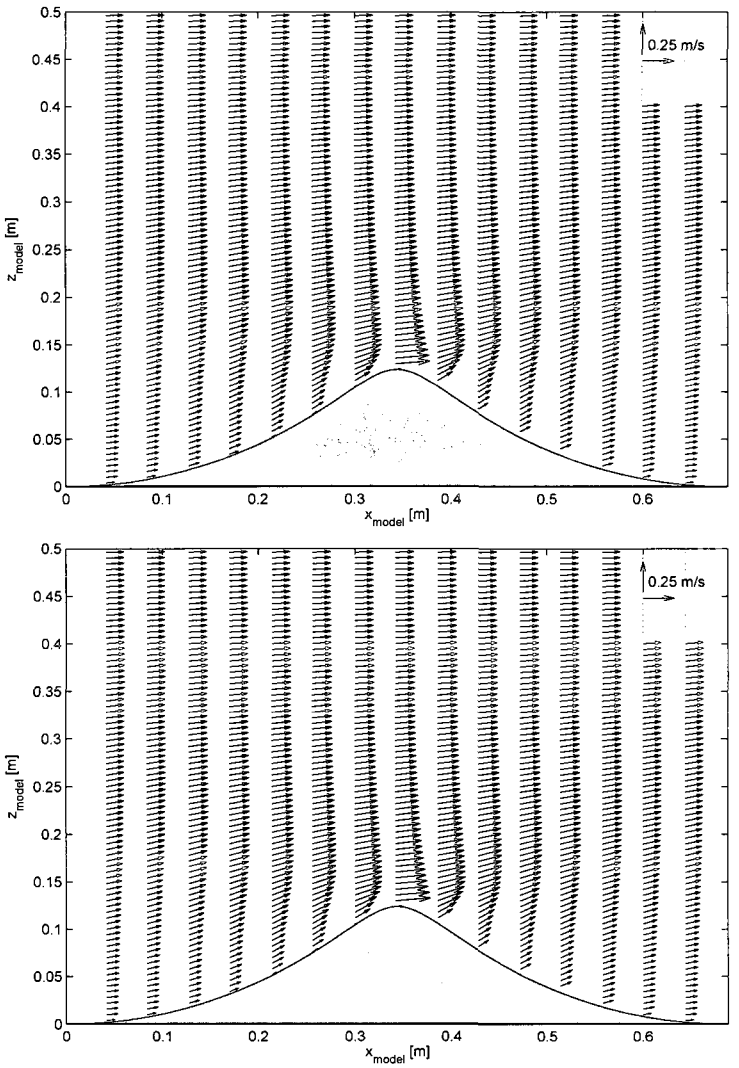

Figure 3-28: Standard deviation velocity vector fields for bursts 286 (top) and 289 (bottom) for Case 1 real wave forcing simulated over a Sleath ripple. The arrow direction and magnitude result from vector addition of u_{std} and w_{std} at arrow origin. A scale is given in upper right hand corner for reference

Figures 3-30 and 3-31 show spatial standard deviation of the vertical velocity temporal standard deviation profiles further demonstrating the velocity variability in the flow field in the presence of a bedform. The spatial variability of w_{std} increases consistently from $z_{model} = 0$ until achieving its maximum magnitude just below the

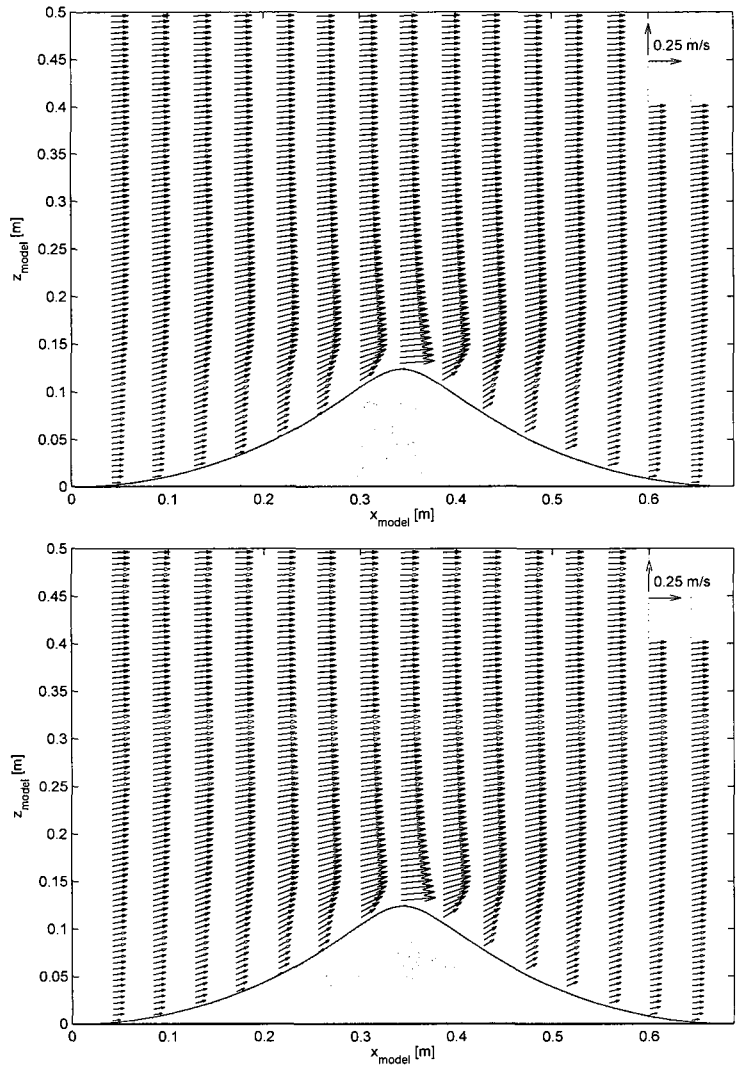

Figure 3-29: Standard deviation velocity vector fields for bursts 292 (top) and 294 (bottom) for Case 1 real wave forcing simulated over a Sleath ripple. The arrow direction and magnitude result from vector addition of u_{std} and w_{std} at arrow origin. A scale is given in upper right hand corner for reference

ripple crest. The amount of variability over the ripple is directly proportional to the width of the dark gray area in the figure. Spatial variability decreases consistently with distance from the bed at elevations greater than the ripple crest. Spatial position of the velocity profile can account for w_{std} velocity measurements of up to 6 cm/s difference. w_{std} spatial variability is consistent for each of the bursts

analyzed. The thick black line in Figures 3-30 and 3-31 show that the profiler was positioned on the ripple at a location of near maximum velocities over the bedform. This suggests that a slight miscalculation of position of the profiler would have significant impact on the simulated profile, and its agreement with the observations. The standard deviation profile variability decreased significantly above one ripple height above the crest, and showed little spatial variability at elevations greater than two ripple heights above the crest. This suggests that bedform induced form drag has implications on the flow field within two ripple heights above the ripple crest for the hydrodynamic forcing investigated.

Figures 3-32 and 3-33 show the spatial variability of u_{std} profiles for Case 1 real waves over a characteristic bedform. Variability is relatively consistent at all elevations below the ripple crest as demonstrated by the nearly constant width of the gray area below the black dashed line. u_{std} spatial variability is a maximum just above the crest location and decreases monotonically with distance above the bed. Significant spatial variability is observed in simulations up to elevations of $z_{model} = 0.3$ m, or nearly 2 ripple heights above the crest. Above this point, spatial variability is negligible with a deviation of around 1 cm/s. Similar to w_{std}, u_{std} shows largest variability near the crest elevation, and suggests that the profiler location is near the position of maximum velocity along the bedform.

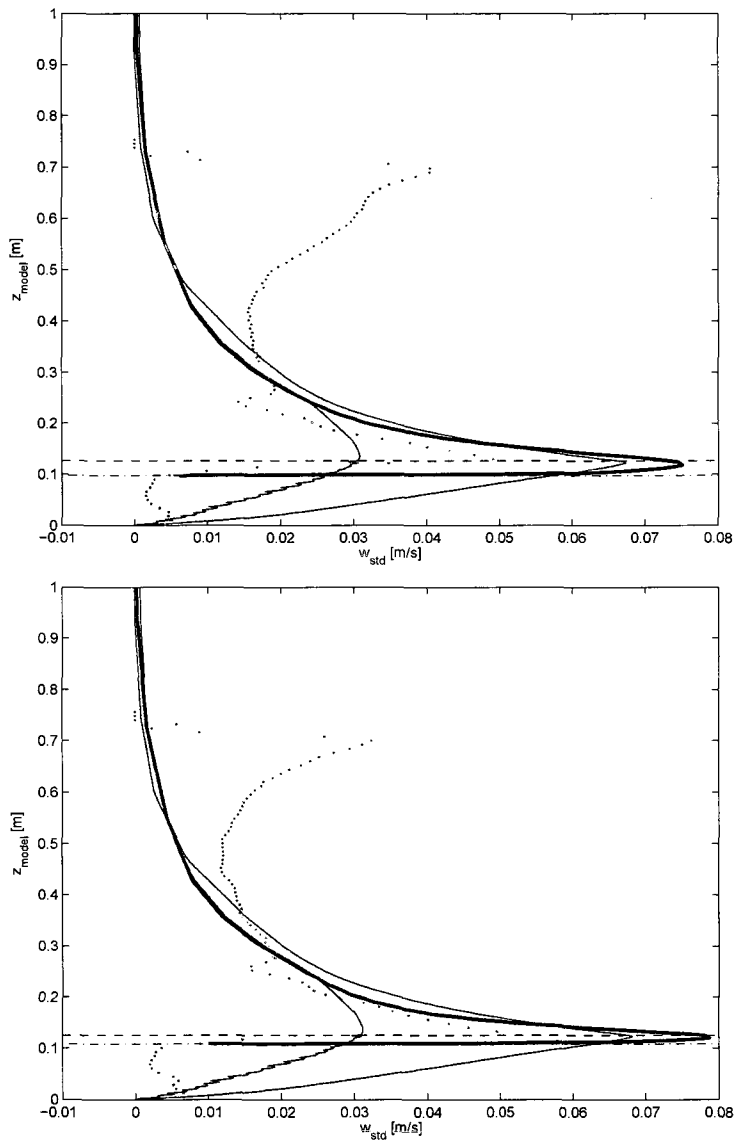

Figure 3-30: Spatial variability of w_{std} for bursts 286 (top) and 289 (bottom) for Case 1 real wave simulations. The red dots represent Doppler profiler data. The black line shows simulation profile at location of profiler. The light gray lines show w_{std} profiles along the bedform. The dark gray area is spatial mean of standard deviation profile for vertical velocity +/- 1 standard deviation about the mean.

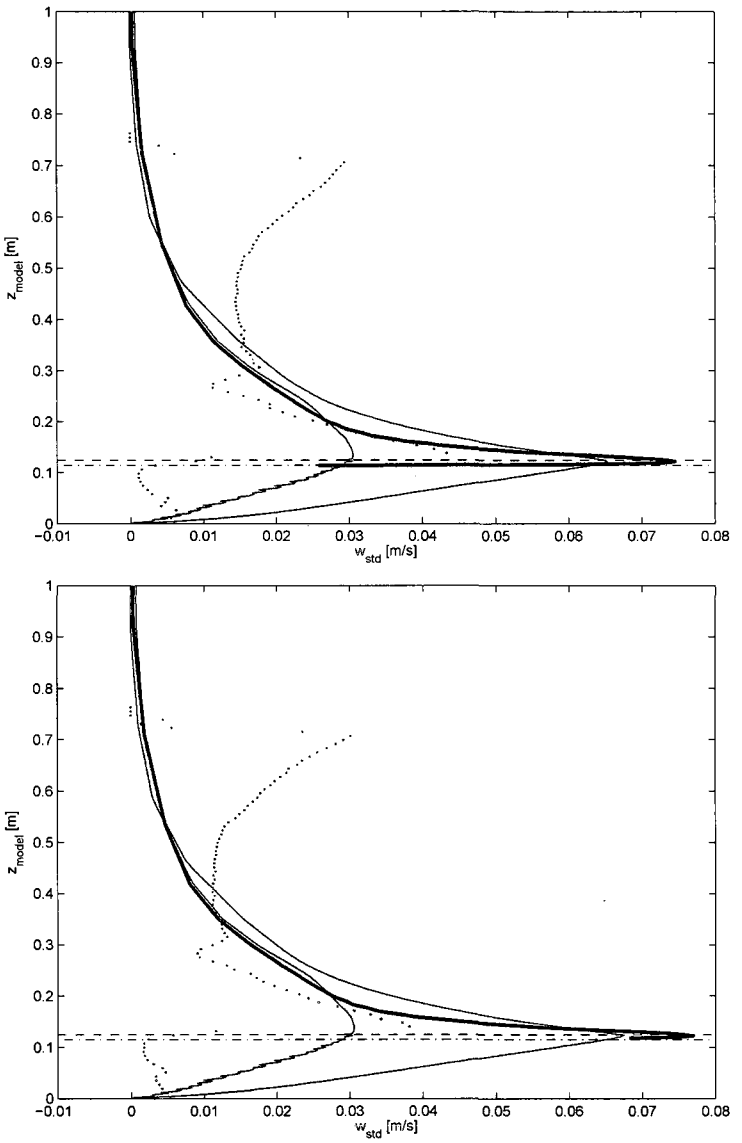

Figure 3-31: Spatial variability of w_{std} for bursts 292 (top) and 294 (bottom) for Case 1 real wave simulations. The red dots represent Doppler profiler data. The black line shows simulation profile at location of profiler. The light gray lines show w_{std} profiles along the bedform. The dark gray area is spatial mean of standard deviation profile for vertical velocity +/- 1 standard deviation about the mean.

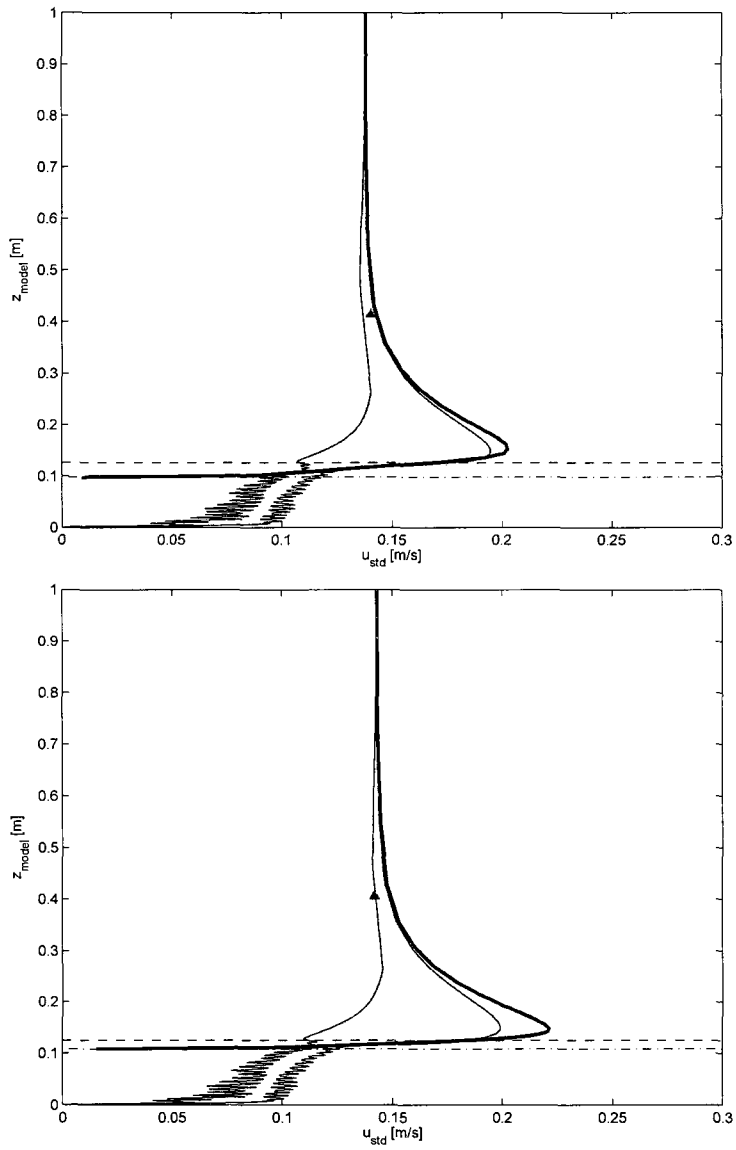

Figure 3-32: Spatial variability of u_{std} for bursts 286 (top) and 289 (bottom) for Case 1 real wave simulations. The red dots represent Doppler profiler data. The black line shows simulation profile at location of profiler. The light gray lines show u_{std} profiles along the bedform. The dark gray area is spatial mean of standard deviation profile for vertical velocity +/- 1 standard deviation about the mean. The ADV u_{std} velocity is shown by red triangle with black fill.

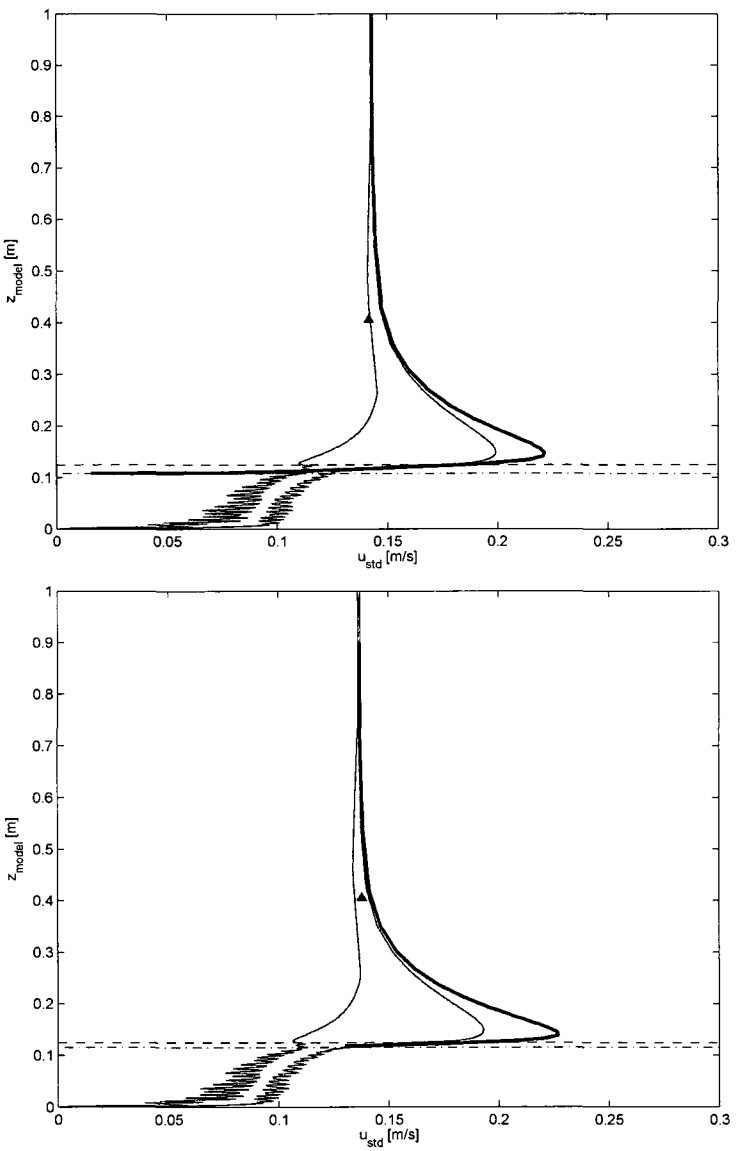

Figure 3-33: Spatial variability of u_{std} for bursts 292 (top) and 294 (bottom) for Case 1 real wave simulations. The red dots represent Doppler profiler data. The black line shows simulation profile at location of profiler. The light gray lines show u_{std} profiles along the bedform. The dark gray area is spatial mean of standard deviation profile for vertical velocity +/- 1 standard deviation about the mean. The ADV u_{std} velocity is shown by red triangle with black fill.

3.8 Spatial Variability of Simulations Over Observed Bedforms

Vector profiles of cross shore and vertical standard deviation velocities are shown at 15 locations for real waves simulated over observed bedforms for bursts 286 and 289 in Figure 3-34, and bursts 292 and 294 in Figure 3-35. Similar to simulations over a Sleath ripple, velocity profiles have little variation in ripple troughs, with profiles steadily increasing to their free stream value with distance from the bed for vectors shown. Near the bedform crest and locations of steep bedform gradients (often located to the right of the ripple crest for the bursts investigated), large variability and velocity overshoot is predicted. Vector profile trends for flow over observed bedforms are similar for those estimated by flow over characteristic bedforms.

Figures 3-36 and 3-37 show simulated spatial variability of w_{std} for real wave flow over observed bedforms. Similar to flow over characteristic bedforms, spatial variability increases steadily from 0 at $z_{model} = 0$ m to a maximum just below the ripple crest. Due to the more variable observed bedform shape, the predicted standard deviation profile of w_{std} shows higher variability than predicted for flow over a Sleath ripple. The profile at the Doppler profiler location (thick black line) suggests that the Doppler is not in one of the most dynamic spatial positions along the ripple, as suggest from simulated flow over the Sleath ripple. This is shown by the w_{std} profile positioned near the mean of the spatial standard deviation velocity profile, rather than outside the region within one standard deviation of the mean as

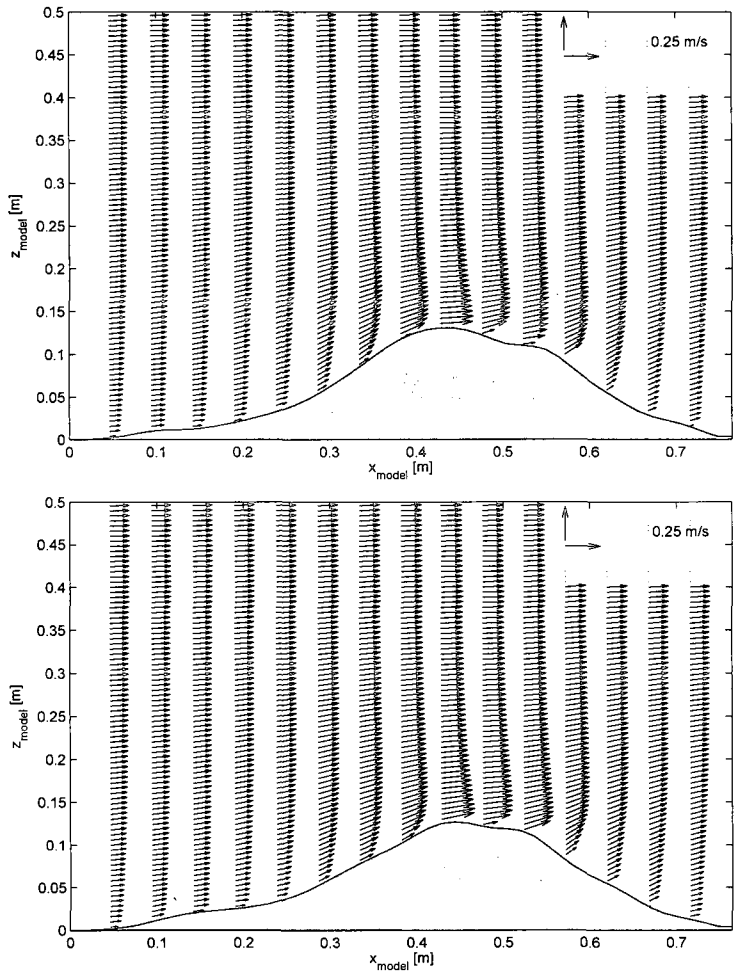

Figure 3-34: Standard deviation velocity profiles for bursts 286 (top) and 289 (bottom) for Case 1 real wave forcing simulated over observed bedforms. The arrow direction and magnitude result from vector addition of u_{std} and w_{std} at arrow origin. Scale in upper right hand corner for reference

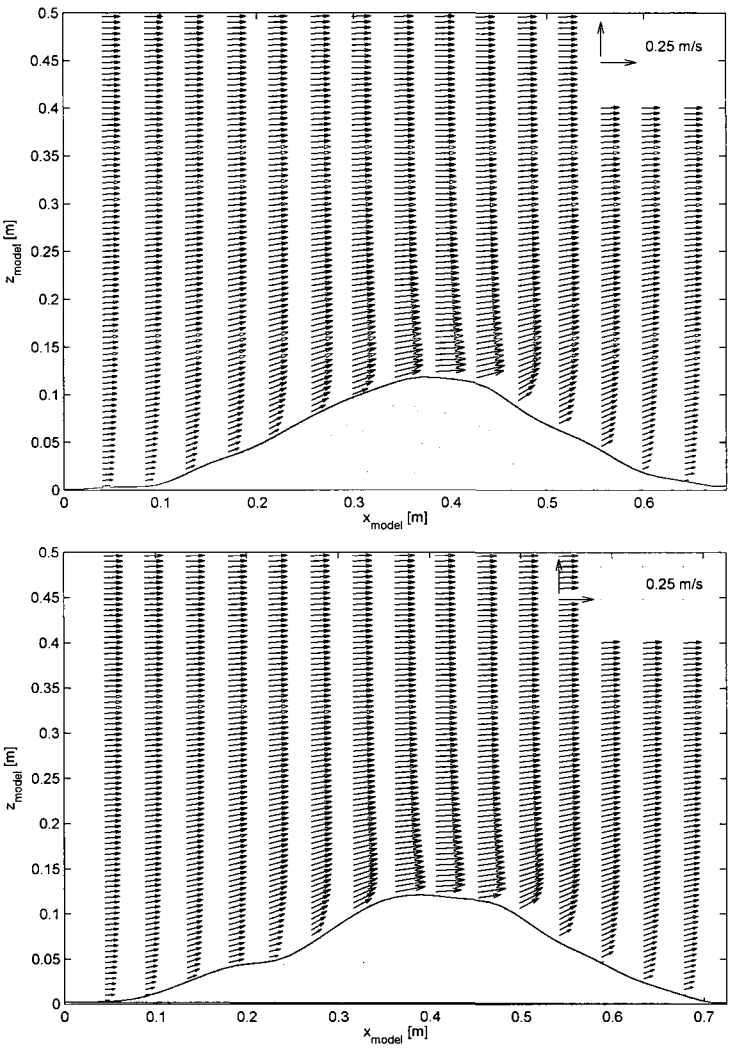

Figure 3-35: Standard deviation velocity profiles for bursts 292 (top) and 294 (bottom) for Case 1 real wave forcing simulated over observed bedforms. The arrow direction and magnitude result from vector addition of u_{std} and w_{std} at arrow origin. Scale in upper right hand corner for reference

flow over a Sleath ripple.

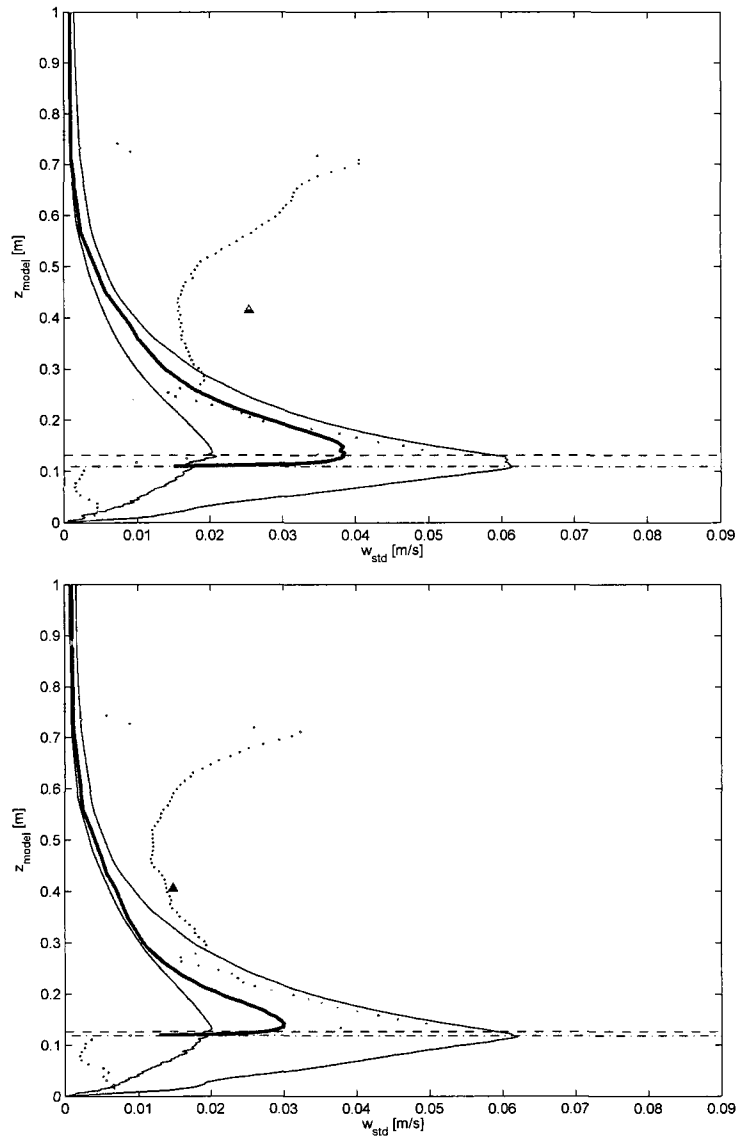

Figure 3-36: Spatial variability of w_{std} for bursts 286 (top) and 289 (bottom) for Case 1 real wave simulations over an observed bedform.. The red dots represent Doppler profiler data. The black line shows simulation profile at location of profiler. The light gray lines show w_{std} profiles along the bedform. The dark gray area is spatial mean of standard deviation profile for vertical velocity +/- 1 standard deviation about the mean. The ADV w_{std} velocity is shown by red triangle with black fill.

The spatial variability of u_{std} for real wave simulations over an observed bedform are shown for bursts 286 and 289 in Figure 3-38, and for bursts 292 and 294 in

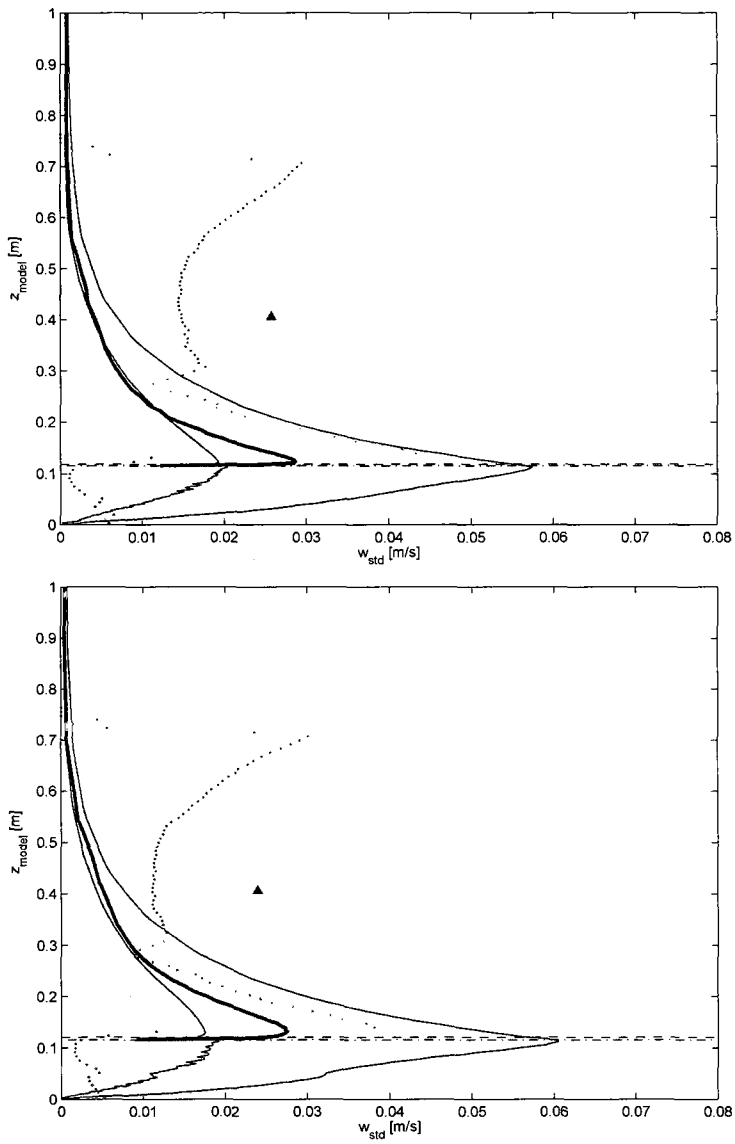

Figure 3-37: Spatial variability of w_{std} for bursts 292 (top) and 294 (bottom) for Case 1 real wave simulations over an observed bedform. The red dots represent Doppler profiler data. The black line shows simulation profile at location of profiler. The light gray lines show w_{std} profiles along the bedform. The dark gray area is spatial mean of standard deviation profile for vertical velocity +/- 1 standard deviation about the mean. The ADV w_{std} velocity is shown by red triangle with black fill.

Figure 3-39. The dark gray area shows one spatial standard deviation about the mean of u_{std} profiles. The width of the gray area at a given elevation is directly related to the amount of disturbance that the bedform exhibits on the flow field.

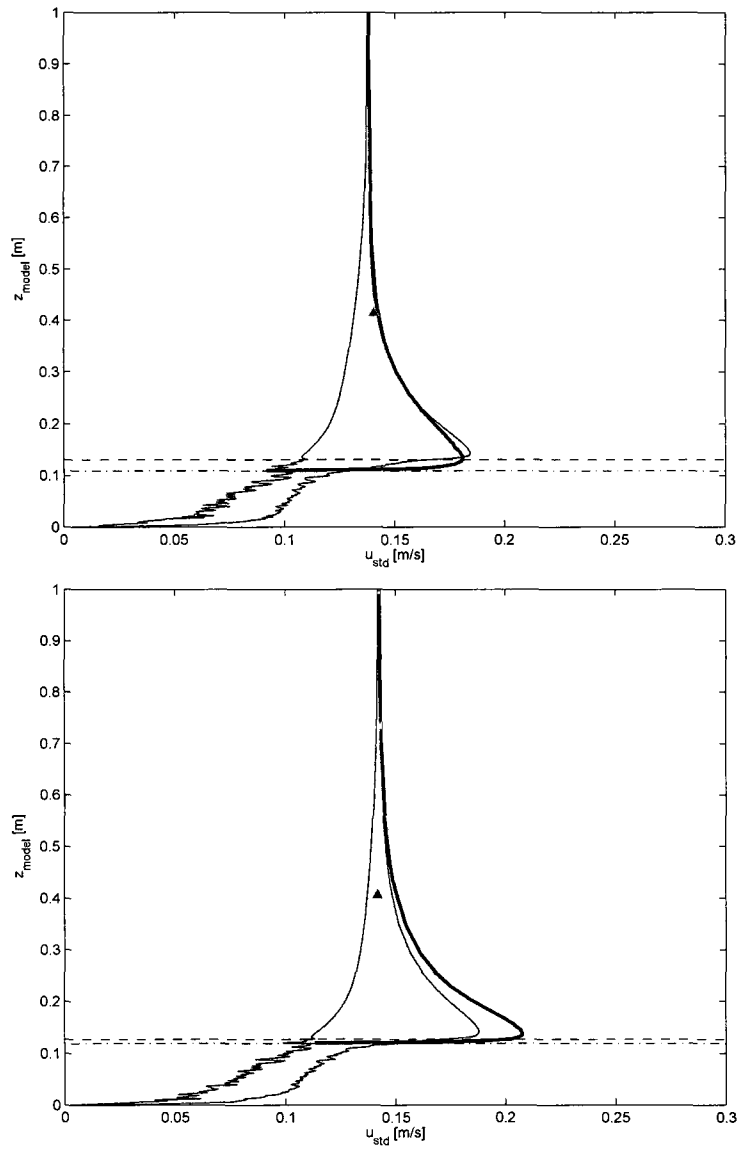

Figure 3-38: Spatial variability of u_{std} for bursts 286 (top) and 289 (bottom) for Case 1 real wave simulations over an observed bedform. The red dots represent Doppler profiler data. The black line shows simulation profile at location of profiler. The light gray lines show u_{std} profiles along the bedform. The dark gray area is spatial mean of standard deviation profile for vertical velocity +/- 1 standard deviation about the mean. The ADV u_{std} velocity is shown by red triangle with black fill.

Bedform disturbance has the greatest effect on u velocities just above the crest location. At heights greater than one ripple height above the ripple crest, spatial variability of u_{std} in the flow field decreases significantly with increasing distance

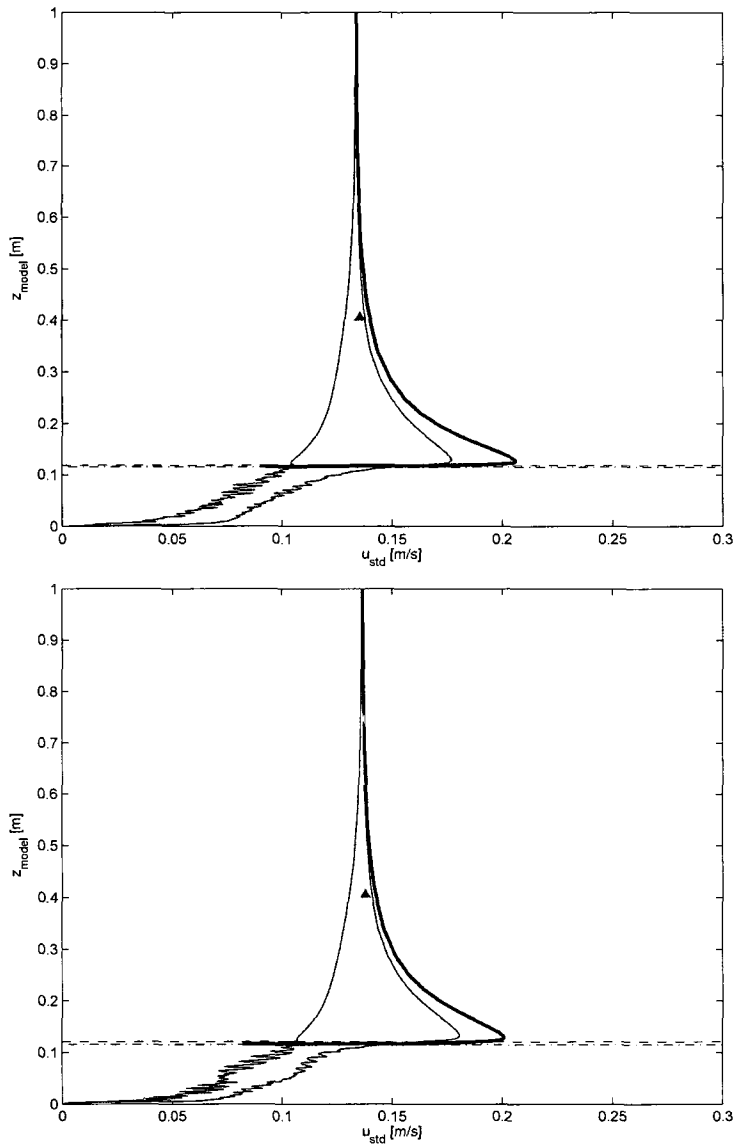

Figure 3-39: Spatial variability of u_{std} for bursts 292 (top) and 294 (bottom) for Case 1 real wave simulations over an observed bedform. The red dots represent Doppler profiler data. The black line shows simulation profile at location of profiler. The light gray lines show u_{std} profiles along the bedform. The dark gray area is spatial mean of standard deviation profile for vertical velocity +/- 1 standard deviation about the mean. The ADV u_{std} velocity is shown by red triangle with black fill.

from the bed. At an elevation of 0.5 meters, the bedform has little effect on the flow field characteristics. Observed bedforms have slightly greater effects on the flow field than Sleath bedforms at elevations in the range 0.2 m $< z_{model} <$ 0.5 m.

Below 0.2 m, spatial variability in u_{std} is greater for the Sleath ripple. The overall shape and trends of spatial standard deviation of u_{std} over an observed bedform are consistent with equivalent flows over the characteristic Sleath ripple (see Figures 3-32 and 3-33). This suggests that although individual bedform characteristics can vary significantly, the characteristic Sleath ripple may provide an adequate approximation of the ripple characteristics observed in this investigation.

3.8.1 Summary

Figure 3-40 shows an overview of the simulations executed for Cases 1, 2, and 3. Sinusoidal simulations are compared with all bursts in the record, while real data and bichromatic wave groups are only compared with the records analyzed in depth in this investigation. The lower values of root-mean-square deviation (herein RMS_d) for wave groups and real wave time series simulations reveal that these simulations are able to better predict the observed data. This is also made evident by the profiles inspection of the profiles in Figure 3-40 d. The dynamics associated with lower frequency signal in the flow field are crucial to estimating the characteristics of flow in the bottom boundary layer. The previous section showcased the spatial variability of velocity profiles. It is important to note that the model-data comparisons presented in this investigation are for a single location on the ripple crest. Each of the profiles investigated were located in the highly dynamic near crest region. Simulations often over predicted near bed estimates of shear at this location. However, generalizations for this investigation must be made with caution as flow over only a small portion of the ripple were analyzed.

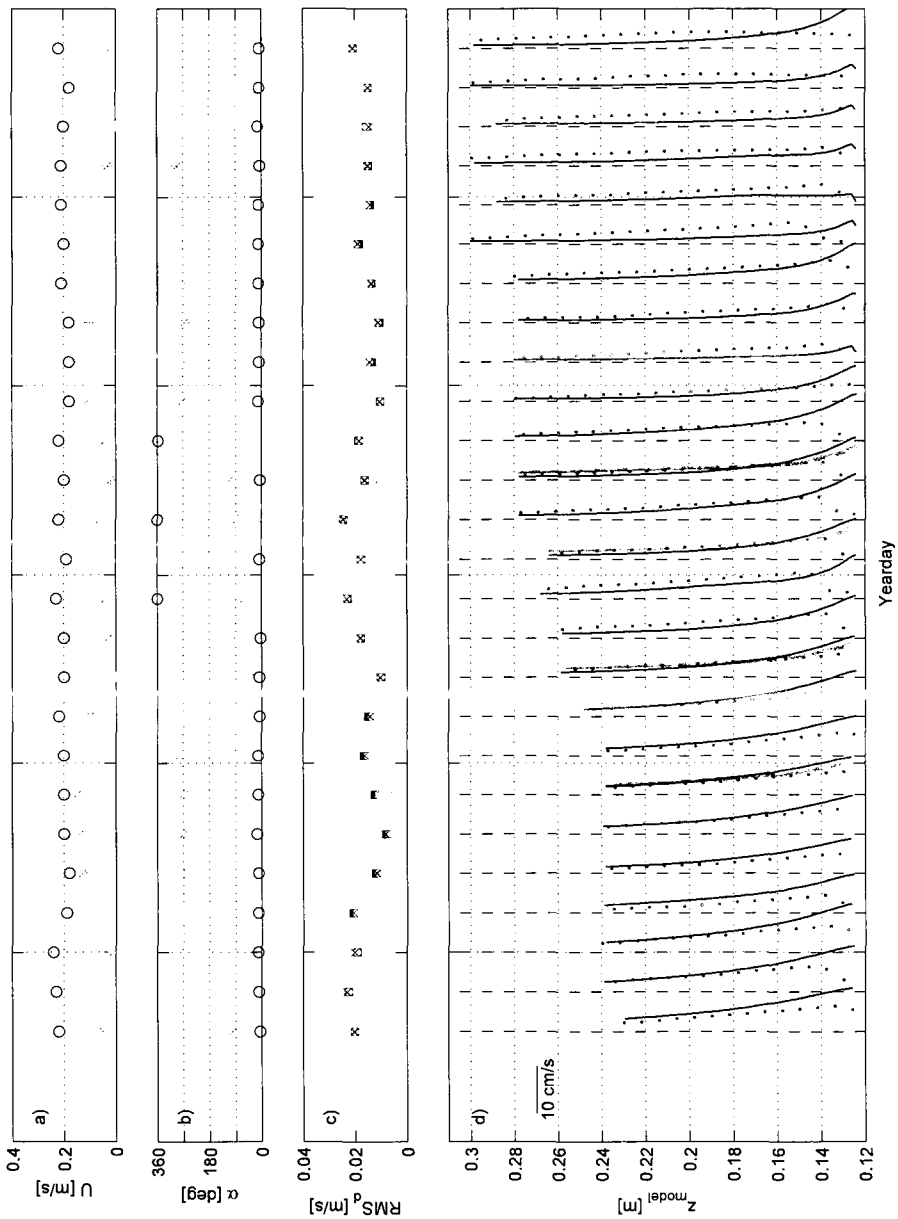

Figure 3-40: w_{std} comparison summary over the entire data set. The circles and stars in panel a) show wave and current velocity magnitudes, respectively. Panel b) circles and stars show α_w and α_c, respectively. Panel c) shows root mean square difference (RMS_d) between model and simulation data. Black squares, light blue circles, and dark blue x's show RMS_d values for sinusoidal wave simulations for Cases 1, 2, and 3, respectively. Gray stars show show RMS_d for Case 1 real wave data, and green diamonds for Case 3 bichromatic wave group simulations. Panel d) shows w_{std} profiles for Doppler profiler data as red dots, Case 1 real waves as gray line, and Case 3 bichromatic waves simulations as green dashed line. A scale bar of 10 cm/s is provided on in the upper left portion of panel d) for reference.

CHAPTER 4

CONCLUSIONS

Model simulations of bottom boundary layer flow over bedforms have been performed with a quasi-three-dimensional bottom boundary layer model, **Dune**, over a range of bedforms with flows of varied complexity. Simulations were evaluated by comparing standard deviation profiles of vertical velocity with field observations measured by a Doppler profiler instrument and ADV point measurements. Simulated hydrodynamic forcing conditions included sinusoidal waves and bichromatic wave groups with and without mean currents, as well as observed velocities obliquely approaching at various angles in the absence of currents.

All simulations over-predicted flow variance in the extreme near-bed region at the location of the profiler instrument, with largest estimates resulting from sinusoidal wave simulations. Observations show lower near bed amplitudes possibly due to bottom reflections or profiler bin locations. The model likely over-estimates the velocity near the crest due to large shear and additional accelerations required to satisfy the no slip condition. While there is no significant sediment suspension, the bed migration of 0.5 cm/s suggests that the incipient motion criterion is, at least, exceeded on occasion. Sinusoidal wave simulations consistently under-predicted the flow dynamics at elevations above the ripple crest. Simulations with modulating velocity magnitudes (namely bichromatic wave groups and real wave time series)

showed an expanded boundary layer with higher shear away from the bed than sinusoidal wave cases. Simulations with modulating velocity magnitudes were able to better predict the shape and magnitude of observed velocity profiles at the instrument location for the records analyzed. Real wave simulations provided the closest agreement with field observations for the investigated profiler locations, which is consistent with the lower values of root-mean-squared deviation for real wave simulations. Real waves simulated over observed bedforms consistently under-predicted observations of w_{std} at the instrument location. Conversely, real waves over the representative Sleath ripple tended to over-predict w_{std} profiles at the ripple location.

The presence of currents had a negligible effect on real wave simulations, as the wave bottom boundary layer was too small to show significant interactions with the current. On the other hand, the introduction of mean currents on bichromatic wave simulations significantly expanded boundary layer, and introduced greater shear at elevations greater than one ripple height above the bedform crest. The model is insensitive to slight wave angles of less than 10 degrees.

Simulations showed significant spatial variability over the bedform, with highest variability located in the vicinity of the ripple crest. Standard deviation profile variability decreased significantly above one ripple height above the crest, and showed little spatial variability at elevations greater than two ripple heights above the crest. This suggests that bedform induced form drag has implications on the flow field within two ripple heights above the ripple crest for the hydrodynamic forcing investigated.

Real wave simulations over observed bedforms - the simulations that most closely represent observed conditions - compared less favorably with observed w_{std} profiles than simulations over the representative Sleath ripple. Often, simulations real waves over observed bed simulations under-predicted the magnitude of standard deviation velocity at the location of the profiler instrument. Further investigation of the dynamics of simulated flow over observed ripples is required to assess less favorable agreement for these simulations.

APPENDICIES

APPENDIX A

REVIEW OF REYNOLDS-AVERAGED NAVIER-STOKES EQUATIONS

In order to attain a numerical solution to the governing equations, the non-linear mathematical complexities of turbulence and flow-sediment coupling needed to be resolved. The construction of the model began with the conservation of momentum equations for a Newtonian fluid element, known as the Navier-Stokes equations (*Kundu and Cohen*, 2008). To decrease the complexity and computational expense of the modeling effort, the flow was assumed to be two-dimensional (herein 2-D), thus, all flow and sediment structures are assumed uniform in the plane perpendicular to the flow (*Tjerry*, 1995). The main difficulties of solving Navier-Stokes equations in three dimensions are not present in two dimensions, and existence and smoothness of the solutions in two dimensions is known to exist (*Ladyzhenskaya*, 1969). The purpose of this model is to simulate flows and sediment structure interactions in a riverine environment for engineering purposes, and thus, the 2-D flow assumption is considered acceptable. Additionally, the fluid was assumed to be incompressible; thus, the density, ρ, was considered constant. Furthermore, the fluid was assumed to have constant viscosity in space and time.

The governing equations that describe the flow field are the Navier-Stokes Equations in the horizontal and vertical directions, as well as the conservation of mass.

This provides three equations, to solve for three unknowns: horizontal and vertical component of velocity, and pressure (p). All aforementioned variables are a function of space and time. The governing equations in cartesian coordinates and indicial notation are as follows:

$$\frac{\partial u_i}{\partial t} + u_j \frac{\partial u_i}{\partial x_j} = -\frac{1}{\rho}\frac{\partial p}{\partial x_i} + \nu \frac{\partial^2 u_i}{\partial x_j^2} \tag{A.1}$$

$$\frac{\partial u_i}{\partial x_i} = 0 \tag{A.2}$$

where ν is the kinematic viscosity. In the case of this model, the flow field is dependent on only roughness and bedform shape and dimensions.

Although the two-dimensional Navier-Stokes equations are proven to be solvable, they still involve high computational demand. To simulate flow directly, it is necessary to include all turbulence – from the Kolmogorov to the integral scale– as it all contributes to the flow field. However, when used for engineering applications, such as the model discussed here, direct simulation of the flow field is often unnecessary.

To decrease computation time, while still achieving sufficient results for the applications desired, flow characteristics are time averaged. Although this greatly reduces the exactness of the flow simulation, time averaged characteristics are often adequate to calculate events such as sediment transport (*Tjerry*, 1995). In order to determine time averaged turbulent characteristics, velocity must be decomposed into mean and fluctuating parts. This is known as Reynolds decomposition, yielding the new equation:

$$u_i = \overline{u_i} + u_i' \tag{A.3}$$

$$\overline{u_i'} = 0 \tag{A.4}$$

where, u_i = total velocity, $\overline{u_i}$ = mean velocity, u_i' = fluctuating velocity component. The over bar represents a time averaged variable. Time averaging is defined by:

$$\overline{\Psi} = \frac{1}{T}\int_t^{t+T} \Psi dt \tag{A.5}$$

where Ψ is an arbitrary variable. The total velocity cannot be time averaged directly without losing information about the turbulent component. The decomposed velocity variables are substituted into the governing equations before any averaging takes place. Substituting the decomposed velocity equation back into the Navier-Stokes equation yields the Reynolds Averaged Navier-Stokes (RANS) equations:

$$\frac{\partial \overline{u_i}}{\partial t} + \frac{\partial \overline{u_i u_j}}{\partial x_j} = -\frac{1}{\rho}\frac{\partial \overline{p}}{\partial x_j} + \nu \frac{\partial^2 u_i}{\partial x_j^2} + \frac{\partial \overline{u_i' u_j'}}{\partial x_j^2} \tag{A.6}$$

$$\frac{\partial \overline{u_i}}{\partial x_i} = 0 \tag{A.7}$$

The Navier-Stokes equations differ from the RANS equations by the time averaged fluctuating terms, which arise from the non-linear convective terms known as the

Reynolds stresses (*Tjerry*, 1995).

Although the RANS equations are exact (in the two dimensional sense), the decomposition of velocity into mean and fluctuating components introduces additional variables in the absence of supplemental governing equations. Consequently Reynolds-Averaging yields a system of unsolvable equations, an issue commonly referred to as the closure problem of turbulence. Actual turbulence is needed in order to solve the averaged equations directly, however, determination of exact turbulence is not possible. Hence, turbulence must be estimated through modeling.

Determination of the Reynolds stresses requires direct simulation of turbulence. The stresses cannot be ignored because they are largely responsible for transport phenomena and altering flow patterns. Therefore, turbulence modeling must be done to obtain these stresses. It is inherent that the turbulence be resolved as a function of only known values so that the same problem of having too many variables is avoided.

APPENDIX B

MATLAB^{TM} CODE

B.1 Sleath ripple generation

```
function [xb zb] = make_bf_sleath(lambdab, etab, xgrids)
% CREATE Sleath ripple
% Inputs ========
% lambdab : ripple wavelength
% etab : ripple height
% xgrids : number of horizontal grid cells = length(xb) - 1
%
% Outputs ========
% xb : horizontal position of bed % zb : vertical position of bed % % code modified
from code ripples.f lines 199 to 228 in Dune code (see % code below: lines 52 - 81)
% INPUTS ================
if exist('lambdab','var') == 0
    lambdab = 2.23; % Smyth and Hay (2002,2003) bedform wavelength (default)
end
if exist('etab','var') == 0
    etab = 0.3223; % Smyth and Hay (2002,2003) bedform height (default)
```

```
end
if exist('xgrids','var') == 0
    xgrids = 68; % xgrids = N = # x-grid cells = length(xb) - 1 (default)
end
% ============================
% Steepness = etab/lambdab; % ripple steepness
% deltalambda = lambdab/xgrids;
% Phi = atan(4*etab/lambdab); % tan(Phi) = 4*HD/LD in Fredsoes formulation
of model
kk = 2.0*pi/lambdab; % "wave number" of the ripple
xb = NaN*ones(xgrids,1); % initialize profile vectors xb and zb
zb = NaN*ones(xgrids,1);
for ii = 1:xgrids
    xi = ii/xgrids*lambdab + 0.5*lambdab;
    xb(ii,1) = xi - 0.5*etab*sin(kk*xi) - 0.5*lambdab;
    zb(ii,1) = 0.5*etab*cos(kk*xi) + 0.5*etab;
end
xb = cat(1,xb(xgrids) - lambdab,xb);
zb = cat(1,zb(xgrids),zb);
% plot sleath ripple
figure;
plot(xb,zb)
axis equal
```

```
ylim([0 etab*1.5])

xlim([0 max(xb)])

title('Sleath Ripple (axis equal)')

xlabel('xb [m]')

ylabel('zb [m]')

text(0.75, 0.75, ['lambda_b = ', num2str(lambdab)],'units','normalized')

text(0.75, 0.60, ['eta_b = ', num2str(etab)],'units','normalized')
```

APPENDIX C

MEAN VELOCITY PROFILE COMPARISONS

Mean velocity profiles for Cases 1, 2, and 3 are presented in this section. Mean velocities were not analyzed in this investigation because there was no way to validate model simulations.

C.1 Case 1 mean velocity profiles

Profiles of mean vertical velocities (w_{mean}) are presented in Figures C-1, and C-2. Similar to w_{std}, w_{mean} profiles show maximum values located between the bed intersect of the profile, and the ripple crest. Maximum values are never greater than 6 cm/s. For sinusoidal wave simulations, profiles decrease consistently to a value of zero as distance above the bedform is increased. On the contrary, both bichromatic wave group simulations, as well as simulated wave time series profiles reveal a region approximately 2 cm in height with nearly constant w_{mean} velocity, located just above the height of the crest. As distance above the crest increases, the w_{mean} velocity decreases to zero for bichromatic and real wave simulations. Magnitudes for w_{mean} are greatest for bichromatic wave group simulations throughout the entire vertical profile, whereas magnitudes for sinusoidal waves are the smallest.

Doppler profiler mean vertical velocity profiles are generally zero in the trusted region near the bed, with no definite structure or pattern. Similarly, no general-

izations may be made about mean vertical ADV velocities. Values for each record vary between +/- 1 cm/s, most often less than zero. This may be due to the acoustic Doppler nature of the instrument, which tends to bias vertical velocity measurements by the particle settling velocity.

Temporally averaged horizontal crest-normal velocity (u_{mean}) profiles are shown in Figures C-3 and C-4. Profiles show a rather large negative spike between the bed intersection and the crest location, in the immediate vicinity of the bed. This holds true for all simulated u_{mean} profiles. This is most likely due to a coherent vortex structure formed by the oscillatory flow over the ripple crest. Magnitudes of this negative spike reach values of 8 cm/s and the different records consistently show that wave groups produce the largest peak magnitudes. Real waves produce the second largest magnitudes of near bed negative maxima, whereas sinusoidal waves produce the smallest magnitude of the three crest-normal wave only simulations.

As distance from the bed is increased, u_{mean} velocity increases rapidly to values near zero. Sinusoidal waves show little or no overshoot in the mean as is recognized consistently in the wave group simulations. Both wave groups and sinusoidal simulations converge to a u_{mean} value of zero in the free stream. Real wave simulations are relatively inconsistent, often showing an overshoot in velocity profile, but rarely converging to $u_{mean} = 0$ as distance above the bed increases. This could be due to an error in completely removing the mean from the wave signal input into the model simulations.

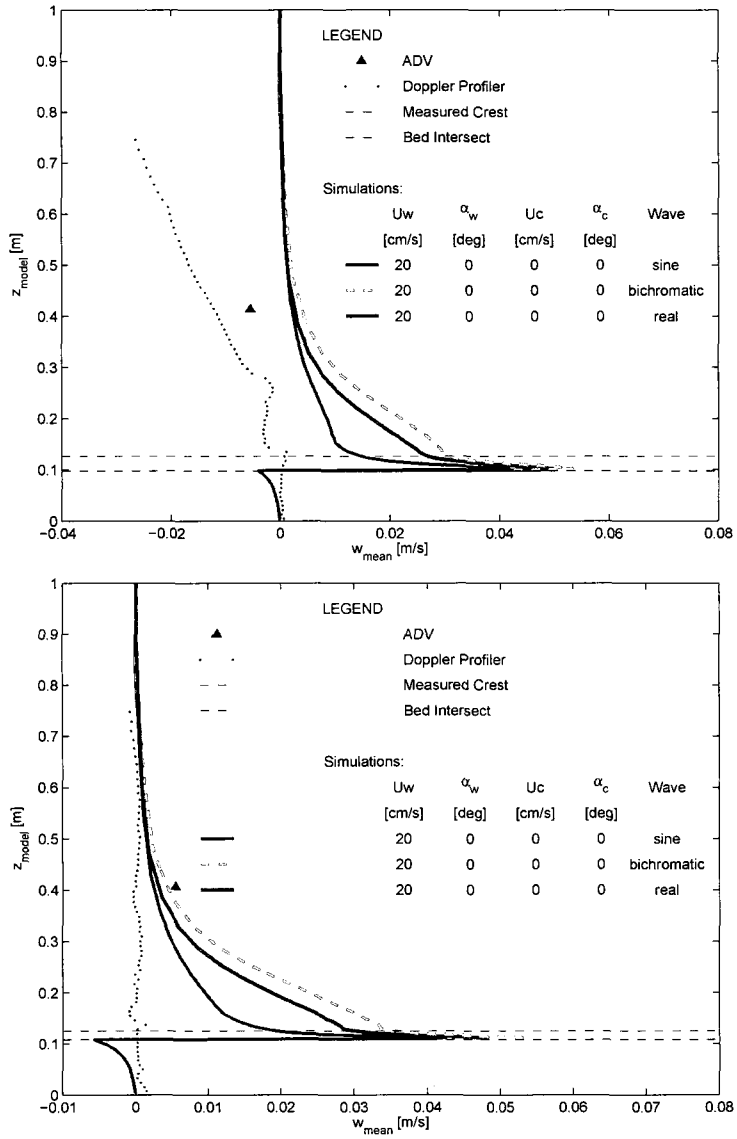

Figure C-1: Case 1: w_{mean} model-data comparison profiles for burst 286 (top) and 289 (bottom). The triangle represents single point velocity measurements recorded by the ADV. The red dotted profile shows Doppler profiler observations. The black dashed line reveals the height above the vertical model datum at which the profiler sampling volume reaches the bed. The red dashed line shows the vertical position of the crest of the actual bedform recorded by the pencil beam sonar. The blue, green-dashed, and gray lines represent model simulations with sinusoidal waves, bichromatic wave groups, and real wave data, respectively.

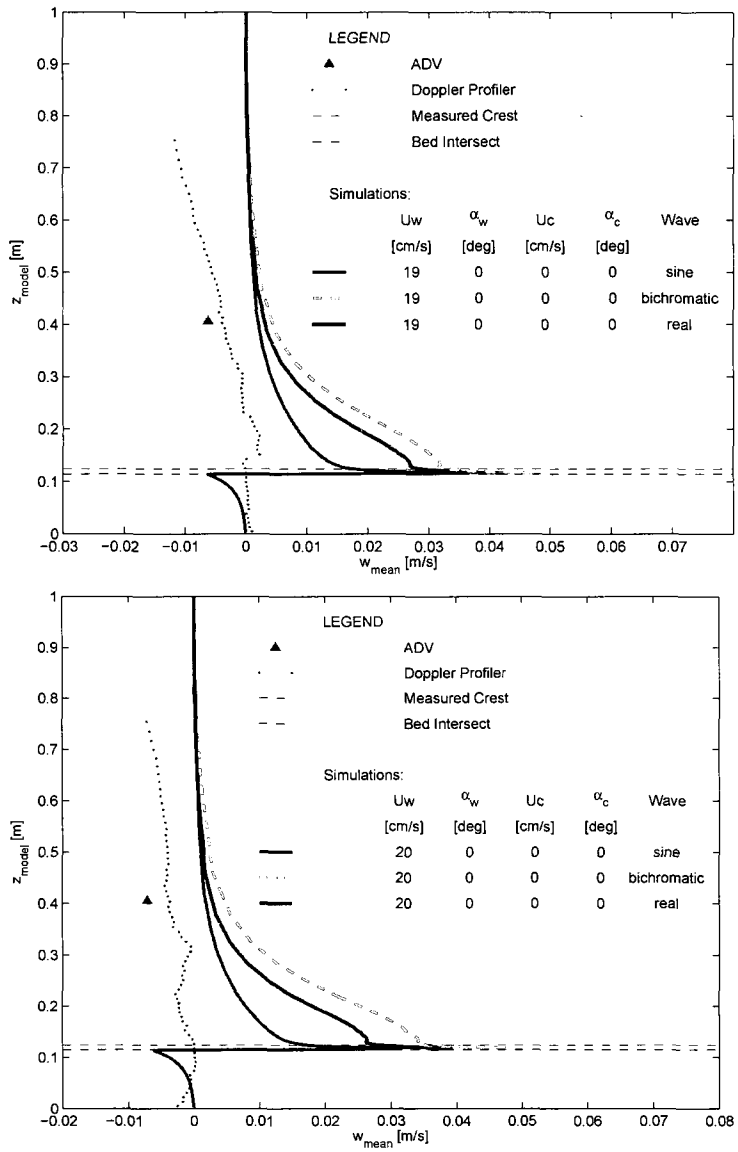

Figure C-2: Case 1: w_{mean} model-data comparison profiles for burst 292 (top) and 294 (bottom). The triangle represents single point velocity measurements recorded by the ADV. The red dotted profile shows Doppler profiler observations. The black dashed line reveals the height above the vertical model datum at which the profiler sampling volume reaches the bed. The red dashed line shows the vertical position of the crest of the actual bedform recorded by the pencil beam sonar. The blue, green-dashed, and gray lines represent model simulations with sinusoidal waves, bichromatic wave groups, and real wave data, respectively.

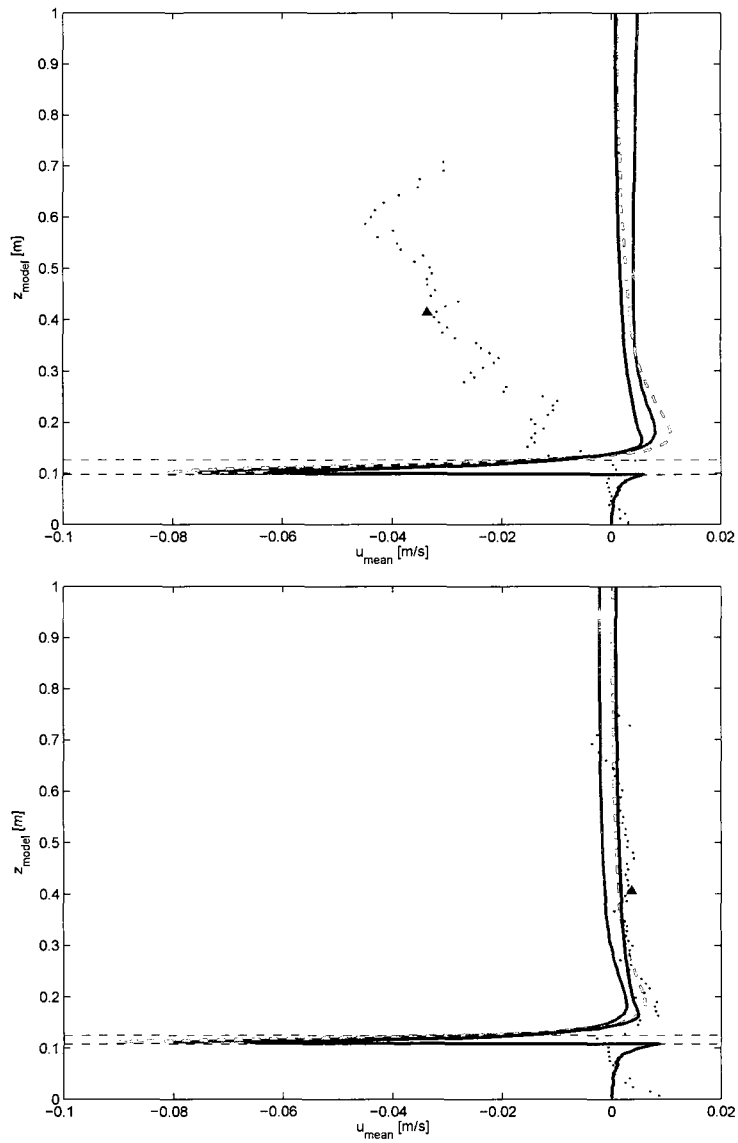

Figure C-3: Case 1: u_{mean} model-data comparison profiles for burst 286 (top) and 289 (bottom). The triangle represents single point velocity measurements recorded by the ADV. The red dotted profile shows Doppler profiler observations. The black dashed line reveals the height above the vertical model datum at which the profiler sampling volume reaches the bed. The red dashed line shows the vertical position of the crest of the actual bedform recorded by the pencil beam sonar. The blue, green-dashed, and gray lines represent model simulations with sinusoidal waves, bichromatic wave groups, and real wave data, respectively.

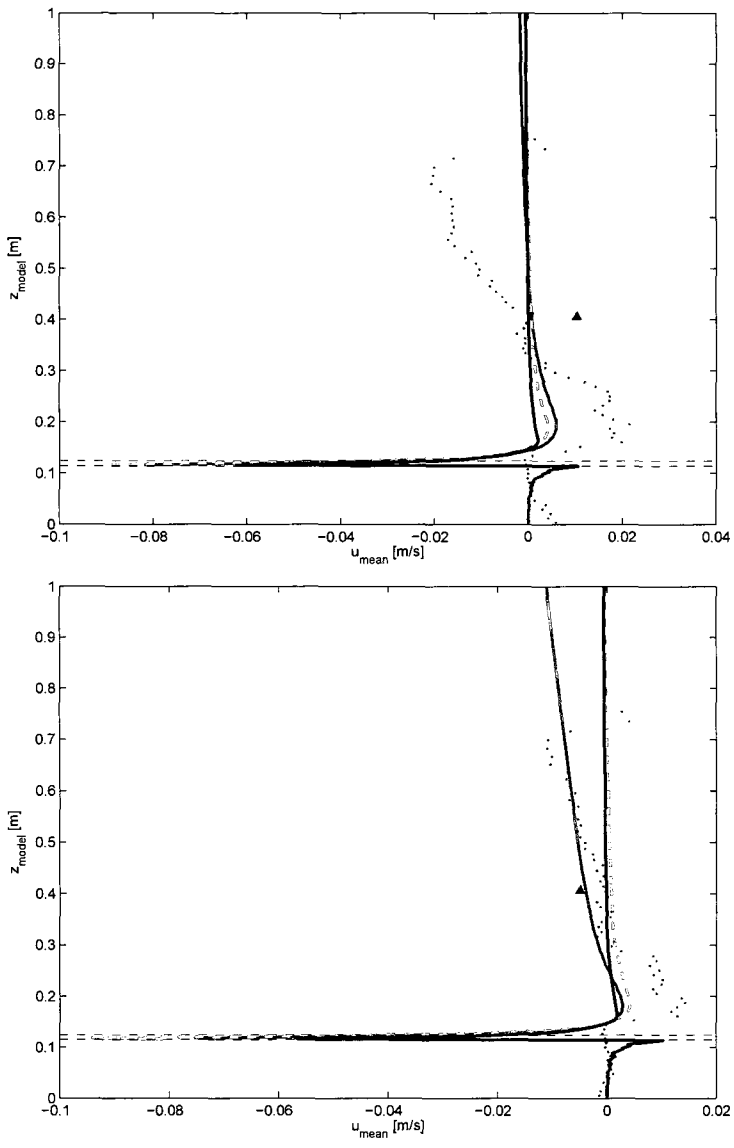

Figure C-4: Case 1: u_{mean} model-data comparison profiles for burst 292 (top) and 294 (bottom). The triangle represents single point velocity measurements recorded by the ADV. The red dotted profile shows Doppler profiler observations. The black dashed line reveals the height above the vertical model datum at which the profiler sampling volume reaches the bed. The red dashed line shows the vertical position of the crest of the actual bedform recorded by the pencil beam sonar. The blue, green-dashed, and gray lines represent model simulations with sinusoidal waves, bichromatic wave groups, and real wave data, respectively.

C.2 Case 2 mean velocity profiles

Mean velocity profiles for u, v, and w are presented in this section.

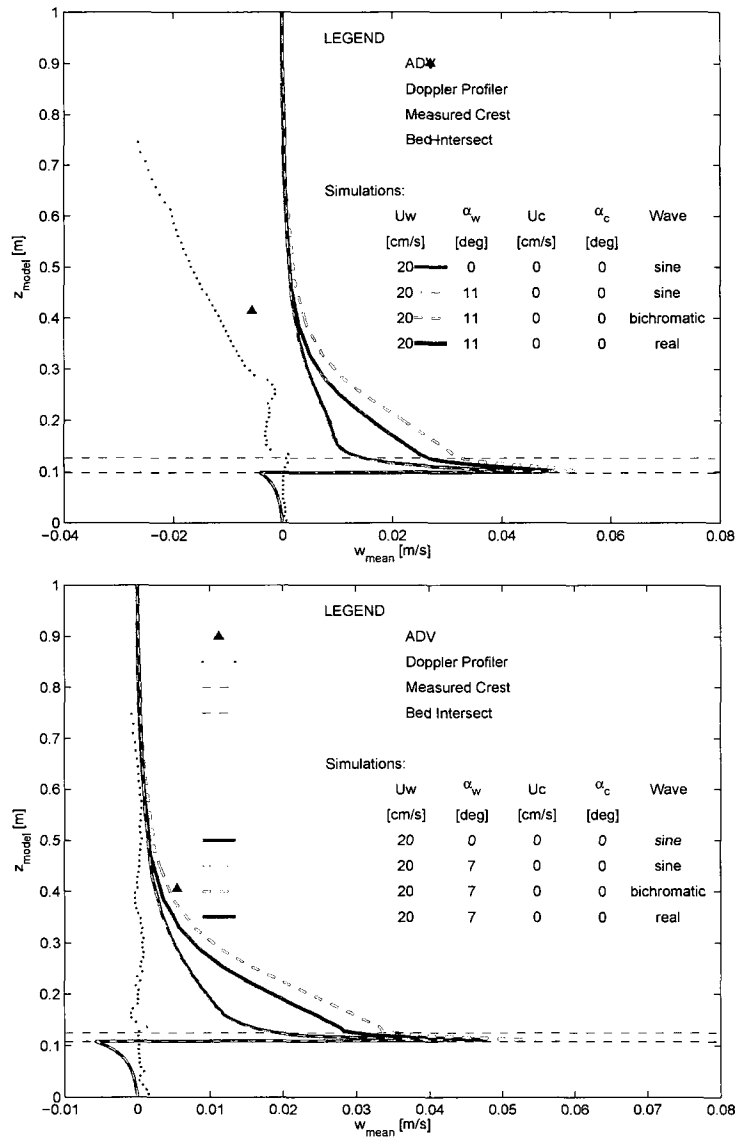

Figure C-5: Case 2: w_{mean} model-data comparison profiles for bursts 286 (top) and 289 (bottom). The triangle represents single point velocity measurements recorded by the ADV. The red dotted profile shows Doppler profiler observations. The black dashed line reveals the height above the vertical model datum at which the profiler sampling volume reaches the bed. The red dashed line shows the vertical position of the crest of the actual bedform recorded by the pencil beam sonar. The light blue dashed, green dashed, and gray lines represent Case 2 model simulations with sinusoidal waves, bichromatic wave groups, and real wave data, respectively. The solid blue line shows a sinusoidal wave simulation profile at $\alpha_w = 0$ (Case 1) for comparison.

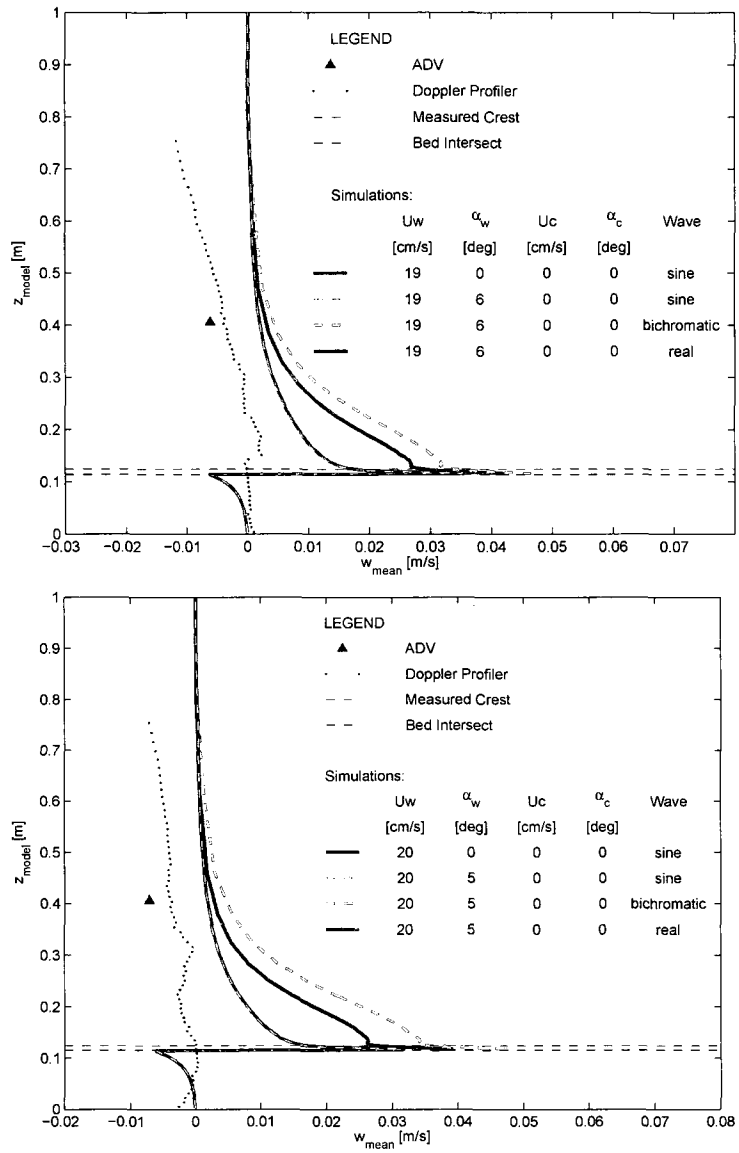

Figure C-6: Case 2: w_{mean} model-data comparison profiles for bursts 292 (top) and 294 (bottom). The triangle represents single point velocity measurements recorded by the ADV. The red dotted profile shows Doppler profiler observations. The black dashed line reveals the height above the vertical model datum at which the profiler sampling volume reaches the bed. The red dashed line shows the vertical position of the crest of the actual bedform recorded by the pencil beam sonar. The light blue dashed, green dashed, and gray lines represent Case 2 model simulations with sinusoidal waves, bichromatic wave groups, and real wave data, respectively. The solid blue line shows a sinusoidal wave simulation profile at $\alpha_w = 0$ (Case 1) for comparison.

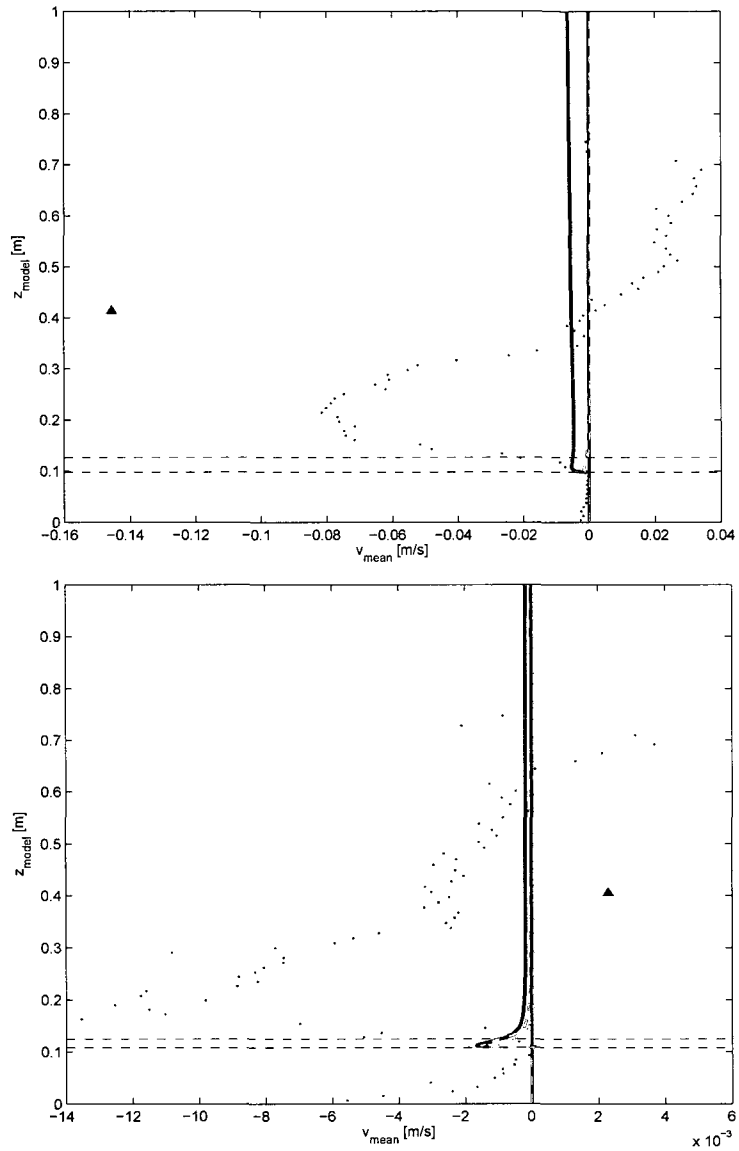

Figure C-7: Case 2: v_{mean} model-data comparison profiles for bursts 286 (top) and 289 (bottom). The triangle represents single point velocity measurements recorded by the ADV. The red dotted profile shows Doppler profiler observations. The black dashed line reveals the height above the vertical model datum at which the profiler sampling volume reaches the bed. The red dashed line shows the vertical position of the crest of the actual bedform recorded by the pencil beam sonar. The light blue dashed, green dashed, and gray lines represent Case 2 model simulations with sinusoidal waves, bichromatic wave groups, and real wave data, respectively. The solid blue line shows a sinusoidal wave simulation profile at $\alpha_w = 0$ (Case 1) for comparison.

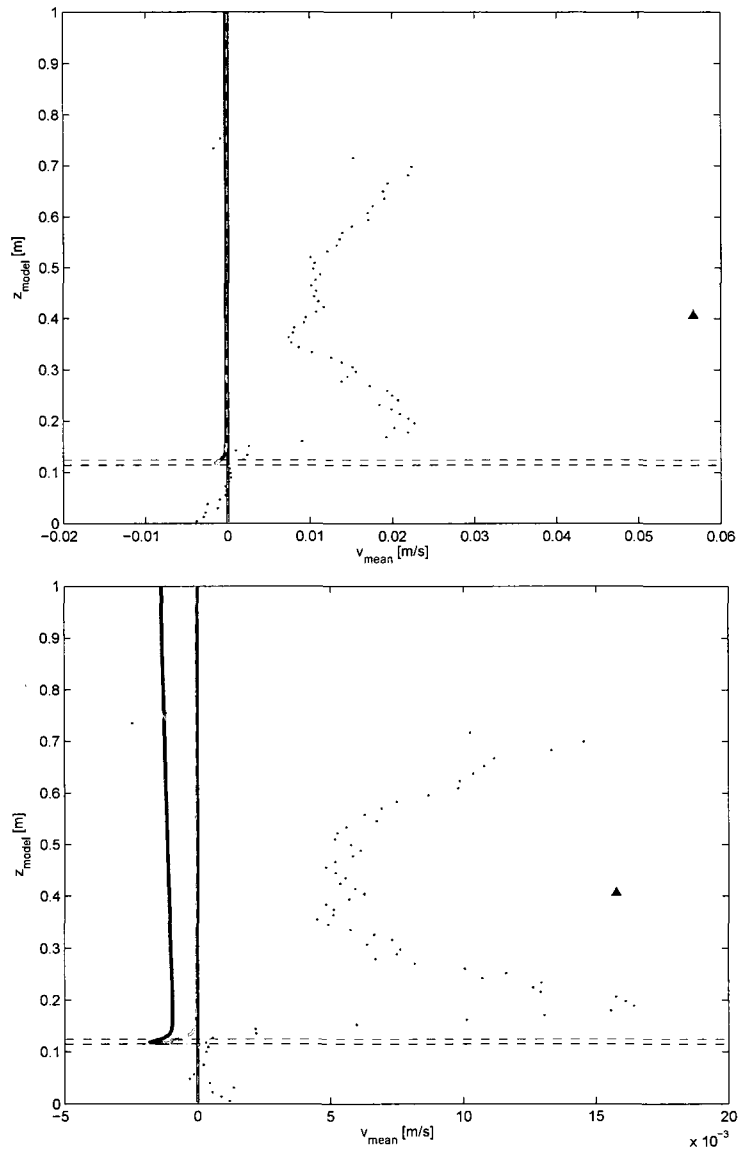

Figure C-8: Case 2: v_{mean} model-data comparison profiles for bursts 292 (top) and 294 (bottom). The triangle represents single point velocity measurements recorded by the ADV. The red dotted profile shows Doppler profiler observations. The black dashed line reveals the height above the vertical model datum at which the profiler sampling volume reaches the bed. The red dashed line shows the vertical position of the crest of the actual bedform recorded by the pencil beam sonar. The light blue dashed, green dashed, and gray lines represent Case 2 model simulations with sinusoidal waves, bichromatic wave groups, and real wave data, respectively. The solid blue line shows a sinusoidal wave simulation profile at $\alpha_w = 0$ (Case 1) for comparison.

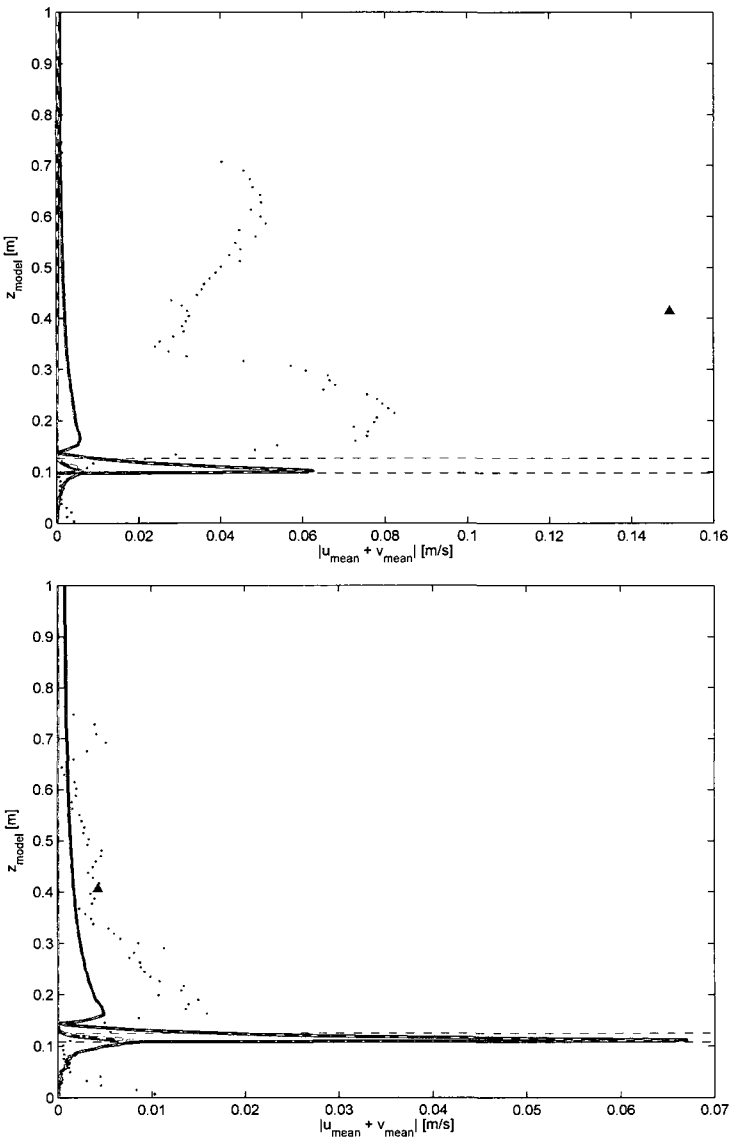

Figure C-9: Case 2: $\sqrt{u_{mean}^2 + v_{mean}^2}$ model-data comparison profiles for bursts 286 (top) and 289 (bottom). The triangle represents single point velocity measurements recorded by the ADV. The red dotted profile shows Doppler profiler observations. The black dashed line reveals the height above the vertical model datum at which the profiler sampling volume reaches the bed. The red dashed line shows the vertical position of the crest of the actual bedform recorded by the pencil beam sonar. The light blue dashed, green dashed, and gray lines represent Case 2 model simulations with sinusoidal waves, bichromatic wave groups, and real wave data, respectively. The solid blue line shows a sinusoidal wave simulation profile at $\alpha_w = 0$ (Case 1) for comparison.

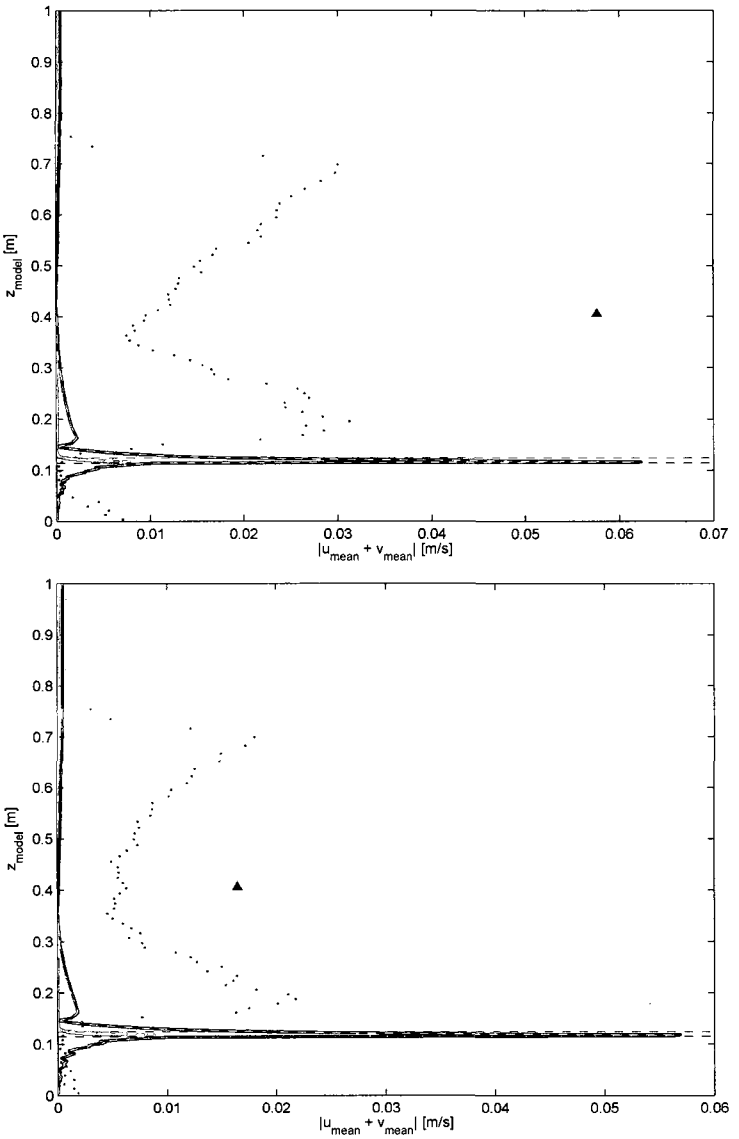

Figure C-10: Case 2: $\sqrt{u_{mean}^2 + v_{mean}^2}$ model-data comparison profiles for bursts 292 (top) and 294 (bottom). The triangle represents single point velocity measurements recorded by the ADV. The red dotted profile shows Doppler profiler observations. The black dashed line reveals the height above the vertical model datum at which the profiler sampling volume reaches the bed. The red dashed line shows the vertical position of the crest of the actual bedform recorded by the pencil beam sonar. The light blue dashed, green dashed, and gray lines represent Case 2 model simulations with sinusoidal waves, bichromatic wave groups, and real wave data, respectively. The solid blue line shows a sinusoidal wave simulation profile at $\alpha_w = 0$ (Case 1) for comparison.

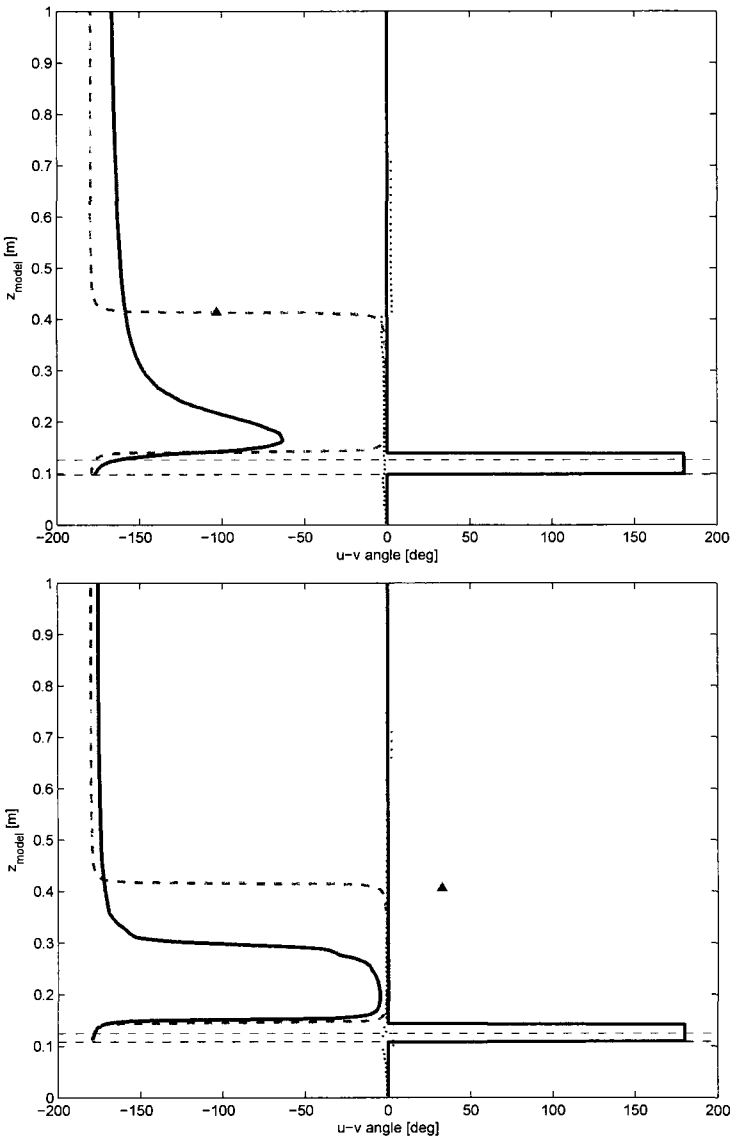

Figure C-11: Case 2: Angle of mean horizontal velocity magnitude model-data comparison profiles for bursts 286 (top), 289 (bottom). The triangle represents single point velocity measurements recorded by the ADV. The red dotted profile shows Doppler profiler observations. The black dashed line reveals the height above the vertical model datum at which the profiler sampling volume reaches the bed. The red dashed line shows the vertical position of the crest of the actual bedform recorded by the pencil beam sonar. The light blue dashed, green dashed, and gray lines represent Case 2 model simulations with sinusoidal waves, bichromatic wave groups, and real wave data, respectively. The solid blue line shows a sinusoidal wave simulation profile at $\alpha_w = 0$ (Case 1) for comparison.

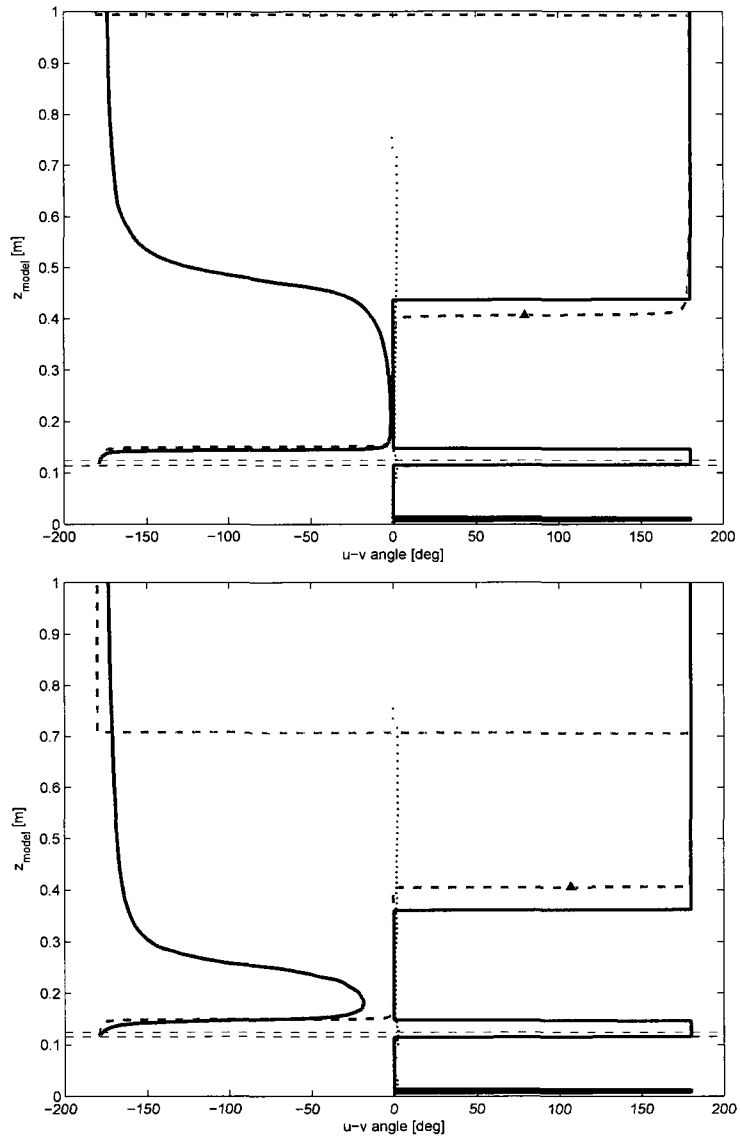

Figure C-12: Case 2: Angle of mean horizontal velocity magnitude model-data comparison profiles for bursts 292 (top), 294 (bottom). The triangle represents single point velocity measurements recorded by the ADV. The red dotted profile shows Doppler profiler observations. The black dashed line reveals the height above the vertical model datum at which the profiler sampling volume reaches the bed. The red dashed line shows the vertical position of the crest of the actual bedform recorded by the pencil beam sonar. The light blue dashed, green dashed, and gray lines represent Case 2 model simulations with sinusoidal waves, bichromatic wave groups, and real wave data, respectively. The solid blue line shows a sinusoidal wave simulation profile at $\alpha_w = 0$ (Case 1) for comparison.

C.3 Case 3 mean velocity profiles

Mean velocity profiles for u, v, and w are presented in this section for combined wave and current flow over characteristic bedforms. Sinusoidal and bichromatic wave simulations are presented.

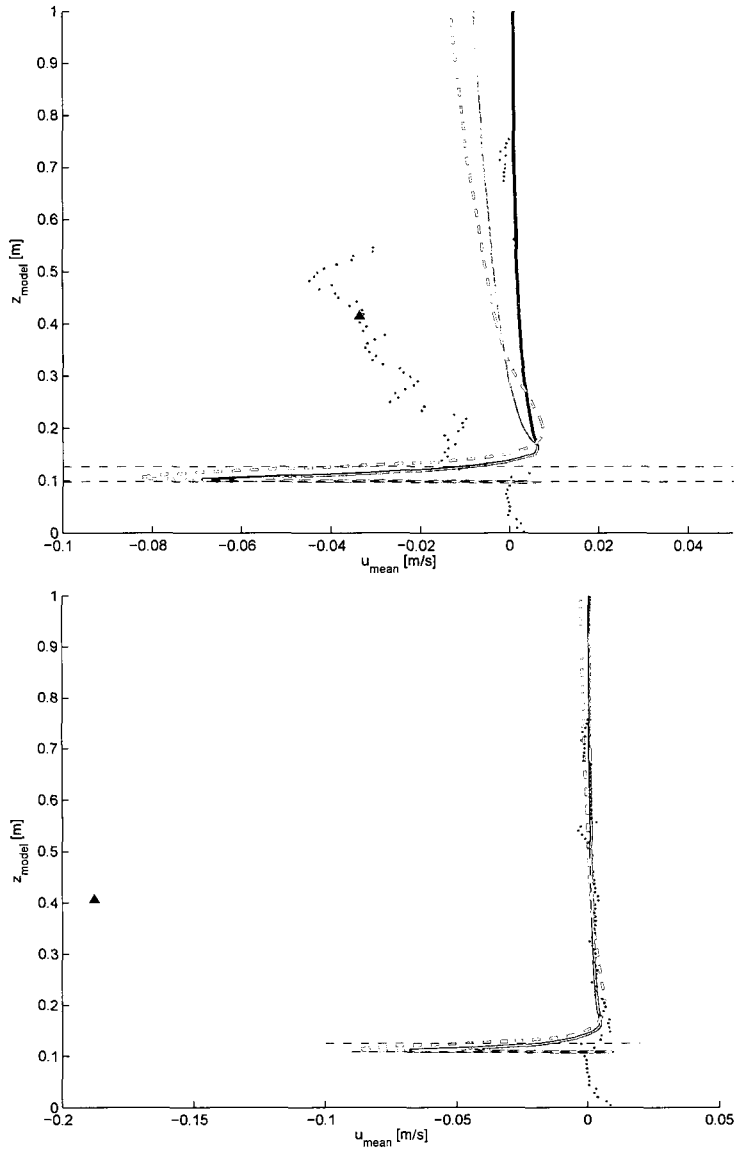

Figure C-13: Case 3: u_{mean} model-data comparison profiles for bursts 286 (top) and 289 (bottom). The triangle represents single point velocity measurements recorded by the ADV. The red dotted profile shows Doppler profiler observations. The black dashed line reveals the height above the vertical model datum at which the profiler sampling volume reaches the bed. The red dashed line shows the vertical position of the crest of the actual bedform recorded by the pencil beam sonar. The orange and green dashed lines represent Case 3 model simulations with sinusoidal waves, bichromatic wave groups, respectively. The solid blue line shows a sinusoidal wave simulation profile at $\alpha_w = 0$ (Case 1) for comparison.

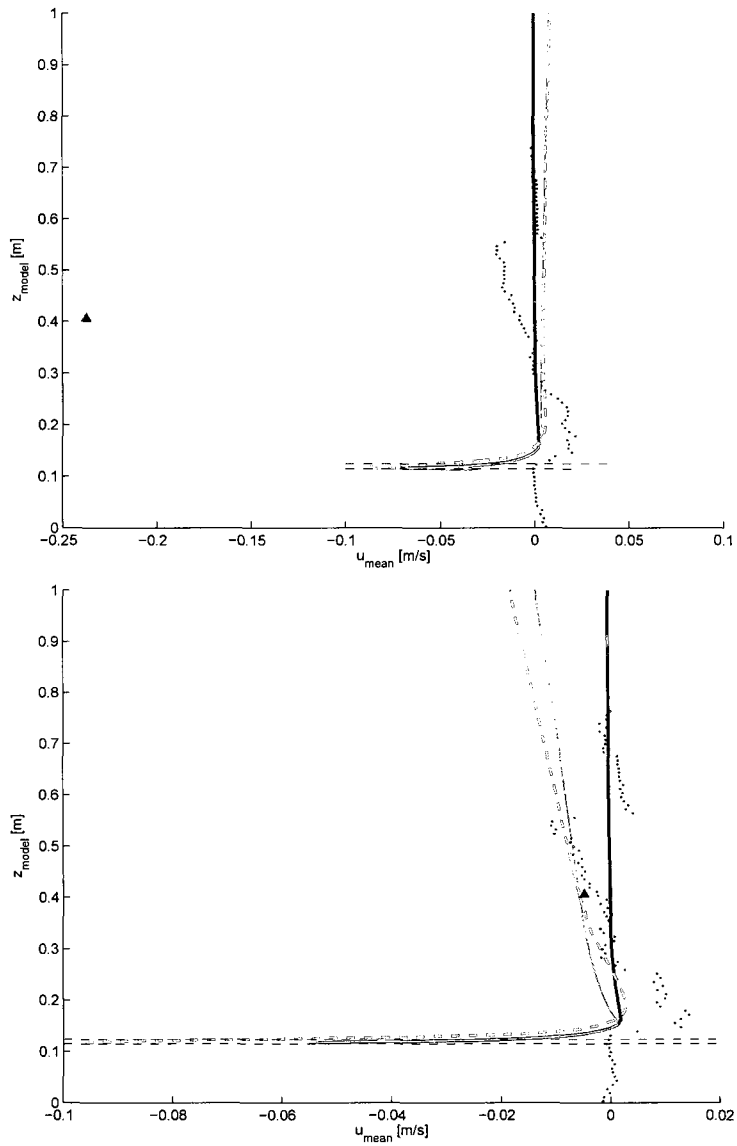

Figure C-14: Case 3: u_{mean} model-data comparison profiles for bursts 292 (top) and 294 (bottom). The triangle represents single point velocity measurements recorded by the ADV. The red dotted profile shows Doppler profiler observations. The black dashed line reveals the height above the vertical model datum at which the profiler sampling volume reaches the bed. The red dashed line shows the vertical position of the crest of the actual bedform recorded by the pencil beam sonar. The orange and green dashed lines represent Case 3 model simulations with sinusoidal waves, bichromatic wave groups, respectively. The solid blue line shows a sinusoidal wave simulation profile at $\alpha_w = 0$ (Case 1) for comparison.

LIST OF REFERENCES

Andersen, K. H. (1999), Ripples beneath surface waves and topics in shell models of turbulence, Ph.D. thesis, Technical University of Denmark, Department of Hydrodynamics and Water Resources (ISVA).

Arya, S. P. S. (1975), A drag partition theory for determining the large-scale roughness parameter and wind stress on the arctic pack ice, *J. Geophys. Res.*, *80*, 3447–3454.

Chriss, T. M., and D. R. Caldwell (1982), Evidence for the influence of form drag on bottom boundary layer flow, *J. Geophys. Res.*, *87*, 4,148–4,154.

Dalrymple, R. A. (2001), Shoring up coastal engineering, *Civil Engineering*.

Felzenberg, J. A. (2009), Detecting bedform migration from high-resolution multibeam bathymetry in portsmouth harbor, nh, usa, Master's thesis, University of New Hampshire.

Frank, D. (2008), Wave-current bottom boundary layer interactions, Master's thesis, The Ohio State University.

Fredsøe, J., K. H. Andersen, and B. M. Sumer (1999), Wave plus current over a ripple-covered bed, *Coast. Eng.*, *38*, 177–221.

Grant, W. D., and O. Madsen (1979), Combined wave and current interaction with a rough bottom, *J. Geophys. Res.*, *84*(C4), 1797–1808.

Kolmogorov, A. (1942), Equations of turbulent motion of an incompressible fluid, *Izvestia Academy of Sciences, USSR; Physics*, *6*(1 and 2), 56–58.

Kundu, P. K., and I. M. Cohen (2008), *Fluid Mechanics, Fourth Edition*, Academic Press.

Ladyzhenskaya, O. (1969), *The Mathematical Theory of Viscous Incompressible Flows, Second Edition*, Gordon and Breach.

Marieu, V., P. Bonneton, D. L. Foster, and F. Ardhuin (2008), Modeling of vortex ripple morphodynamics, *J. Geophys. Res.*, *113*, C09,007.

Natoo, P. (2003), Evaluation of near bed suspension in a wave and current dominated environment, Master's thesis, The Ohio State University.

Natoo, P. (Accepted), The suspension of sediment from flat and megarippled beds: A pairing of models and observations, *Cont. Shelf Res.*

Nelson, J. M., S. R. McLean, and S. R. Wolfe (1993), Mean flow and turbulence over two-dimensional bed forms, *Water Resour. Res.*, *29*(12), 3935–3953.

Nielsen, P. (1992), *Coastal bottom boundary layers and sediment transport*, World Scientific.

Ranasoma, K. I., and J. Sleath (1994), Combined oscillatory and steady flow over ripples, *J. Waterw. Port. C. - ASCE*, *120*(4), 331–346.

Sleath, J. F. A. (1991), Velocities and shear stresses in wave-current flows, *J. Geophys. Res.*, *96*(C8), 15,237–15,244.

Tjerry, S. (1995), Morphological calculation of dunes in alluvial rivers, Ph.D. thesis, The Danish Technical University.

Tjerry, S., and J. Fredsøe (2005), Calculation of dune morphology, *J. Geophys. Res.*, *110*(F4), doi:10.1029/2004JF000,171.

Traykovski, P. (2007), Observations of wave orbital scale ripples and a nonequilibrium time-dependent model, *J. Geophys. Res.*, *112*(C06026), doi:10.1029/2006JC003,811.

Wilcox, D. C. (1988), Reassessment of the scale-determining equation for advanced turbulence models., *AIAA J.*, *26*, 1299–1310.

Wilcox, D. C. (1998), *Turbulence Modeling for CFD*, second ed., 128-131 pp., DCW Industries.